Complementary applications of Scanning Kelvin Nanoprobe microscopy and electrochemical techniques

Aidan Rhodes

Complementary Applications of Scanning Kelvin Nanoprobe Microscopy and Electrochemical Techniques

By

Aidan Rhodes

Durham University

Department of Chemistry

A Thesis submitted for the degree of Doctor of Philosophy

May 2008

Statement of copyright

Declaration

The work described in this thesis was carried out in the Department of Chemistry at the University of Durham between October 2004 and September 2007. All the work is my own, unless stated to the contrary, and it has not been submitted previously for a degree at this or any other University.

Acknowledgements

Completing a PhD course is a long and complex undertaking, and you don't do it alone. There are many, many people that have helped and supported me along the way, and the thesis that you are reading at the moment could not exist without them.

Firstly, many, many thanks to my supervisor, Dr Ritu Kataky, whose support and belief in me and my abilities have allowed me to take and complete this degree. She has been a fantastic force every step of the way, and I would not be writing this today if it wasn't for her.

Also, of course, thanks to the ever great members of the Kataky group, past and present. Tom Jackson, Jaanus Kruusma, Radhika Bhatia, Lisa Murphy and Nilotpal Barooh have all provided help with experiments and chemicals throughout the years, and made the lab a fun and friendly place to work through the years. Special thanks to Francisco Aguiar for his help with this report. Thanks also to Anil Suri and Amit Chakraborty for making coffee time extra-special!

The support staff in the Chemistry Dept, especially the mechanical and electrical workshops, have been extremely helpful, and invaluable when I had some of my many equipment problems! Thanks also go out to the people in the Engineering and Biology Depts who helped me with my work, especially Naomi Wilis, who I hope didn't get into too much trouble when I accidently caused Biology to be evacuated! Larissa Cheran and Saman Sadhegi in Toronto have helped a lot with SKN problems and spent many patient hours on the phone with me.

Thanks also go out to Jonathan Wentworth of the Parliamentary Office of Science and Technology, who was incredibly understanding about my panicked thesis writing, and gave me the flexibility I needed at work to get this finished on time.

My parents and family have been incredibly supportive, even through some tough times of their own. They've always been there for me, and I'm incredibly grateful. I would also like to thank Dr Susan Frenk of St Aidan's for her understanding and support throughout my PhD.

And, of course, I wish to thank all of my friends here in Durham for their company over the last three years. I've had an amazing time here in this little city in the north, and one I will remember for the rest of my life. Max Parker, Emma Thompson, Nick Boalch, Grant Ingram, Adrian Brockless, Stu Greaves, the two Robs, Michelle Zang, Rachel Greenhaff, James Osbourn, Katie Carter, Will Black, and everyone else who I've had the privilege to know up here, thank you. It's been great.

To my mother, and to Ange.

The strongest people I know.

ABSTRACT

Scanning Kelvin Nanoprobe (SKN) microscopy is a new technique, based on Lord Kelvin's theory of contact electrification, which is able to measure changes in the work function of a surface with nanometre-scale precision. This technique has great potential in the analysis of surface chemistry, especially that of self-assembled monolayers and biochemical interactions. This thesis examines the potential of SKN microscopy in analytical chemical applications. SKN microscopy is used and contrasted against a range of other analytical techniques, including atomic force microscopy (AFM), confocal Raman spectroscopy and common electrochemical techniques such as cyclic voltammetry and electrochemical impedance spectroscopy.

A short background is given on SKN microscopy, as well as the other analytical techniques used. This is followed by a chapter discussing the theory behind basic electrochemistry and the electroanalytical techniques used in the thesis. Work is then presented on the hydrogen bonding environment in mixtures of dimethylsulfoxide (DMSO) in water. Confocal Raman spectroscopy showed that the hydrogen bonding environment in DMSO:water mixtures had a profound effect on the S-H (thiol) group of the amino acid cysteine, as well as on the thiol groups of the small-molecule protein analogue BMC. As molecular biologists use DMSO:water mixtures extensively in studies, this work brings up important issues concerning these experiments.

SKN microscopy was used with a range of other analytical techniques including AFM, Raman spectroscopy and cyclic voltammetry to probe the formation and characteristics of a new derivative of phthalocyanine synthesised to avoid crystalline formation and to naturally form an amorphous thin-film. Films were deposited on a variety of substrates, including gold, high-order pyrolytic graphite and glassy carbon, and were compared with a range of other phthalocyanine compounds. Simple computer modelling was also carried out on the compound. The derivative was found to form nanoporous films which allowed the passage of positively-charged molecules less then 7Å in diameter.

Self-assembling monolayers of organothiols on gold were then probed using the SKN and electrochemical impedance spectroscopy. Selections of linear, branched, cyclic, aromatic and biological organothiols were tested. The SKN was capable of directly measuring the length of a linear alkanethiol from the change in work function of the monolayer. The SKN also proved capable of measuring the degree of organisation of the monolayer – branched and cyclic alaknethiols, which are expected to form looser-packed layers, recorded more significant changes in work function. These results were confirmed by the use of electrochemical impedance spectroscopy to measure the effects of a monolayer on an electrode surface.

Abbreviations

SKN	Scanning Kelvin Nanoprobe
CPD	Contact Potential Difference
AFM	Atomic Force Microscope
EIS	Electrochemical Impedance Spectroscopy
DDT	1-dodecanethiol
HDT	1-hexadecanethiol
ODT	1-octadecanethiol
DMSO	Dimethylsulfoxide
BMC	(±)trans-1,2-bis(2-mercapto-acetamido)cyclohexane
HOPG	Highly-ordered pyrolytic graphite
PDI	Protein Disulphide Isomerase
Ero1p	Endoplasmic Reticulum Oxidoreductin 1 protein
I	Electrical current, measured in amperes
V	Electrical potential, measured in volts
RMS	Root-mean-square
MALDI-TOF	Matrix-assisted laser desorption/ionization – time of flight

Table of Contents

Chapter 1: Introduction and Literature Review **5**

1.1 Scanning Kelvin Nanoprobe Microscopy 5

1.1.1. Work function *7*

1.1.2. Kelvin probe theory *9*

1.1.3. Development *14*

1.1.4. Modern Scanning Kelvin Nanoprobe microscopy *16*

1.1.5. Sample nature and measurement considerations *18*

1.2 Atomic Force Microscopy 24

1.2.1 Contact Mode *25*

1.2.2. Non-contact Mode *25*

1.2.3. Tapping Mode *25*

1.3 Raman Spectroscopy 27

1.3.1. Confocal Raman Microscopy *29*

1.3.2. Surface-Enhanced Raman Spectroscopy *30*

Chapter 2: Electrochemical Techniques **36**

2.1 Introduction 36

2.1.1 General Overview *36*

2.1.2 The Electrical Double Layer *38*

2.1.3 Half-cell potentials and the Nernst equation *40*

2.1.4 Kinetics of Electrode Reactions *42*

2.2 Cyclic Voltammetry 48

2.2.1 Introduction *48*

2.2.2 Reversible cyclic voltammetry scans *50*

2.2.3 Quasi-reversible and irreversible cyclic voltammetry scans *53*

2.2.3.2: The EC mechanism *54*

2.2.4 Electrochemical simulations *57*

2.3 Electrochemical Impedance Spectroscopy 59

2.3.1 Introduction *59*

2.3.2 Equivalent Circuits *62*

Chapter 3: The effects of hydrogen bonding environments on thiol groups. 69

3.1. Introduction 69

3.1.1. Thiol groups in biology *69*

3.1.2. Enzymatic protein folding *72*

3.1.3. BMC: A small-molecule analogue of PDI *73*

3.1.4. Dimethyl Sulfoxide *74*

3.1.5. Objectives *76*

3.2. Experimental Details 77

3.2.1. Solution preparation *77*

3.2.2. Raman spectroscopy measurements *77*

3.3. Results and Discussion 78

3.3.1 Raman spectra of cysteine *78*

3.3.2 Raman Spectra of BMC *84*

3.4 Conclusions 88

Chapter 4: SKN and Electrochemical Investigation of Nanostructured films of Phthalocyanine Derivatives 91

4.1. Introduction 91

4.1.1 Phthalocyanine *91*

4.1.2 Phthalocyanine thin-films *92*

4.1.3 Axially-substituted phthalocyanine derivatives *93*

4.1.4 Objectives *95*

4.1.5 Analytical Methods *97*

4.2 Experimental Details 99

4.2.1 Thin-film preparation *99*

4.2.2 Scanning Kelvin Nanoprobe Microscopy *99*

4.2.3 Atomic Force Microscopy *100*

4.2.4 Confocal Raman Microscopy *100*

4.2.5 Cyclic Voltammetry *101*

4.3 Results and Discussion 102

4.3.1 Molecular Modelling *102*

4.3.2 Scanning Kelvin Nanoprobe Microscopy *106*

4.3.3 Atomic Force Microscopy *110*

4.4.4 Confocal Raman Microscopy *114*

4.4.5 Cyclic Voltammetry *116*

4.5 Conclusions 124

Chapter 5: Investigation of Self-Assembled Monolayers of Thiol-Containing Compounds on Gold **128**

5.1 Introduction 128

5.1.1 Self-assembling monolayers *128*

5.1.2 History ..... ***Error! Bookmark not defined.***

5.1.3. Organothiol monolayers *129*

5.1.4 Preparation *131*

5.1.5 Objectives *134*

5.1.6 Analytical Methods *136*

5.1.8 Preparation concerns *137*

5.2 Experimental Details 139

5.2.1 Organothiols under investigation *139*

5.2.2 Substrate preparation *142*

5.2.3 Self-assembling monolayer preparation *142*

5.2.4. Scanning Kelvin Nanoprobe Microscopy *148*

5.2.5 Electrochemical Impedance Spectroscopy *149*

5.3 Results and Discussion 150

5.3.1 Scanning Kelvin Probe Microscopy *150*

5.3.2. Electrochemical Impedance Spectroscopy *176*

Chapter 1: Introduction and Literature Review

This chapter provides an introduction to the concept of the work function, and to the technique of Scanning Kelvin Nanoprobe Microscopy (SKN), looking at the theory, development and current usage of the technique. In addition, the techniques of Atomic Force Microscopy (AFM,) and confocal Raman spectroscopy are discussed.

1.1 Scanning Kelvin Nanoprobe Microscopy

In the last couple of decades much work has been done to advance the field of scanning probe microscopy techniques. Instead of working with optical wavelengths or electron beams to image a surface, both of which have resolution limits imposed by the wavelengths of the imaging medium, these techniques use the movement of a small, often micro- or nano- metre sized, tip over a surface to measure its properties. Popular techniques in this field include the Atomic Force Microscope (AFM), (See section 1.2), which images the topographical properties of a surface by the contact of a moving tip, the Scanning Tunnelling Microscope[1](STM), which images and manipulates conductive surfaces by utilising the quantum tunnelling effect, and the Scanning Electrochemical Microscope[2](SECM), a device which utilises microelectrodes in a typical three-electrode cell in order to image the conductive properties of a substrate in solution.

A second advantage of using a probe instead of an optical beam is that a microscope can be used to measure and influence properties other then the topographical layout of a substrate. The AFM can for instance, when placed in 'tapping mode', a mode which oscillates the tip at very high frequencies and moves it into contact with the surface, create images of the viscoelastic properties of a substrate simultaneous with topographical images, which enable mapping of variations of properties such as the hardness and degree of

crystallisation of a sample. The SECM, utilising the microelectrode's ability to act as an electron source or sink, can modify surfaces by electrochemically generating reagents at the tip, leading to use as a versatile micro-fabrication device.

The rapidly expanding field of probe microscopy has led to massive advances in tip positioning and piezoelectric technology, as well as advances in precise and sensitive measurement of small variations electrical currents. Information technology has also greatly improved, allowing real-time reading and modification of scans as well as a great range of image enhancement techniques. This has all led to a fertile and significant environment for the research of new methods of scanning probe microscopy. This introductory chapter examines the theory, development and application of relative work-function measuring scanning probe microscopy, referred to as Scanning Kelvin Nanoprobe microscopy or SKN for short.

SKN microscopy is a refined development of the Kelvin probe, a device used in corrosion studies and studies of semi-conducting interfaces, as well as in the investigation of layer and surface processes[3]. The Kelvin probe takes its name from the famous Scottish scientist William Thompson, later to be given the title of Lord Kelvin. In a British Institution lecture in 1898[4] he demonstrated the 'phenomenon of the contact electrification of metals'. This was demonstrated using two large plates, one made of copper and the other zinc. When brought into contact via a wire, the two plates developed surface charges and thus a potential difference between them when brought into close proximity to one another. The cause of this phenomenon was unknown at the time. Today, a century later, this effect becomes the core of relative work function measurement; and thus of the Scanning Kelvin Nanoprobe.

Until now, the Kelvin probe technique for measuring work functions has been used mainly to investigate surface chemistry, corrosion, stress and semi-conducting surfaces. The investigation of biological surfaces and materials using Kelvin techniques is a new area under investigation, using high-resolution

scanning probes. The study of microarrays, both nucleic acid and protein-based, is an obvious application for a Kelvin probe due to its ability to sense changes in the properties of materials. With microarray spot density continually increasing, the errors encountered with standard confocal fluorescent microscopy become a greater issue. The low brightness of fluorescent dyes combined with background interference, as well as the interference of the dyes with the arrangement of the nucleic acids, cause significant issues with detecting hybridisation. Therefore, higher resolution, fluorescent label-free methods are required to extract the maximum amount of data from each array.

Preliminary work on detecting changes in nucleic acid microarrays due to hybridisation was carried out by Michael Thompson's group in 2000[5]. They discovered that differences between conjugated and unconjugated microarray spots could be observed directly with the Kelvin probe, without the need to attach fluorescent labels as done conventionally. Because of the increased resolution of the scanning Kelvin microprobe compared to a confocal fluorescent microscope, the Kelvin probe can be used to investigate far more densely packed microarrays with smaller spot sizes then fluorescence will allow. Due to the limitations of robotic-based microarray printing today, this resolution is not necessary, but may well become important with further printing advances in the future.

1.1.1. Work function

The SKN microscope images two properties of a surface; the topographical profile and the contact potential difference (CPD) profile. To understand the CPD image, which is a measurement of the work function of the substrate relative to the probe tip, an explanation of the work function property is required.

The work function of a substance is a fundamental property of that substance. It is closely related to its Fermi energy. The Fermi energy is a concept in quantum

mechanics that refers to the highest occupied quantum state in the electronic band, the aggregate of the atomic orbital energies present in a solid[6]. This level, otherwise defined as the mean electron energy of the solid, is located in different areas of the band for different materials. For a metal, the filled and empty bands overlap, producing a substance that is conductive regardless of temperature. The overlap between the filled and empty bands reduces as the conductivity of the substance reduces, and semiconducting materials have a bandgap between the filled (valence) and empty (conductive) bands.

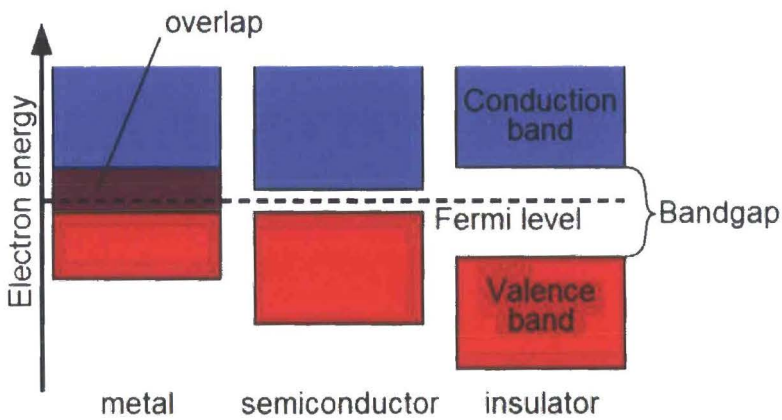

Figure 1.1.1.1: Comparison of the electronic band structures of metals, semiconductors and insulators.[25]

The standard definition given of the work function, Φ, of a conducting substance is given as the minimum energy required (usually measured in electron-volts), in order to remove an electron from the Fermi level of the conducting substance through the surface to a point where the substrate can exert no influence on the electron. This electric potential is known as the Volta Potential or the vacuum potential and is represented by Ψ. Thus the work function can be expressed as the following equation:

$$\phi = -e\Psi - E_F$$

Where e represents the unit charge and E_F represents the Fermi energy.

As the work function is a measurement of the energy required to remove an electron from a material, through the surface, the work function of a material is heavily influenced by the surface properties of that material. A wide variety of surface properties can therefore influence the work function, including the conductance, topological layout and optical properties of the material. Therefore, work function measurements are highly useful in the investigations of adsorbed layers, layer imperfections, surface charging and other surface-based properties.

There are two general methods of measuring a work function; absolute and relative. An absolute method of measurement involves inducing electron emissions from the sample surface via photo or thermionic methods. Photoelectron spectroscopy or XPS is an example of this method. A relative method such as the Kelvin probe measures the contact potential difference between the sample and a reference probe.

1.1.2. Kelvin probe theory

As explained above, the work function Φ is the energy required to move an electron from the Fermi (E_F) level of a conductor through the surface to a point infinitely distant. Consider two conducting metals with complete electrical separation and with Fermi levels E_1 and E_2.

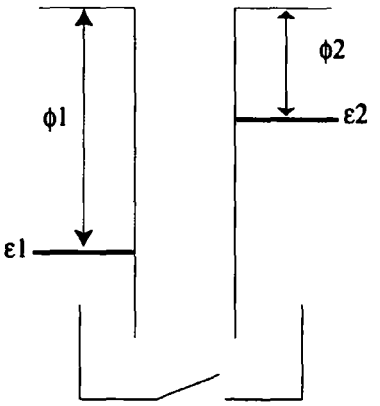

These metals have work functions defined as Φ_1 and Φ_2. When the two are brought into electrical contact, electrons from the metal with the higher Fermi energy flow to the metal with the lower Fermi energy. This continues until the Fermi energy of the two metals equalises. This flow of electronic charge creates a potential between the faces of the two metals equal to the difference between their work functions, defined as;

$$V_C = \Phi_1 - \Phi_2$$

This is known as the Contact Potential Difference, or CPD, and can be represented graphically by the following;

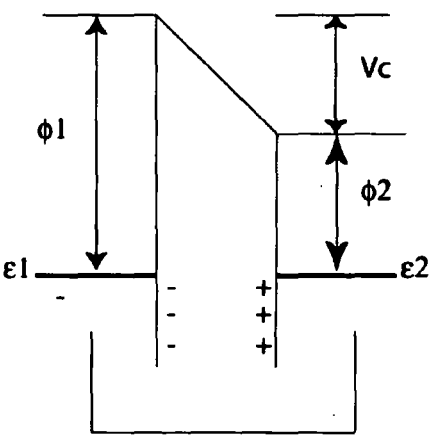

As can be seen above, the connection of the two metals and the resulting equilibrium of their Fermi levels cause a capacitive charge to be built up on the opposing faces of the metals. This charge can be nullified and V_C measured by the application of a backing voltage, V_B, equal and opposite to V_C, as shown below;

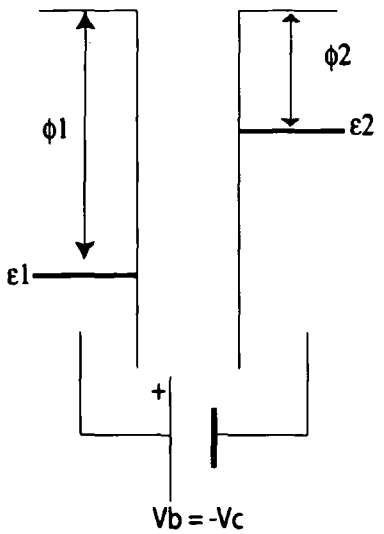

This solution, while allowing the contact potential difference to be accurately measured, possesses the disadvantage of not being able to measure continuously, due to the time needed for the charge between the plates to dissipate. Therefore, a method of measuring the contact potential continuously was required. Such a method was discovered by Zisman in 1932[7]. This involves using a vibrating probe, with a capacitance calculated by using the formula;

$$C = \frac{Q}{V} = \frac{\varepsilon A}{d} \qquad (1)$$

Where: C is the capacitance in farads

Q is the charge in coulombs

V is the potential in volts,

ε_0 is the permittivity of the dielectric,

A is the surface area in m^2,

d is the distance between the capacitance plates in m.

When one plate of the capacitor is vibrating, the distance d is constantly changing, and therefore the capacitance changes as well – getting lower when the probe is further away and higher when the probe is closer. As the charge on the plates remains constant, due to the work functions being constant values, the voltage must therefore change. This creates a sinusoidal waveform, allowing the distance between plates to be expressed as;

$$d(t) = d_0 + d_1 \cos \omega t \tag{2}$$

Where d_0 is the mean distance tip-sample separation, ω is the angular frequency of vibration and d_1 is the amplitude of vibration.

The application of a variable dc voltage source to provide the backing potential can therefore lead to the equation;

$$i_t = \frac{dQ}{dt} = (V + V_0) \frac{\varepsilon \omega d_1 A \omega t}{(d_0 + d_1 \cos \omega t)^2} \tag{3}$$

Where : i_t is the Kelvin current,

Q is the charge,

d the distance,

V is the voltage difference between the probe and the sample,

V_0 is the backing voltage,

C_0 is the capacitance of the probe,

ε the permittivity of the dielectric medium,

ω is the angular frequency of vibration,

A is the area of the capacitive plates,

Φ is the phase angle,

t is the time.

This can be used to work out the contact potential between vibrating probe and sample tip by varying the backing potential V_0. At the point when $i_t = 0$, the backing potential will be equal and opposite to the contact potential.

This can therefore be used to determine contact potentials and therefore work functions continuously and without the need to dissipate capacitive charge, and is therefore greatly useful for microscopy and the measurement of continuous change with time.

Kelvin probe measurements can be carried out as long as there is a dielectric material gap separating the tip and the sample. This gap can be either air or a vacuum. When measuring in liquids, the tip must be coated with a dielectric material to ensure accurate measurement.

1.1.3. Development

After the invention of the vibrating probe tip by Zisman in 1932, work progressed on developing the method further. However, there were few major advances in accuracy and precision of Kelvin probes for over forty years. This is due to the convergence of several factors. Firstly, the research push at that time was toward understanding the bulk properties of solids, with little thought given to surface properties other then considering them a minor hindrance. Also, the engineering ability to move a tip with micrometre-precision near a surface did not exist, and neither did the computational ability to analyse and display data collected by the probe. The interest in making highly-precise spatial contact-potential measurements resurfaced in the 1970s with a desire to monitor changes to areas of conducting surfaces over time[8]. The a.c method proposed by Zisman was refined further[9], but it was not until 1976 that the first piezo-electric Kelvin probe was designed[10]. This allowed far precise spatial movement over a surface, allowing the development of far more spatially accurate Kelvin probes.

The spatial resolution of these microscopes was usually about 50μm, using a tip, usually a vibrating wire, of about 6μm across. Precision in recording CPD values was about 20mv[11]. This dropped quickly with improvements in amplifier and frequency analyser technology, to about 1mv by 1982[12].

As CPD and spatial resolution increased, the issue of stray capacitance, signals picked up from the other metallic components of the Kelvin probe, became more of an issue. When the probe size became less then 1mm, this stray capacitance becomes large enough to mask weak changes in CPD. Several solutions were proposed to this, of which the simplest and most enduring is a insulating guard shield, surrounding and extending behind the probe but being electrically isolated from it [8]. This size and spacing needs to be tailored to each probe individually, due to differing components and whether the probe is to be used in vacuum or not, but generally a probe-shield spacing of over 200μm proves largely ineffective[13].

By 1991 the first use of a Kelvin probe to distinguish the CPD difference between different materials was demonstrated[14]. This scanning probe, developed at IBM in New York, had a lateral resolution of 50nm and a CPD sensitivity of ~50μv, using a gold-coated silicon tip with a radius of 50nm.

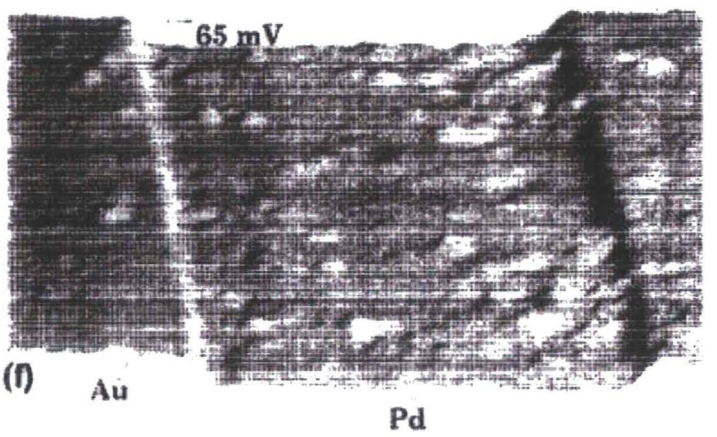

Figure 1.1.3.1: An 8μm by 6μm CPD scan of palladium deposited on gold, taken by the 1991 IBE Kelvin probe force microscope.

This scanning probe could operate successfully in both air and ultra-high vacuum (UHV). If in UHV, a tenfold sensitivity increase was observed, due to an increase in the quality of the capacitive field generated.

The invention of Atomic Force Microscopy (AFM) in the 1980s had useful implications for the development of Kelvin probe microscopy. The two techniques both use a small sharp tip scanning over a surface with sub-micron precision, meaning that technological advances in one could easily be applied to the other. The term Kelvin Force Microscopy became common as a method to describe the non-contact mode of an AFM[15]. This is an incorrect usage of the term, however, as a non-contact AFM measures electrostatic force from Van

der Waals fields, not work function. In 1999, the first scanning Kelvin nanoprobe was developed by a group in Toronto[12]. This probe was the first to use a tip of less than 0.5μm to measure Kelvin currents.

1.1.4. Modern Scanning Kelvin Nanoprobe microscopy

The scanning Kelvin nanoprobe in use at Durham was developed by Professor Michael Thompson and his research group at the University of Toronto[16]. This probe utilises piezoelectrically vibrated tungsten microelectrode tips of a ~50nm radius, protected by a guard shield surrounding and electrically isolating the tip. Tungsten is used as the tip material due to its extremely stable work function, which is highly resistant to changes in temperature and environmental conditions, and remains stable over a large period of time. Stray capacitance is minimised by this guard shield, as well as electrical shielding on all leads and surfaces. The tungsten tip and an accompanying metallic piezoelectric table form a system of two metallic plates, which function as a capacitor. A sample placed on the piezoelectric table, and therefore between the two plates, has measurable properties based on the change of dielectric permittivity between the material and the free space between the plates (usually air). As shown above in Section 1.1.2, the CPD of the material compared to the tip is therefore measured by the local capacitor thus formed between the vibrating tip and the sample.

In the SKN in use at Durham, the tip vibrates at a frequency of between 1.7 and 2kHz, depending on the exact properties of the tip. As there are slight variations in size and length between tips, caused by natural variances in the manufacturing process, this frequency is set manually when a new tip is installed and is calibrated precisely to minimize background noise at the tip. The tip is positioned close to the substrate surface firstly by manual approach, and then by automated computer control, which measures the Kelvin current obtained and positions the tip in an area bounded by preset CPD values. Once an operational distance is reached, the tip is scanned over the substrate surface

in a preset pattern in the x and y axes. This is also fully automated, allowing for extremely small (up to 100nm) steps to be taken.

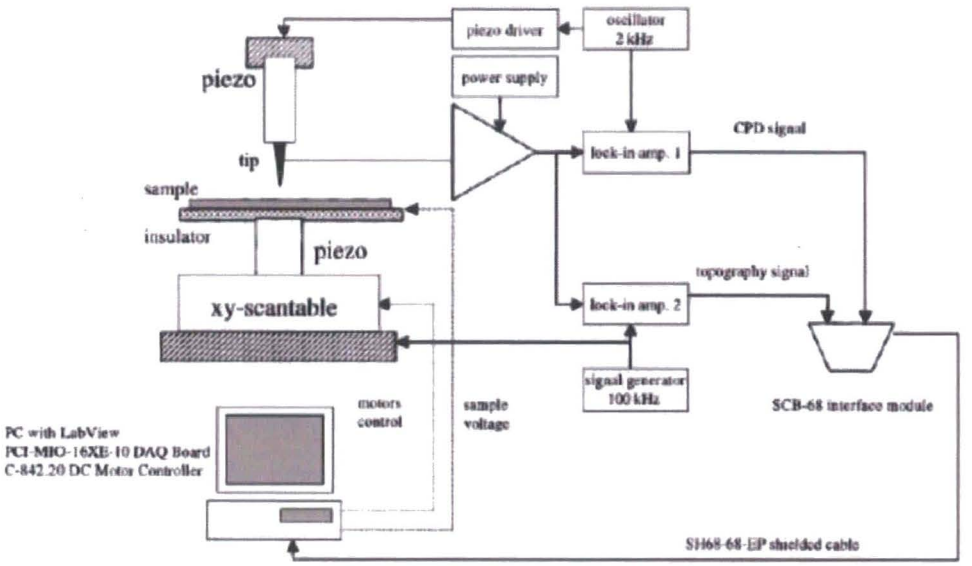

Figure 1.1.4.1: A systems level diagram of the scanning Kelvin nanoprobe.[3]

The collected Kelvin current signal arising from the vibrating capacitive field is extremely small, in the picoamp region, due to the small size of the tip. This signal is thusly boosted through an ultra-low noise amplifier and converted to a voltage, which is then inputted into a pair of lock-in amplifiers. One of these amplifiers detects the CPD signal, the other the topographical signal. The tip is kept at a constant height by a z-axis piezopositioner, which maintains the distance via a feedback loop by ensuring the tip is kept within the CPD bounds previously specified. This mechanism also allows the simultaneous collection of topographical images.

The two signals are fed from the lock-in amplifiers via a data acquisition card (DAQ) into a personal computer. The computer contains the user interface and

control mechanism for the SKN, which is implemented in National Instrument's Labview software. Labview is a powerful tool for controlling scientific instruments, as it allows the construction of virtual circuitry and thus instruments within the PC. This allows precise tuning and testing of the SKN instrumentation without the need for complex and expensive physical hardware and is therefore an extremely important component of the developmental SKN.

The Labview SKN control programs automate measurement and data collection, and return a pair of ASCII text files from a completed scan, which contain values at each point of the scan for the CPD and topography values respectively. These can be measured using any capable mathematical analysis program. In this thesis, OrginLab 7.5 has been used to analyse the measured SKN data.

1.1.5. Sample nature and measurement considerations

The Fermi energy of different classes of materials, as can be seen in Figure 1.1.1.1 above, varies greatly. In metallic substances, the Fermi level lies at the overlap of occupied levels, and transfer of electrons between the occupied levels is therefore simple and energy-efficient. Semiconductors are characterised by a very small band gap, and transfer of electrons from the valence and conduction bands requires only a small input of energy. The relative work function of these materials can therefore be characterised easily via a Kelvin probe measurement by direct analysis of the CPD values. This led to the adoption of Kelvin probes in surface science, performing measurements to characterise surface roughness, catalysis and layer imperfections over a large range of metallic and semiconducting samples.

Dielectric materials such as ceramic, mica and glass are poor conductors of electricity but efficient at supporting electrostatic fields such as those found in capacitors. A dielectric medium possesses a property known as permittivity, or ε, relating to the charge distribution within a material to be polarised in response to an electric field. These substances were previously thought

impossible to measure directly using a Kelvin probe. This is due to the typical band structure of dielectric materials which place the Fermi energy level in a large band gap, which makes the transfer of electrons between the occupied valance and unoccupied conduction bands extremely difficult. As electrons cannot cross this large band gap, the contact potential difference cannot therefore be measured by regular means.

Biological samples such as DNA and proteins fall into the category of dielectric materials. The properties of such, including DNA hybridisation and protein folding configurations, are extremely important to biologists and biochemists. As these properties can be directly measured via the investigation of the work function of the sample, due to the change in dipole moments caused by the change in configuration, a Kelvin probe, should it prove capable of measuring the work function of dielectrics, would be an extremely powerful tool in microbiological analysis.

The Thompson group showed[16] that if a monolayer of a dielectric material deposited on a conductor is considered, the dipole moment of the dielectric material can be expressed as;

$$m = Q_d l \tag{3}$$

Where Q_d is the dipole charge and l is the separation distance[17]. The voltage drop over the layer can therefore be expressed as;

$$U = \frac{Q_d}{\epsilon_{sample}} l \tag{4}$$

U is therefore the voltage drop over a monolayer of the dielectric material, and the value which should theoretically modify SKN CPD scans where a monolayer of dielectric material has been deposited over a conducting substrate.

In 2000, the Thompson group succeeded in producing SKN CPD images illustrating a clear differentiation between the work function of DNA spots and the glass slide upon which they had been printed. Subsequent images showing differentiations in protein microarrays and dielectric materials such as mica were produced. Why this is possible was not understood, as conventional theory on dielectric materials claims that this should be impossible.

Further work in this area[17] showed that this is due to the change in dipole moment between hybridised and unhybridised DNA molecules. A unhybridised single DNA strand possesses a large lateral dipole moment due to the net negative charge of the molecule and the fact that it is surrounded by negative counter-ions. During hybridisation, another complentary DNA strand will cancel out this dipole moment, so that the net dipole moment for a hybridised DNA strand is zero. A similar change is noticed on protein molecules, as the dipole moment of a protein depends on the individual moments of its constituent parts, which will change with any molecular interactions. Thus, the Kelvin probe can also be used to investigate biomolecular interactions on protein microarrays.

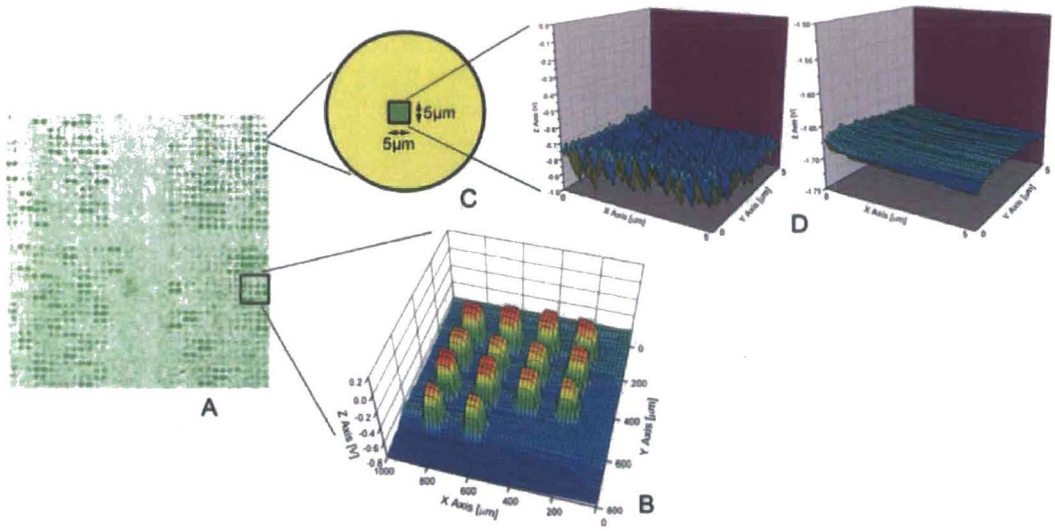

Figure 1.1.5.1: DNA microarray imaged by (a) fluorescence microscopy, (b) CPD image from Kelvin nanoprobe with 20µm step, (c), (d), CPD and topographical images from Kelvin nanoprobe with 100nm step.[5]

As changes in dipole moments can be seen to be investigated with the SKN, it stands to reason that dielectric compounds are therefore measurable. The current hypothesis developed by Thompson and Cheran[18] observes that the measurement of dielectric compounds is possible with the SKN, provided that the compounds are between the two conducting plates of a capacitive system. A dielectric sample will have a significantly different permittivity ε then that of free air, the dielectric usually between the two plates. This alters the CPD values recorded considerably over areas where a dielectric sample is present. In reality, the system can be considered as two capacitors in series, one between the probe and the dielectric sample and one between the dielectric sample and the piezoelectric table. These two capacitors have different permittivity values – the first free air and the second the dielectric sample itself.

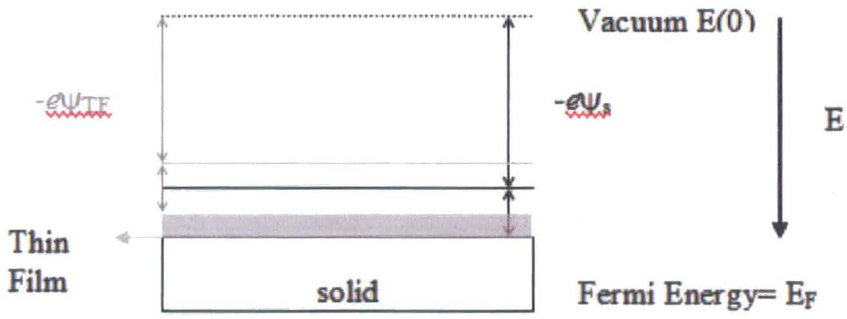

Figure 1.1.5.2: Diagram showing the difference in Volta energies (-eΨ) of a bare gold substrate and a substrate with a dielectric thin film.

As the diagram shows, the Volta potential of a substance changes when a monolayer of a dielectric sample is deposited. This therefore affects the corresponding work function of the sample, via the relationship;

$$\Delta\phi_{TFS} = \phi_{TF} - \phi_S = -e(\psi_{TF} - \psi_S) \tag{4}$$

This leads to one of the major operational issues with the SKN. Due to changes in background noise, temperature, humidity and other environmental conditions, an absolute CPD value of a substrate can almost never be accurately obtained. Two scans of the same area of plain gold, for example, will not return the same average CPD value, nor one within an acceptable margin of error. However, two scans of a patterned monolayer will return the same change in CPD between the bare and monolayered regions of gold. The SKN therefore is extremely useful not for determining the absolute work function values of a surface, but the changes that adsorbed materials or other chemical treatments create.

This however leads to the problem that any dielectric material to be examined by the SKN cannot be deposited on the surface of the conducting substrate by standard immersion monolayering techniques, but by methods designed to cover a portion of the substrates surface, leaving sections bare in order to view the substrate/monolayer contrast. Methods used to accomplish this are diverse, and the specific methods used in this thesis will be covered in the chapters detailing the work in which they apply.

Tip degradation is also an issue when using the SKN. The tips are manufactured with a diameter of ~100 nm, but use and the occasional tip crash degrade the tip to the point where the diameter can be many micrometres in diameter. The difficulty of changing and calibrating the tip in the current SKN setup means that tips are usually changed out only when absolutely necessary, which limits the operational resolution to the micrometre range.

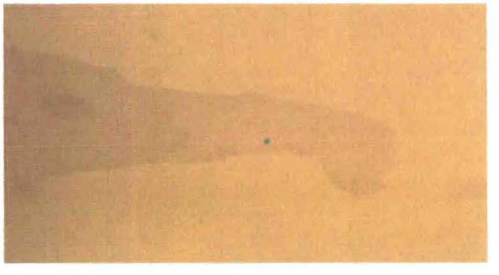

Figure 1.1.5.3. Optical microscopy image of new SKN tip.

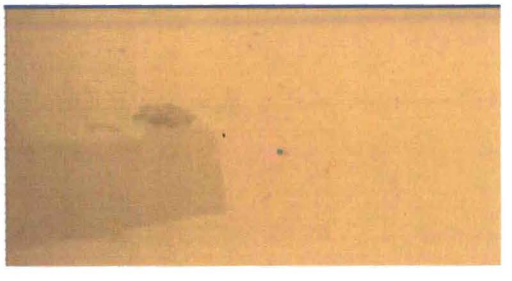

Figure 1.1.5.4. Optical microscopy image of SKN tip after ~6 months of use.

1.2 Atomic Force Microscopy

Atomic Force Microscopy was developed in 1986 by Binnig, Quate and Gerber[19]. Like the Kelvin probe and other scanning-probe microscopes, it uses a fine tip which is scanned across the surface of a sample to form an image. In a standard AFM, the probe tip is mounted on the end of a cantilever, which deflects according to the force on the tip. This force is measured, usually by focusing a laser on the cantilever and measuring the change in laser signal by a photodiode. This allows very small differences in topography to be imaged – the latest AFMs have a resolution measured in picometres[20]. The AFM is primarily a topography measuring device but is fairly easily modifiable to other uses, for example being used as a Kelvin probe[21].

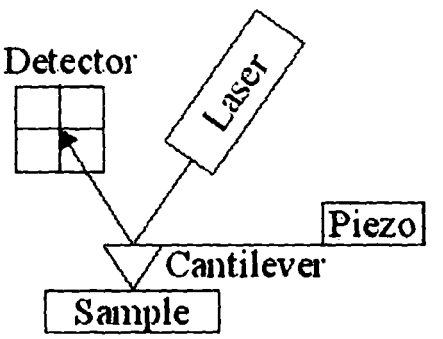

Figure 1.2.1: Simple diagram of AFM operation.

There are three commonly used modes when imaging with AFM; contact, tapping and non-contact[22].

1.2.1 Contact Mode

When the AFM is in contact mode, the tip is pushed against the surface with a piezoelectric motor, and dragged along the sample. The deflection of the cantilever is measured with the laser and any changes in deflection due to topography are recorded. This is the simplest of the AFM modes – its major drawback stemming from the large lateral forces sometimes applied to the tip. Under ambient conditions, a problem also arises from a thin (20-30 monolayers) layer of adsorbed water vapour and nitrogen on the sample surface, which can be negated by performing the measurements in liquid. Issues with many surfaces holding a charge also cause the AFM tip to press harder against these samples, causing frictional forces and possible damage to the sample and tip.

1.2.2. Non-contact Mode

When using the non-contact mode, the tip hovers generally 50-150 nanometres above the surface to be imaged. The tip cantilever is oscillated so that Van der Waals forces can be detected using an ac method similar to the Kelvin probe. Van der Waals forces are substantially weaker than actual surface contact, and the probe tip can often get caught or image the vapour layer above the sample so non-contact mode's applications are usually limited only to very fragile or difficult samples. This method is unusable in liquids, due to the interference from surrounding liquid molecules.

1.2.3. Tapping Mode

Tapping mode provides a way to obtain the high resolution found with contact mode AFM while avoiding the frictional problems and other difficulties found with this mode. In tapping mode, the cantilever is oscillated near its resonant frequency by a piezoelectric crystal, (typically 50-70000 Hz) and is then moved toward the surface until it comes into light contact with it. The tip is then

moved along the surface, coming into contact with it at the downwards portions of the stroke. As the cantilever comes into contact with the surface, the amplitude of oscillation decreases, which is detected by a laser-photodiode system. The high frequency of oscillation also reduces adhesion between the tip and sample, which helps to prevent damage to both. Tapping mode can be used in liquids, but with a reduced oscillation frequency due to liquid drag. Often the entire liquid cell is oscillated to reduce this problem.

AFM technology has also been applied to solve problems in data storage and retrieval. Researchers at IBM are developing a system codenamed 'Millipede[23]' which uses an array of more than a thousand heated AFM tips to punch small holes in a substrate and read this information back in massive parallel. Although not ready for commercial use, this system shows a far higher data density and read/write speed then ordinary flash memory.

1.3 Raman Spectroscopy

Raman spectroscopy is a technique which utilises the inelastic scattering of light, an effect known as the Raman Effect, to study the chemical composition of materials.

When a beam of monochromatic radiation hits a sample, most of the scattered radiation is found near the incident wavelength. This elastic scattering is known as Rayleigh Scattering. Approximately $1x10^{-7}$ of the radiation is scattered in-elastically at other wavelengths. This scattering is known as Raman scattering.

The Raman Effect occurs when a photon of a specific wavelength hits a molecule, and interacts with the electron cloud surrounding the atomic bonds in the molecule[24]. The photon excites an electron from the ground state into a virtual energy state. The electron then relaxes into an excited state, emitting a photon. This is known as Stokes radiation, and occurs at lower wavelengths then the incident photon. If the electron was already in an excited state when hit by the incident photon, as will occur in a small quantity of molecules at room temperature, it will relax back into the ground state, releasing a photon at higher wavelengths than the incident, known as Anti-Stokes radiation. Raman scattering only occurs with a change in the vibrational, rotational and electronic energy of a molecule.

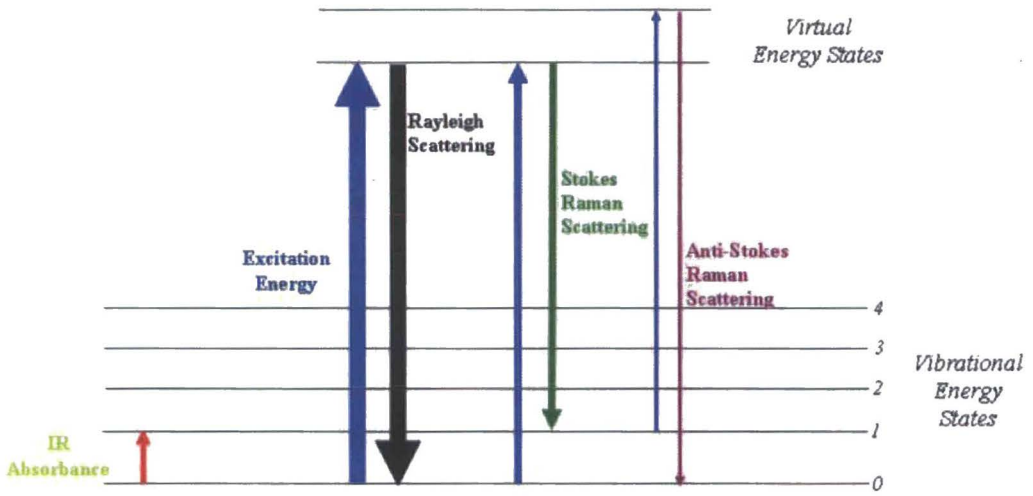

Figure 1.3.1 Simplified diagram of Raman energy levels, showing Stokes and Anti-Stokes scattering.[25]

In a modern Raman spectrometer, a laser beam is typically directed at the sample to provide the incident radiation. The scattered light from the illuminated section of material is sent through a monochromator and the Rayleigh scattering close to the incident wavelength is filtered out. The rest of the light is dispersed onto a detector, typically a Charge-Coupled Device (CCD) in modern spectrometers. As the amount of Raman radiation is typically very small, acquisition times are typically in the tens of seconds in order to collect a meaningful spectrum.

Raman spectroscopy allows characterisation of molecular bonds based on their vibrational levels. This leads to Raman spectroscopy being an extremely powerful tool for chemists, as molecular bonds can be 'fingerprinted' based on their unique vibrational energies.

The energy of a vibrational mode depends largely on the composition of the bond itself, but it will also vary based upon the molecular geometry surrounding the bond, as well as secondary effects such as hydrogen bonding. For instance, the vibrational frequency of the S-H bond is between 2500-2700 cm^{-1},

depending on molecular organization and whether hydrogen bonding effects are present[26]. This band shifts and changes intensity and shape based on the differing hydrogen bonding characteristics of the surrounding environment. The Raman S-H stretching vibration, σSH, occurs at 2525-2560 cm^{-1}, 2560-2575 cm^{-1} and 2575-2580 cm^{-1} corresponding to strong, moderate or weak S-H hydrogen bonds respectively.

The standard fingerprinting region for organic molecules is in the region between 500-2000 cm^{-1}, and most common Raman spectrometers are set up to observe this range by using a Helium-Neon 633nm laser, capable of measurements to 3200cm^{-1}. Lasers of different wavelengths can be used to image frequencies beyond this window. Biological and medical samples, for example, are typically measured in the near-infrared range using laser sources up to 1064nm. These sources can be used at lower intensities, and thus damage to the sample can be minimised[27].

1.3.1. Confocal Raman Microscopy

Conventional optical fluorescence microscopy techniques illuminate an entire sample in light and the image viewed directly, either by eye or projection. This creates issues with excited out-of-focus sections of specimens thicker then the focal plane creating glare, therefore preventing the effective resolution of depth-of-field, and thus the z-axis. Confocal microscopy, patented by Marvin Minsky in 1957[28] eliminates this problem by providing tightly-focused point illumination and a confocal pinhole to eliminate any out-of-focus information. The light beam is scanned across the sample, collecting data in a regular raster pattern and an image built out of the data collected at each point.

This technique can be readily applied to Raman spectroscopy. As Raman spectroscopy is a scattering technique, data can be collected using a tightly focused laser from very small (<1 μm) volumes of sample, both solid and in

solution. Thus, a standard confocal microscope with the addition of an incident laser and detector can be used to collect Raman spectra from surfaces in the same manner as an optical or fluorescence image is built up – by direct scanning across the surface. Chemical distributions and concentrations throughout a sample can thus be imaged directly. Confocal Raman microscopy has high lateral resolution (up to 250nm), and is heavily used for the imaging of biological samples, including cell cultures and proteins[29].

1.3.2. Surface-Enhanced Raman Spectroscopy

In 1974, Martin Fleischmann and his group carried out Raman scans of pyridine adsorbed onto an electrochemically-roughened silver substrate[30]. They noticed a large increase in the intensity of the spectra, something they attributed to a higher-than-expected surface pyridine concentration. In reality, what they were observing was surface-enhanced Raman scattering, abbreviated to SERS. This effect dramatically boosts the intensity of Raman signals of molecules absorbed on roughened metal surfaces, by up to 10^{14} in some cases.

The mechanism behind this phenomenon is still not fully understood, with two different major theories presented. One theory explains SERS using purely electromagnetic arguments, hypothesising that the roughened surfaces force surface plasmons (oscillations of free electron gas density) to lie perpendicular to a surface instead of in-plane[31]. These plasmons are excited by the incident radiation and oscillate twice, once by the light excitation and once by the surface interaction.[32]

The second major theory acknowledges this electromagnetic effect, but contends that it is not sufficient to explain the magnitude of the SERS effect. It hypothesizes that molecules with a lone pair of electrons can bond to the metallic surface, and thus the metal can act as a charge-transfer intermediate for the target molecule. As metals tend to have a conducting Fermi level positioned symmetrically around the HOMO and LUMO of the metal, the energy

required to make the spectroscopic transition for the molecule is significantly decreased through this charge transfer process[33]. Thus, incident radiation around the IR and visible light range can excite spectroscopic transitions that would usually take place at far higher energy levels.

SERS can take place at electrochemically roughened surfaces of metal, which can be prepared by performing several cycles of slow (less then 10mV/s) scan cyclic voltammetry between -2 and +2V using the metal to be roughened as the working electrode. However, SERS taking place at such surfaces often is variable both in quality of the enhancement and in reproducibility. More recent SERS experiments take place using metallic nanoparticles, either distributed over a surface substrate or in a colloidal solution[34]. These experiments show a great increase in reproducibility and in quality and are often used to obtain spectra of very small quantities of complex molecules, such as proteins, which would be impossible to collect using standard Raman.

References

[1] 'Theory of the scanning tunnelling microscope' Tersoff, J.: Hamann, D. R., *Phys.Review B.* 1985, **31,** 805-813.

[2] 'Scanning Electrochemical Microscopy. Introduction and Principles' Bard, A.J., F.-R.F. Fan *et al, Anal Che*m, 1989. **61**, 132 – 138

[3] 'Piezoelectric driven Kelvin probe for contact potential difference studies', K. Besocke, S. Berger, *Rev. Sci. Instrum,* 1976, **47,** 840.

[4] Lord Kelvin, *Philos. Mag.* 1898, **46**, 82

[5] 'Surface immobilised biochemical macromolecules studied by scanning Kelvin microprobe', L, Cheran, M Thomson, *Faraday Discuss,* 2000, **116,** 21.

[6] 'Microelectronics' Jacob Millman and Arvin Gabriel, ISBN 0-07-463736-3, Tata McGraw-Hill Edition

[7] 'A New Method of Measuring Contact Potential Differences in Metals', W. A. Zisman, *Rev. Sci. Instrum,* 1932, **3**, 367.

[8] 'Stress Dependence of Contact Potential', P. Craig, V. Radeka, *Rev. Sci. Instrum,* 1970, **41**, 258

[9] 'A critique of the Kelvin method for measuring work functions,' N A Surplice, R J D'Arcy, *J Phys E,* 1970, **3**, 477.

[10] 'Piezo-electric driven Kelvin probe for contact potential difference studies', K Besocke, S Berger, *Rev. Sci. Instrum,* 1976, **47**, 840.

[11] 'A device for measuring contact potential differences with high spatial resolution', R Butz, H Wagner, *Appl. Phys. A,* 1977, **13**, 37.

[12] 'Conditions nece ssary to get meaningful measurements from the Kelvin method', B Ritty *et al*, *J Phys E Sci Instrum,* 1982, **15**, 311.

[13] 'The effects of stray capacitance of the Kelvin method for measuring contact potential difference', R J D'Arcy *J Phys D: Appl Phys,* 1970, **3**, 482.

[14] 'Kelvin probe force microscopy', M Nonnenmacher *et al*, *Appl. Phys. Lett*, 1991, **58, 25.**

[15] 'Vacuum-compatible high-sensitive Kelvin probe force microscopy', A. Kikukawa *et al*, *Rev. Sci. Instrum.* 1996, **67,** 1463

[16] 'Scanning Kelvin nanoprobe in the tandem analysis of surface topography and chemistry', L Cheran, M Thompson, *The Analyst,* 1999, **124,** 961

[17] 'Label-free detection of nucleic acid and protein microarrays by scanning Kelvin microprobe', M. Thompson, L. Cheran *et al, Biosensors & Bioelectronics,* 2005, **20**, 1471.

[18] 'Scanning Kelvin nanoprobe detection in materials science and biochemical analysis', L Cheran, S Sadeghi, M Thompson, *The Analyst*, 2005, **130,** 1569-1576.

[19] 'Atomic Force Microscope', G Binnig, C Quate, C Gerber, *Phys. Rev. Lett,* 1986, **56,** 930.

[20] 'Traceable pico-meter level step height metrology' Orji, N, Dixson, R, *Wear,* 2004, **257,** 1264.

[21] 'Two-dimensional surface dopant profiling in silicon using scanning Kelvin probe microscopy', Henning, A, Hochwitz, T, *J. Appl. Phys,* 1995, **77,** 1888.

[22] 'Training Notebook for the Scanning Probe Microscope', Digital Instruments, 2000.

[23] The Millipede – more then one thousand tips for future AFM data storage', P Vettieger *et al, IBM J. Res. Develop.* 2000, **44**, 323.

[24] 'Practical Raman Sepectroscopy', Gardiner, D J, *Springer*, ISBN 978-0387502540

[25] *Wikipedia.* Licenced under the Creative Commons licence.

[26] 'Infrared and Raman Spectroscopy', Schrader, B. ed, *VCH Publishers*, ISBN 3-527-26446-9

[27] 'Metabolic fingerprinting in disease diagnosis: biomedical applications of infrared and Raman spectroscopy', Ellis, D I, Goodacre, R, *Analyst*, 2006, **131**, 875-885.

[28] 'Handbook of Biological Confocal Microscopy', Pawley, J.B ed, *Springer*, ISBN 038725921x.

[29] 'Confocal Direct Imaging Raman Microscope: Design and Applications in Biology', Sijtsema, N M, Wouters, S D Greve, J, *Appl. Spec,* 1998, **3,** 348-355.

[30] 'Anomalously Intense Raman Spectra of Pyridine at a Silver Electrode,' Fleischmann M, Hendra PJ, McQuillan A J, *Chem. Phy. Letters,* 1974, **26,** 163-166.

[31] 'Modern Raman Spectroscopy: A Practical Approach', Smith E, Dent G, *Wiley,* 2005, ISBN 0471497940

[32] 'Surface-enhanced Raman scattering', Campion, A.; Kambhampati, P, *Chem. Soc. Rev,* 1998, **27,** 241-250.

[33] 'Charge-transfer theory of surface enhanced Raman spectroscopy: Herzberg--Teller contributions', Lombardi, J. R.; Birke, R. L., *Journal Chem. Phys*, 1996, **84(8),** 4174-4180.

[34] 'Study of silver films over silica beads as a surface-enhanced Raman scattering (SERS) substrate for detection of benzoic acid', Mahurin L, Dai, C, *Journal of Raman Spectroscopy,* 2003, **34(5)**, 394-398.

Chapter 2: Electrochemical Techniques

Electrochemistry refers to the branch of chemistry dedicated to studying the reactions that take place at the interface of an electronic and an ionic conductor. This chapter gives an overview of basic electrochemical concepts and basic equations, before studying the common electrochemical techniques of cyclic voltammetry and electrochemical impedance spectroscopy.

2.1 Introduction

2.1.1 General Overview

Electrochemistry is the study of reactions that take place at the interface between an electronic conductor and an ionic conductor. Usually, this concerns the transport of charge across chemical phases, usually between an electrolyte, the ionic conductor, and an electrode, the electronic conductor. If an external application of potential causes the reaction to occur, or if the reaction itself causes a change in potential, then the reaction is deemed an electrochemical reaction.

Experimentally, electrochemical reactions are studied using electrochemical cells, which are defined as two or more electrodes separated by an electrolytic phase. Electrolytes are generally liquid solutions containing ionic charge carriers. However, liquid or fused salts and ionically conducting solids can be used. Electrodes can be solid or liquid, but must be metallic or semi-conducting, able to transport electronic charge easily[1].

In general, electrochemical reactions are redox (reduction/oxidation) reactions separated in space. The overall chemical reaction occurring in an electrochemical cell, therefore, is made up of two half-reactions taking place at

the two electrode interfaces. Consider an electroactive compound in both oxidised and reduced forms represented by O and R. The two species can change into each other by the transfer of electrons as shown below;

$$O + ne^- \leftrightharpoons R$$

The working electrode is the electrode used to investigate the half-reaction taking place at its tip, often by varying its interfacial potential. The other electrode is typically a standard counter electrode, and is not typically measured. To measure reactions, the working electrode's potential is driven either negatively, raising the mean energy, the Fermi level, of the electrons in the electrode so that they eventually transfer into vacant spaces in the electrolytic species (a reduction current), or positively, lowering the Fermi level so that electrons flow from the electrolyte to the electrode (an oxidation current).

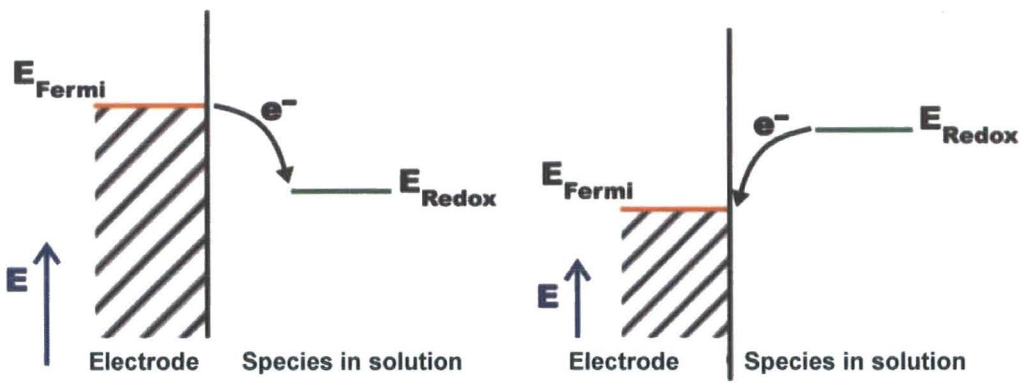

Figure 2.1.1.1 Fermi levels at electrode surfaces for reduction of species (left) and oxidation (right)

To measure the changes occurring at the working electrode accurately, a reference is needed. This reference electrode is constructed using phases known to have a constant makeup, and which will thusly provide a reproducible reference. This provides a fixed potential, and therefore when the reference electrode is present in a cell any changes in the cell can be shown to be due to the working electrode. The standard reference electrode is the standard

hydrogen electrode (SHE), which is based on the redox half-cell $2H^+(aq) + 2e^- \rightarrow H_2(g)$. This electrode requires the use of gaseous hydrogen, and is therefore not practical for most experimental situations. Instead, electrodes with different compositions are used, and their potentials quoted relative to the standard hydrogen electrode.

There are two major types of electrochemical cells. Galvanic cells are cells in which an electrochemical reaction will occur spontaneously at the electrodes when they are conductively connected. These kinds of cells are mostly used for energy storage, and form the basis of both rechargeable and non-rechargeable batteries, as well as fuel cells. An electrolytic cell is a cell in which reactions are induced at the electrodes by the application of an external voltage[2]. These cells are used for producing aluminium industrially, as well as processes such as electroplating.

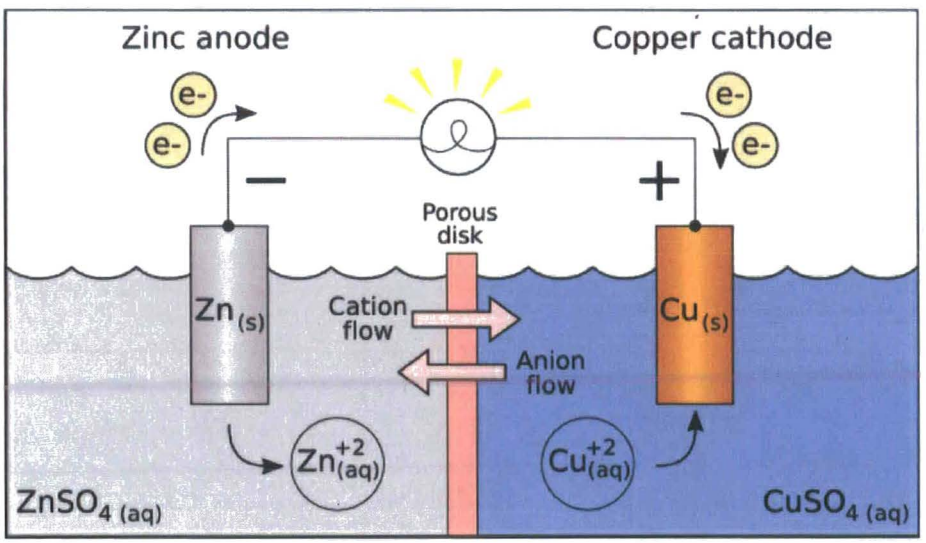

Figure 2.1.1.2 $ZnSO_4/CuSO_4$ galvanic cell.[3]

2.1.2 The Electrical Double Layer

The processes that occur at an electrode's surface can be divided into two sections, Faradaic and non-Faradaic. Faradaic processes are those in which

electrons transfer across the electrode/electrolyte interface. These reactions obey Faraday's Law, which states that the mass of a substance produced at an electrode during electrolysis is proportional to the number of moles of electrons transferred at that electrode[4]. This charge transfer allows the reduction or oxidation reaction to occur, and therefore Faradaic processes are of most use to the electrochemist. However, processes such as adsorption and desorption, as well as the accumulation of charged particles at an electrode surface can occur. These events cause currents to flow through the electrolyte, though not through the interface, and therefore are known as non-Faradaic processes.

When charge does not pass through an electrode interface, and only non-Faradaic processes are occurring, the interfacial region between the electrode and the electrolyte has been shown to behave like a capacitor. This occurs because the electrode has a different potential to the electrolyte, and thus charge builds up both on the electrode surface (in a very thin layer, less than an angstrom in thickness) and in the surrounding electrolyte, expressed as an excess of ions holding an opposing charge to the electrode surface. This structure of opposing charges is known as the electrical double layer.

Hermann von Helmholtz in 1853 was the first to treat the double layer mathematically as one capacitor. Gouy and Chapman later improved on this model in 1913 by adding a diffuse layer to Helmholtz's single capacitor. The present model was refined further by Stern in 1924 and is known as the Gouy-Chapman-Stern model.

The double layer contains several components. The inner layer, also known as the inner Helmholtz plane or Stern layer, is made up of electrolytic and other species specifically adsorbed to the electrode surface at a distance x_1 and a charge density σ^i. Solvated ions can only approach to a distance x_2 due to the presence of the adsorbed species, these make up the outer Helmholtz plane and are non-specifically adsorbed, interacting with the electrode surface only through long-range electrostatic forces. These species are distributed in a three-dimensional pattern from the outer Helmholtz plane to the bulk of the solution,

known as the diffuse layer and possessing a charge density of σ^d. The total excess charge density can therefore be expressed as $\sigma^S = \sigma^d + \sigma^i$, and is equal and opposite to the charge on the electrode surface.

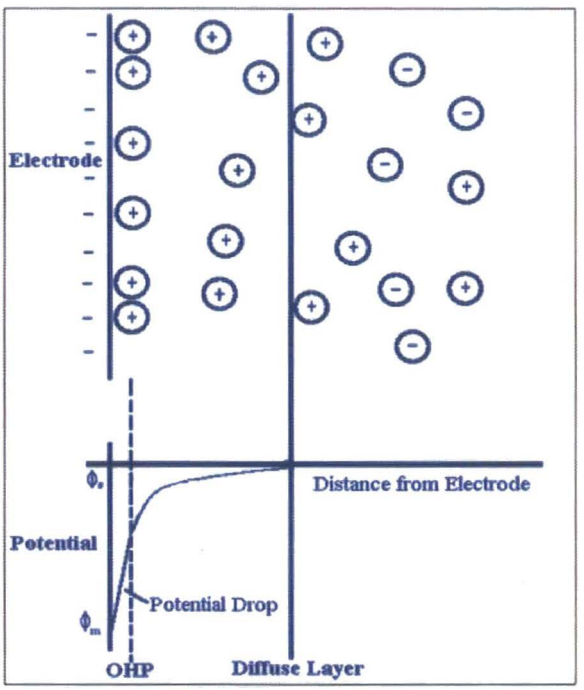

Figure 2.1.2.1 Diagram of the electrical double layer, showing the IHP and OHP, as well as the diffuse layer.[3]

The double layer can affect the rates of Faradic charge-transfer processes, and therefore reaction rates. As there is a small potential drop across the double layer caused by electrokinetic effects, and the electroactive species can only approach to the outer Helmholtz plane, the double layer has a measurable effect on electrochemical reactions and its presence should not be discounted.

2.1.3 Half-cell potentials and the Nernst equation

An electrochemical reaction in a cell is made up of two half-reactions occurring at the cathode and anode. Each half-cell reaction therefore has a potential difference at the electrode-electrolyte interface, E, which depends on the

nature and concentration of the electroactive species. Half-cell potentials are recorded relative to the SHE and always in the reduction direction of the reaction. These standard reduction potentials or electro-motive forces (EMF) are denoted by the symbol E^0 and are recorded in volts. The cell potential can be simply calculated by adding the reduction potential for the reduction half-cell to the negative of the reduction potential (therefore the oxidation potential) of the oxidation half-cell.

The more positive the cell potential, the greater the tendency for the reaction to take place, and therefore the greater the amount of free energy (ΔG) in the system. As free energy measures the amount of useful work that can be extracted from a system to the surroundings, E and ΔG measure the same quantity, and are related by the equation

$$\Delta G = -nFE \tag{1}$$

Where n represents the number of electrons transferred and F represents the Faraday constant. This can now be substituted into the equation

$$\Delta G = \Delta G^0 + RTlnQ \tag{2}$$

Where Q is the reaction quotient, a qualitative measure of the extent to which a reaction will occur, R is the gas constant and T is the temperature.

$$nF\Delta E = nF\Delta E^0 - RTlnQ \tag{3}$$

This can be rearranged into:

$$\Delta E = \Delta E^0 - \frac{RT}{nF} lnQ \tag{4}$$

This is named the Nernst equation, after its formulation by the German chemist Walther Hermann Nernst in the early 1900s. This equation successfully relates the electrode potential E to the standard electrode potential E^0 and therefore is of great use to electrochemists.

2.1.4 Kinetics of Electrode Reactions

Electrochemical cells measure current – the current being proportional to the rate of the electrochemical reaction and therefore to the concentration of the electroactive species. Therefore, two species, A and B, which react in a simple unimolecular electrode reaction,

$$A \leftrightharpoons B \tag{5}$$

With forward rate constant k_f and backward rate constant k_b, the reaction has a net reaction rate v_{net} of

$$v_{net} = k_f C_A - k_b C_B \tag{6}$$

Where k_f and k_b are the forward and backward rate constants respectively and C_A and C_B are the concentrations of the two species. The reaction rate v can be related to the current i by the equation

$$v = \frac{i}{nFA} \tag{7}$$

Where A is the area of the electrode in cm^2. Therefore, the net current density i_{net} can be expressed as

$$i_{net} = nFAk_f C_A - nFAk_b C_B \tag{8}$$

The current density is an exponential function of the potential of the cell. This is due to the relationship between the current and the rate constant, which is related to the free energy of activation $\Delta G^{\ddagger}$ by the modified Arrhenius equation[5];

$$k = A' e^{\frac{-\Delta G\ddagger}{RT}} \quad (9)$$

Where A' in this case is a coefficient known as the frequency factor, a factor related to the probability of surmounting the potential energy barrier.

Understanding this, it is now possible to relate the current density to the potential of the reference electrode, using the Nernst equation, as follows;

$$i = nF\left[k_f^0 C_O \exp\left(-\frac{\alpha nFE}{RT}\right) - k_b^0 C_R \exp\left(-\frac{(1-\alpha)nFE}{RT}\right)\right] \quad (10)$$

The symmetry coefficient, represented by α, is a reflection of the sensitivity of the transition state of the reaction to the voltage applied in the electrochemical cell. If α=0, then the transition state shows no dependence to potential. In a standard reversible electrochemical reaction α~0.5, indicating that the transition state responds to applied potential in a manner which is half-way between the response of the reactant and the product.

As shown before, the net current is a product of two different reactions A→B and B→A, with two different rate constants k_f and k_b. The potential of the electrochemical cell controls the rate of reaction, and therefore at a certain potential k_f and k_b are equal, and can be expressed simple by one heterogeneous rate constant k^0. This means that rate constants at other potentials can be expressed in terms of k^0 as follows;

$$k_1 = k^0 \exp\left(-\frac{\alpha nF\left(E_{eq} - E^0\right)}{RT}\right) \quad (11) \quad \text{and}$$

$$k_2 = k^0 \exp\left(-\frac{(1-\alpha)nF\left(E_{eq} - E^0\right)}{RT}\right) \quad (12)$$

Where E_{eq} is the equilibrium potential for the electrode system. This can now be written in terms of current density as;

$$i = nFk^0\left[C_O \exp\left(-\frac{\alpha nF\left(E_{eq}-E^0\right)}{RT}\right) - C_R \exp\left(-\frac{(1-\alpha)nF\left(E_{eq}-E^0\right)}{RT}\right)\right] \quad (13)$$

At equilibrium, the cathode and anode would have equal current densities, as the rate constants are identical for the forwards and backwards reactions. This can be reflected in the flowing equation;

$$nFk^0C_O \exp\left(-\frac{\alpha nF\left(E_{eq}-E^0\right)}{RT}\right) = nFk^0C_R \exp\left(-\frac{(1-\alpha)nF\left(E_{eq}-E^0\right)}{RT}\right) \quad (14)$$

This is the Butler-Volmer equation, which is the fundamental relationship between the voltage applied and the current which flows inside an electrochemical cell.

The quantity E_{eq}-E^0 represents the activation energy required to force current flow. In a well-mixed solution, one with equal bulk and surface concentrations, mass transport effects do not complicate electrolysis. In an equilibrium situation where C_o and C_R are identical, net current flow would therefore be zero. Even though this is the case, balanced Faradaic activity can still be envisaged as the exchange current, i_0. This is related to k^0 by the simple relationship:

$$i_0 = nFk^0C \quad (15)$$

The Butler-Volmer equation therefore simplifies to:

$$i = i_0\left\{e^{\frac{-\alpha nF(E_{eq}-E^0)}{RT}} - e^{\frac{(1-\alpha)nF(E_{eq}-E^0)}{RT}}\right\} \quad (16)$$

This equation is known as the current-overpotential equation. Since mass-transfer effects are irrelevant in a well-mixed solution, the overpotential associated with the current serves solely as activation energy. It is therefore possible to investigate the kinetics of reactions with different values of i_0, the

larger the value of i_0, the larger the current change will be on the variation of E_{eq}-E^0, and the quicker the kinetics of the reaction.

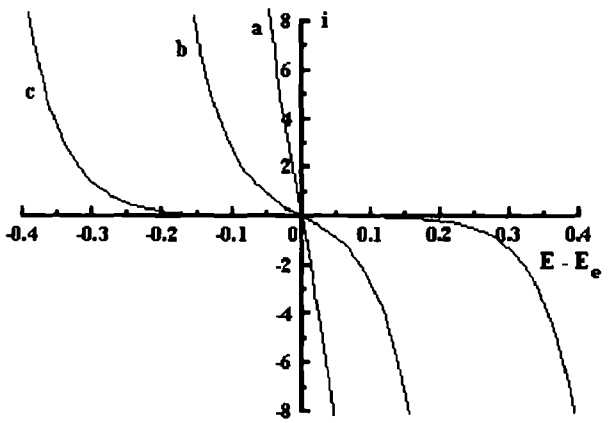

Figure 3.1.4.1 Graph showing the effect of i_0 on electrode kinetics.

Each curve on the graph above passes through zero, showing that when E_{eq}-E^0 equals zero then no current flows – the cell is in equilibrium. When E_{eq}-E^0 is changed, however, the value of i_0 influences the current response. The curve (a) shows the response when i_0 is large – a large current change is observed on a small variation of E_{eq}-E^0. This shows that the activation barrier to the redox reaction occurring is very small, and the reaction is therefore a reversible one. Curve (c) shows a classically irreversible reaction, where the current response is much smaller over the same variation of E_{eq}-E^0. This shows a large required overpotential and therefore a high barrier to activation – therefore slowing the rate of reaction and making reversal greatly more difficult. Curve (b) shows intermediate behaviour, and therefore a quasi-reversible reaction, a reaction that will reverse, but with more limited intensity.

The overpotential of a system can be defined by η. The Tafel equation relates the rate of an electrochemical reaction to the overpotential. It is a limiting case of the Butler-Volmer equation, applied to high overpotential systems. On a single electrode (the Tafel equation is applied to each electrode separately), the Tafel equation is;

$$\eta = \frac{RT}{\alpha nF} ln i_0 - \frac{RT}{\alpha nF} ln i \tag{17}$$

This simplifies down to;

$$\eta = a + b\ log i \tag{18}$$

Where a and b are characteristic constants of the electrode system. A provides information about the rate constant and the exchange current density of the reaction, and b is the 'Tafel slope', which provides information about the mechanism of the reaction.

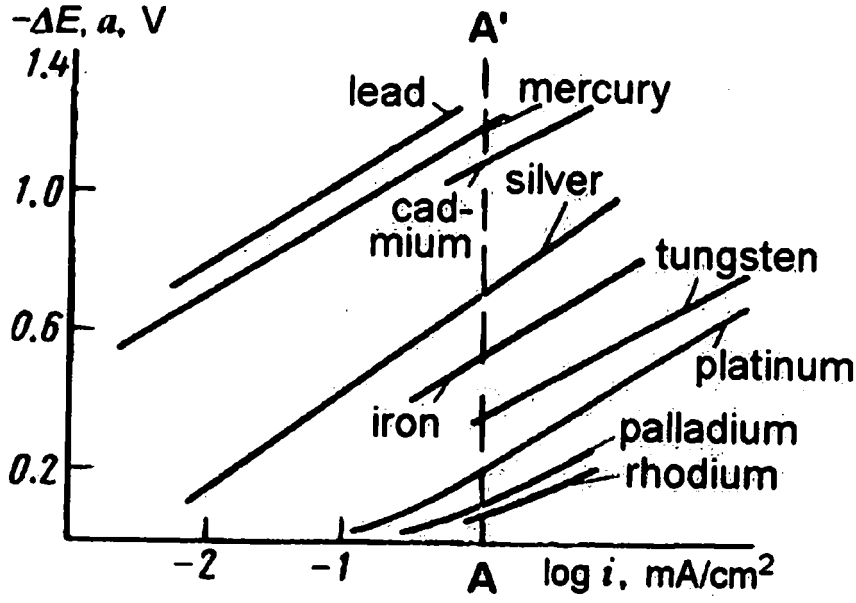

Figure 3.1.4.2 Tafel plot of hydrogen evolution at a number of metals in an acidic solution. The line AA' is drawn at i=1mAcm^{-2}. As can be seen by the linear responses, the Tafel equation holds for most of these reactions.

A plot of log iv s η is known as a Tafel plot, with a being the intercept and b being the slope of the line. If the Tafel plot shows a straight line, then the reaction obeys the Tafel eqaution. In this way, Tafel plots can be used to investigate non-reversible reactions and non-equilibrium conditions in a way that Nernstian kinetics cannot.

2.2 Cyclic Voltammetry

2.2.1 Introduction

Cyclic voltammetry is a type of potentiometric electrochemical measurement, widely used due to its simplicity, speed, ease of use and ease of interpretation. A standard cyclic voltammetry experiment takes place in a three-electrode cell, using working, reference and counter electrodes. Cyclic voltammetry electrochemical cells usually contain the electroactive compound to be studied in solution, often along with a non-reactive electrolyte such as KNO_3 or KCl to facilitate ionic transport. A potential is applied to the working electrode, and the Faradaic current response at the working electrode is measured. The potential at the working electrode is then changed as a function of time, with scan rate v in mV/s. This potential is generally swept from the starting potential to a fixed endpoint (often known as a switching potential) and then back in a triangular waveform. More complicated cyclic voltammetry experiments will sweep the potential through three or more ending points and repeat the waveform for a number of cycles.

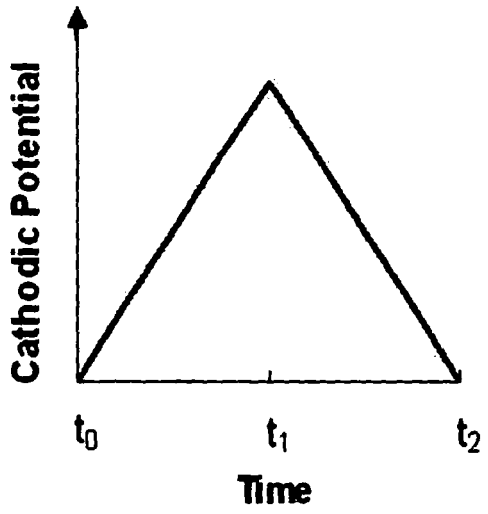

Figure 2.2.1.1 Triangular potential/time waveform for standard two-point cyclic voltammograms. The voltage is swept linearly from a start to an end potential and then back.[3]

As the working electrode is swept through the potential range, the potential applied to the electrode may prove sufficient to cause any electrochemical species present to undergo electron-transfer reactions. Consider a redox couple, O and R. Before the scan begins, the electrochemical cell will contain mostly the reduced form R. As the working electrode is swept through the redox potential, some of O is converted into R and a Faradaic current flows, increasing exponentially as the potential is neared. This is due to the surface concentration of R on the electrode – as the redox potential is neared, it drops, increasing the concentration gradient and thus the current flow. As the potential passes through the redox potential, mass transfer of R to the surface reaches a maximum rate, declining past this point due to depletion. A reversal current peak is seen when the potential is swept in the opposite direction, as the oxidised species O at the electrode surface gets converted back into R. The result is a curve as shown in Figure 3.2.1.2.

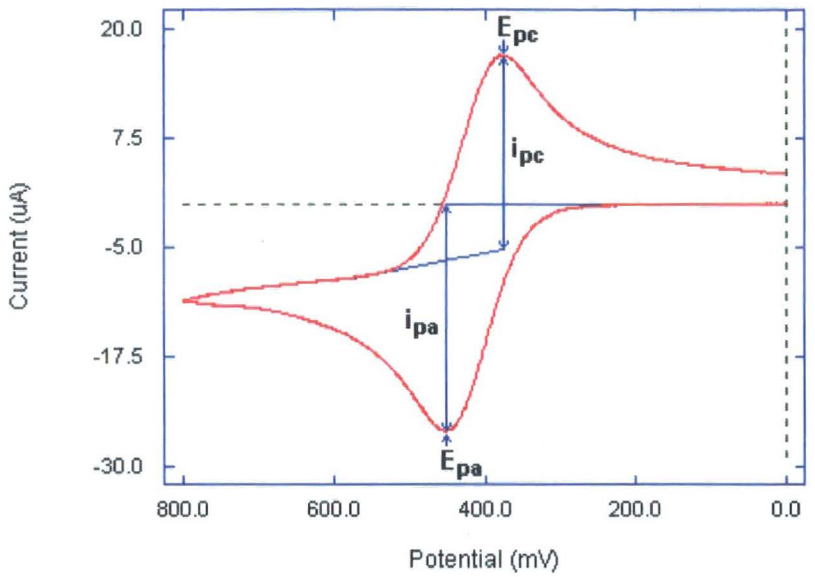

Figure 3.2.1.2 Sample current (i) vs potential (v) graph of a cyclic voltammetry scan of a reversible electrochemical reaction. The two peaks represent the oxidation and reduction potentials of the compound under investigation.

If a redox system remains in equilibrium throughout the CV, resulting in two peaks of equal height, then the reaction is known as reversible. This is an example of a standard reversible cyclic voltammogram. There are a number of powerful analysis methods to obtain data relating to the kinetic and mechanistic features of the reaction.

2.2.2 Reversible cyclic voltammetry scans

Consider a standard cyclic voltammetry scan of a typical reversible electrochemical reaction as introduced above. To begin the scan, the potential of the working electrode is held at a point E_i, where no reaction will occur. When the scan is begun, the working electrode potential is swept linearly at scan rate *v*, allowing the potential at any point to be expressed as

$$E_t = E_i - vt$$

Where E_t is the potential at time t. On the backward sweep of the reaction, the potential can be expressed as:

$$E_t = E_i - 2v\lambda + vt$$

Assuming the reaction follows diffusion-controlled Nernstian kinetics, and that the rate of reaction is very fast compared to the scan rate, then the concentration of reduced and oxidised species will vary at different scan rates according to the Nernst equation –

$$E = E^0 + \frac{RT}{nF} ln \frac{Co}{Cr}$$

Where Co and Cr are the surface concentrations of the oxidised and reduced species respectively. Fick's Second law of Diffusion will hold assuming the reaction is diffusion-controlled, as is standard in a cyclic voltammetry setup. Assuming this is the case, the peak current at equilibrium conditions is given by the Randles-Sevcik equation:

$$i_p = 2.69 \times 10^5 n^{3/2} A. D_O^{1/2} v^{1/2} C_O$$

Where i_p is the peak current, A is the electrode area in Cm^2, D is the diffusion coefficient in cm^2s^{-1} and C_o is the concentration of the oxidant in $molcm^{-3}$.

From the Randles-Sevcik equation, it can be seen that ip is directly proportional to the concentration of the reactant and proportional to the square-root of the scan rate when the reaction is completely reversible. This is due to the electrode diffusion layer – the faster the scan, the less time it has to grow, and therefore the greater flux toward the electrode surface. As the current is proportional to the flux at the electrode surface, a faster scan rate leads to greater current.

A reversible electrochemical reaction following Nernstian kinetics should therefore show the following properties when a cyclic voltammetry scan is undertaken.

1. The peak potential separation – the difference between the potential at which peak current is observed on the forward and reverse sweeps – should be 57/n mV where n is the number of electrons transferred during the electrochemical redox reaction.

2. The width of the peak should be equal to 28.5/n mV, whatever scan rate is used in the sweep.

3. The ratio between the forward and reverse peaks should be equal to 1 for all scan rates.

4. The peak current is directly proportional to the square root of the scan rate.

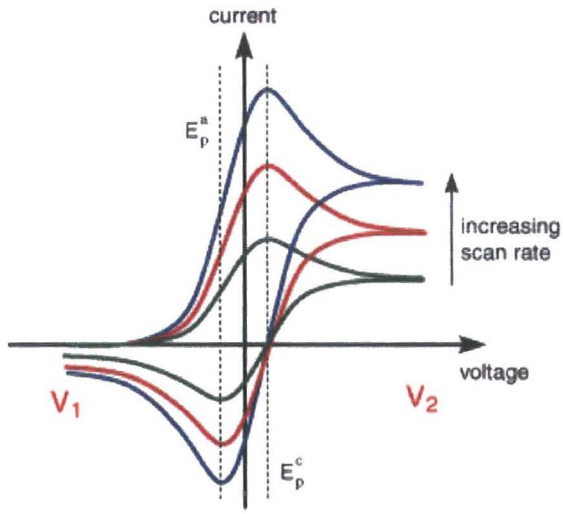

Figure 2.2.2.1: Effect of increasing scan rate upon peak current for a fully-reversible cyclic voltammetry sweep. (Cambridge CREST)

For a fully-reversible cyclic voltammetry sweep, the heterogeneous electron transfer rate k_s is extremely fast compared to the scan rate. When the electron transfer rate constant decreases, either due to slow diffusion to the electrode surface or to chemical processes coupled to the electrochemical reaction, then uneven cyclic voltammograms are observed. These are referred to as quasi-

reversible or irreversible reactions, depending on the severity of the asymmetry observed in the cyclic voltammogram.

2.2.3 Quasi-reversible and irreversible cyclic voltammetry scans

When the rate constant of the electrochemical reaction reduces, there will not be high enough concentrations generated at the electrode surface for Nerstian kinetics to be applicable. This occurs due to the kinetics of the reaction being too slow compared to the scan rate to establish the equilibrium of oxidised and reduced products. When this happens, the peak currents become reduced and shift further apart in potential, needing more time to adjust in the change in applied voltage, until the peak current can no longer be calculated as the square-root of the scan rate.

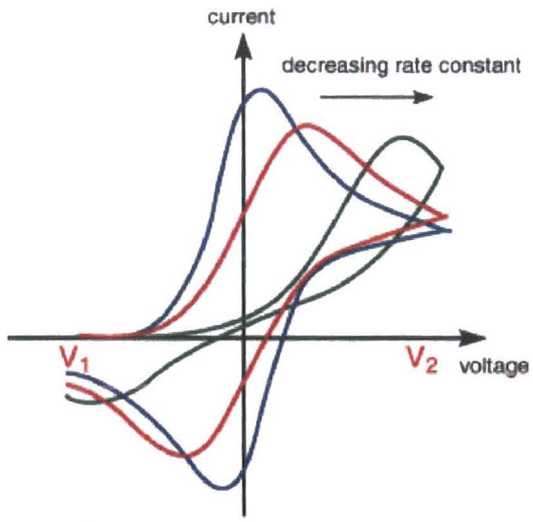

Figure 2.2.3.1.1: Figure showing the effect of decreasing electrochemical rate constant on the shape of a cyclic voltammogram. (Cambridge CREST)

By analysing the variation in peak position as a function of scan rate relative to the fully-reversible Nernstian situation, it is possible to estimate a value for the heterogeneous electron rate transfer constants.

Rate constants can be affected by many environmental factors – whether the electrode is clean or fouled, any interfacial films slowing mass transport, the composition of the solution and whether it is well mixed and stirred – but non-reversible CVs are usually seen when there is a chemical component to the reaction, occurring usually after an electrochemical reaction. The two most common types of coupled reaction types are EC and ECE, where E denotes an electrochemical and C a chemical step in the reaction.

2.2.3.2: The EC mechanism

An EC mechanism is simply an electrochemical reaction, characterised by an initial electrochemical step in which electrons are transferred at an electrode surface, followed by a chemical step in which the electrode is not involved, as shown below;

$$O + e^- \rightleftharpoons R \qquad (E)$$

$$R \rightarrow A \qquad (C)$$

The electrochemical reaction and the chemical reaction will have different reaction rates, the fast heterogeneous electron transfer rate with rate constant k_s at the electrode surface and the chemical reaction rate, usually characterised by a homogeneous first-order rate constant k_{EC}. An example of this mechanism can be seen in the electrochemical oxidation of ascorbic acid and the reaction with the water used as a solvent to yield dehydroascorbic acid, an electrochemically inactive substance.

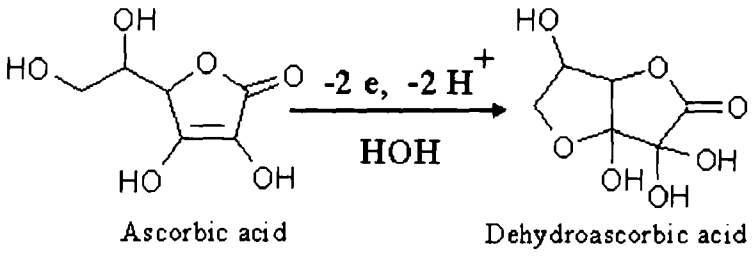

Figure 2.2.3.2.1: Figure showing the EC-mechanistic reaction that occurs when ascorbic acid is electrochemically oxidised.

When a cyclic voltammogram is taken of a reaction following an EC mechanism, then the speed of the chemical rate constant k_{EC} relative to the scan rate v determines the shape of the curve. The faster the chemical reaction, the more material will have move from an electrochemically-active to an electrochemically-inactive condition, and therefore the smaller the amount of material will be available for the reverse potential sweep. This lessens the magnitude of the reverse current peak and shifts the peak towards more reductive potentials. By measuring the ratio of the height of the back peak to the forward one and plotting a curve of ratios at various scan rates, k_{EC} can be estimated.

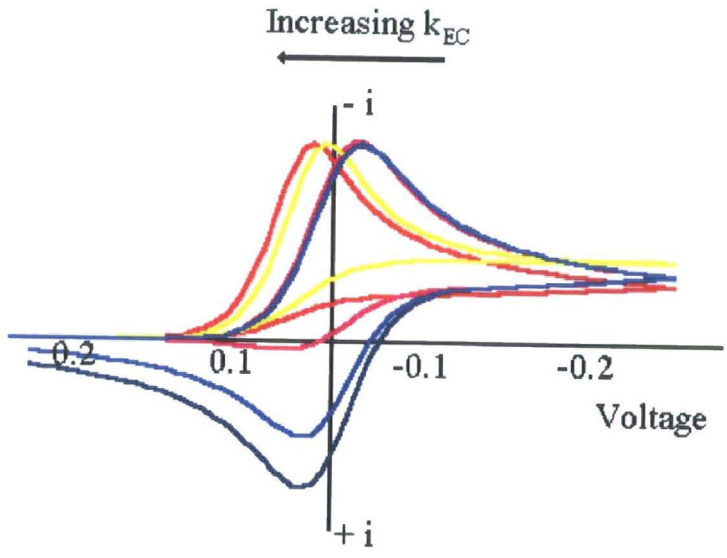

Figure 2.2.3.2.2: Graph showing the effect of increasing k_{EC} on the shape of the measured cyclic voltammogram.

A similar mechanism, the EC' mechanism, is a case in which a catalytic mechanism regenerates the starting oxidative product, resulting in greater and greater forward peaks, relative to the amount of catalyst added.

$$O + e^- \leftrightarrow R \qquad \textbf{(E)}$$

$$R + Y \rightarrow O + \text{Products} \qquad \textbf{(C')}$$

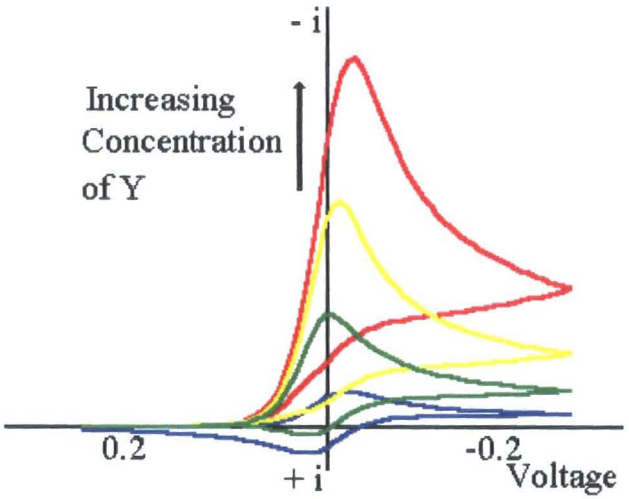

Figure 2.2.3.2.3: Graph showing the effect of the EC′ mechanism on the shape of the cyclic voltammogram, relative to the quantity of Y added.

2.2.4 Electrochemical simulations

Qualitative information gathered from cyclic voltammetry scans, such as the quantity of electrons transferred, the stability of the oxidation states and the overall kinetics of the reactions can be easily inferred from simple studies of the voltammograms. Quantitative studies, such as exact figures for diffusion and rate constants, often require computational simulation and fitting, due to the large number of repetitive calculations required to obtain accurate values.

Two popular computer programs used in this field are Digisim[6], published by Bioanalytical Systems Inc, and Digielch[7], published by Elchsoft. Both pieces of software can simulate cyclic voltammograms from any user-defined electrochemical mechanism, which can be composed of both charge-transfer processes and first- and second- order chemical reactions. They both rely on the fast implicit finite difference (FIFD) algorithm developed by Manfred Rudolph[8]. This represents any electrochemical mechanism as a set of tridiagonal matrix equations, which can then be solved by a matrix-version of the back-forward substitution algorithm[9]. This allows experimental voltammograms to be fitted

by a series of iterative steps to the simulated curve created by the FIFD algorithm.

2.3 Electrochemical Impedance Spectroscopy

2.3.1 Introduction

Electrochemical impedance spectroscopy is a rapidly-developing and powerful technique for investigating the functionalisations of electrode surfaces, as well as uses in corrosion and defect studies. It is based on electrical impedance, a concept similar to electrical resistance. Resistance is calculated using the well-known Ohm's law, E=IR. This relationship, however, only encompasses ideal resistors, which are never usually found in the real world. Like resistance, impedance is a measure of a circuit to resist the flow of electrical current through it. Unlike the concept of resistance, it is able to more accurately reflect real-world conditions.

Electrochemical impedance aims to describe the response of a circuit to ac current or potential as a function of frequency. Impedance is usually measured by the application of an ac potential, called the excitation signal, to an electrochemical cell and measuring the resultant current[10]. This resulting current signal is also ac, and will contain the excitation frequency and its harmonics.

Impedance is at its simplest described as an analogous equation to Ohm's Law,

$$E=I.Z \qquad (19)$$

Where Z is the impedance, which is measured as a two-dimensional, vector quality. If the applied ac potential is sinusoidal, then the resulting current would also be sinusoidal, with the attendant harmonics also seen.

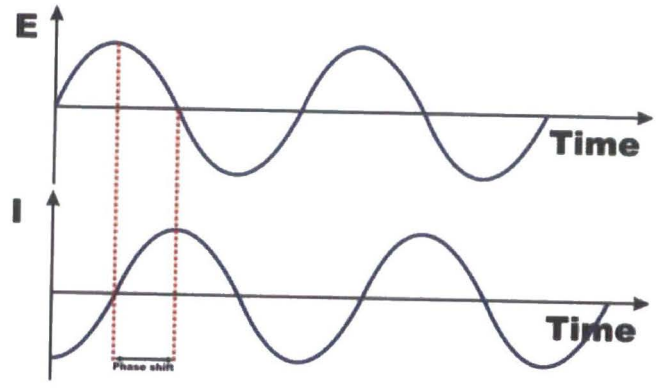

Figure 2.3.1.1 Figure showing the relationship between an applied ac potential E and the resultant current I.

For the diagram above, the equation for the applied potential is:

$$E(t) = E_0 \sin(\omega t) \tag{20}$$

Where

E(t) is the voltage as function of time (V)

E_0 is the voltage amplitude (V)

ω is the angular frequency (rad / s = $2\pi f$)

f is the frequency (Hz)

t is the time (s).

The resulting current equation is therefore:

$$i(t) = i_0 \sin(\omega t + \phi) \tag{21}$$

Where,

I(t) is the current as function of time (A)

I_0 is the maximum current amplitude (A)

ϕ is the phase shift (rad).

Impedance can therefore be expressed as;

$$Z = \frac{E(t)}{I(t)} = \frac{E\cos(\omega t)}{I_0\cos(\omega t - \phi)} = Z_0\frac{\cos(\omega t)}{\cos(\omega t - \phi)} \quad (22)$$

The impedance can therefore be expressed as a magnitude, Z_0, and a phase shift, f. This is a vector measurement, where the magnitude and direction of the vector can be expressed by the sum of the components. At each measured point the data consists of both the real and imaginary components of the applied potential and the measured circuit. Therefore, the impedance vector can be expressed as;

$$Z(\omega) = Z' + jZ'' \quad (23)$$

Where Z' and Z'' are the real and imaginary components respectively of the impedance vector Z. j is the imaginary multiplier √1, represented here by j instead of the more usual i to avoid confusion with the standard current representation.

2.3.2 Equivalent Circuits

For the case of a perfect resistor, the two curves would be directly aligned, with no phase shift. The magnitude of the impedance Z will therefore equal R, and ϕ will equal zero for all applied frequencies.

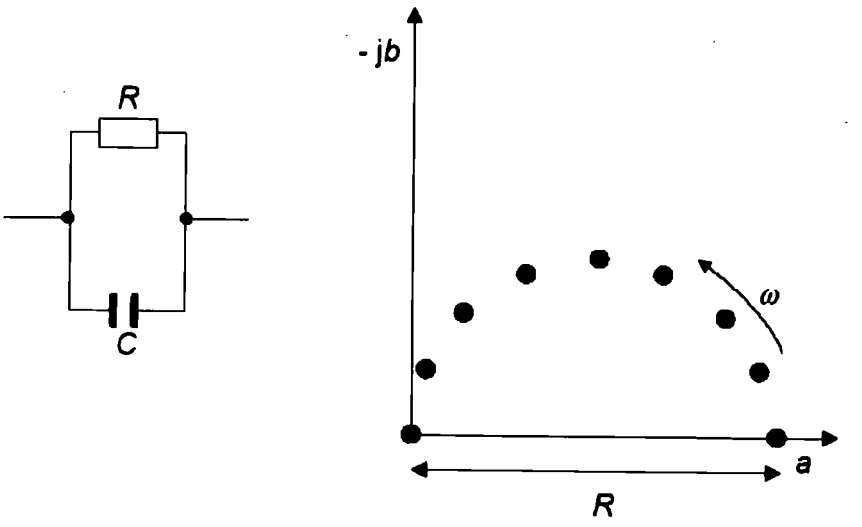

Figure 2.3.2.1 Nyquist plot of a purely resistive system.(Solartron)

For the case of a purely capacitive system, the impedance is now completely dependent on the frequency, which is defined by the relationship $Z=1/\omega C$, and a phase angle of 90°. This leads to a decrease in impedance with an increase in frequency.

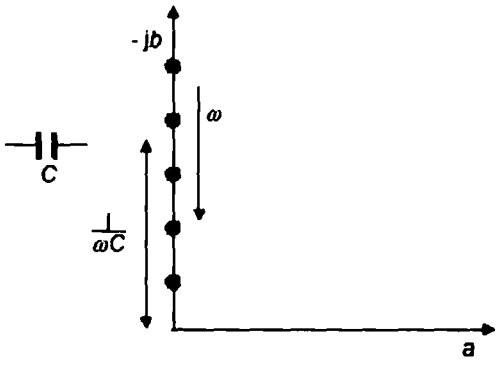

Figure 2.3.2.2 Nyquist plot of a purely capacitive system.(Solartron)

A real-world impedance system can therefore be modelled as a system of capacitors and resistors. The total impedance in a circuit is equal to the combined opposition to the electron flow of all resistors, capacitors and inductors in the circuit. This is known as an equivalent circuit, and can be used to deduce specific values for resistive and capacitive values from an impedance graph. A set of impedance results can be fitted to an equivalent circuit, and known values substituted in order to deduce values for unknown capacitive and resistive components of the circuit.

When constructing an equivalent circuit for a three-electrode system, several factors must be considered. The first is the solution resistance between the working and reference electrodes. The solution resistance is usually calculated from the solution conductivity, commonly represented by κ. And given in units of Siemens per metre (Sm^{-1}) Its relation to the solution resistance is given by;

$$R = \frac{1}{\kappa}.\frac{1}{A} \tag{24}$$

Which rearranges to:

$$\kappa = \frac{1}{RA} \tag{25}$$

Where A is the area and R the solution resistance. Practically, this calculation is difficult given the often non-uniform current distribution and electrolyte

makeup in a typical electrochemical cell. This resistance is therefore usually found through electrochemical impedance measurement and equivalent circuit fitting.

The double-layer capacitance is also a factor, although a relatively insignificant one. The expectation is that roughly 30 μF of capacitance should be expected for every cm^2 of bare metal immersed in an ionic electrolyte.

Polarisation resistance, R_p, caused by the electrode resisting the change of potential from away from the open circuit value, can be calculated from a derivation of the Butler-Volmer equation, as seen below;

$$I_{corr} = \frac{\beta_a \beta_c}{2.303(\beta_a + \beta_c)} \cdot \frac{1}{R_p} \tag{26}$$

where β_a and β_c are the anodic and cathodic Beta coefficients, measured in volts/decade.

Charge-transfer resistance, R_{ct}, created by the mechanism of an electrochemical reaction, can also be calculated by a derivative of the Butler-Volmer equation, given below;

$$R_{ct} = \frac{RT}{nF i_0} \tag{27}$$

Where F is Faraday's constant and i_0 is the exchange current density.

At high frequencies, the double-layer capacitance conducts easily, which mostly negates the charge-transfer resistance. The conduction of the double-layer capacitance drops with lower frequencies, causing the charge-transfer resistance response to increase. As the frequency approaches zero, the cell impedance becomes a function only of the charge-transfer resistance, plus any other resistive effects in the system.

An additional element, Warburg impedance, occurs due to diffusion. This is a complex element having both real and imaginary components, and is proportional to the reciprocal of the square root of the frequency, 1/Vw. This can be seen on a Nyquist plot as a straight line of gradient 0.5, and is a commonly-seen aspect of almost all impedance readings.

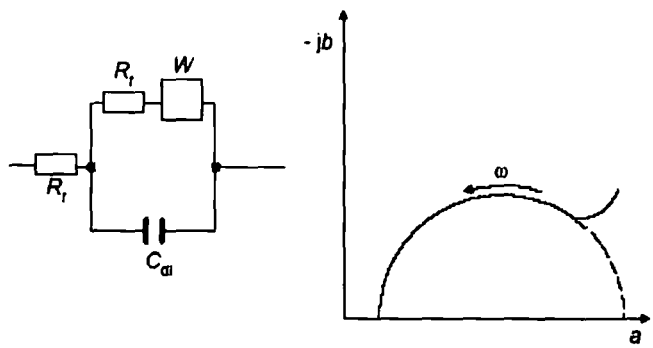

Figure 2.3.1.4 Argand diagram showing Warburg-distorted impedance scan

Typically, the low-frequency region of an impedance scan contains information related to diffusion and charge transfer resistances, and the high frequency region providing the solution resistance. Impedance is commonly represented as Nyquist plots, which plot the real impedance, Z, against the negative imaginary impedance, -Z', on a logarithmic scale. The impedance can be measured directly as a vector Z with frequency f determined by the angle between the vector and the z-axis.

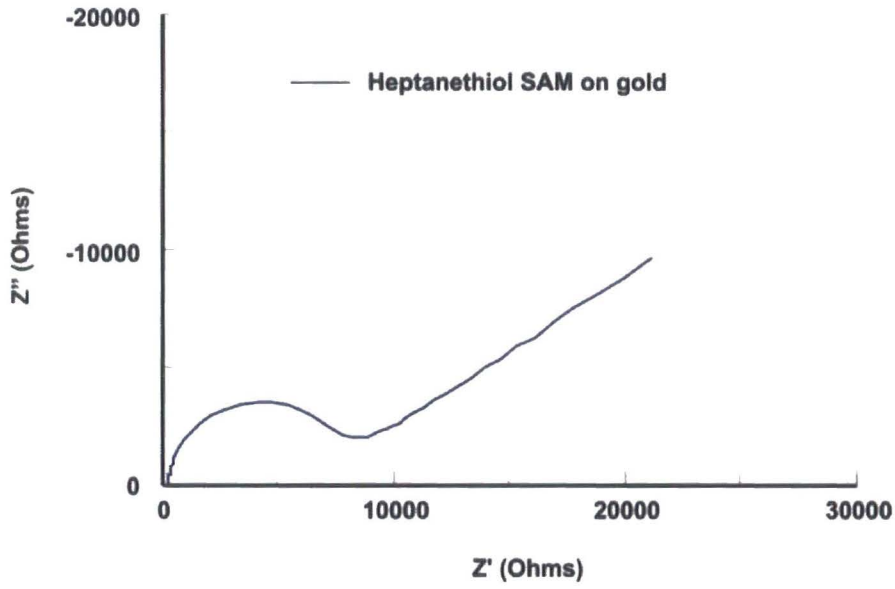

Figure 2.3.1.5. Example Nyquist plot of a monolayer of 1-heptanethiol on a gold working electrode.

The Bode plot is also commonly used to represent impedance. These are plotted with the log of the frequency on the x-axis and both the absolute value of Z and the phase-shift on the y-axis. The Nyquist plot cannot show frequency information for a specific point, whereas the Bode plot can, but at a loss of clarity for the overall reaction.

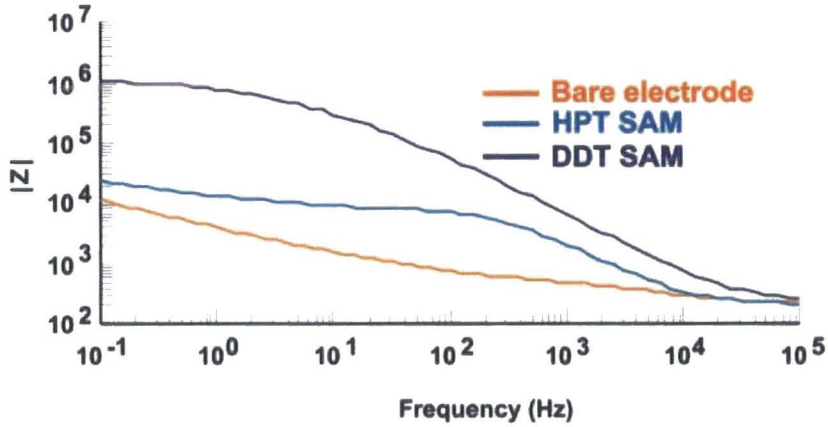

Figure 2.3.1.6. Example Bode plot comparing three impedance scans: a bare gold working electrode, a monolayer of 1-heptanethiol and a monolayer of 1-dodecanethiol.Provided by Francisco Aguiar, Durham University.

As Nyquist plots generally have greatly differing scales for different reactions, it is difficult to directly compare readings using them. The structure of a Bode plot, however, allows multiple reactions to be compared directly. Generally, both plots are given simultaneously when presenting impedance data.

References

[1] 'Electrochemical Methods: Fundamentals and Applications', Bard, A J, Faulkner, L R, *Wiley*, 1980, ISBN 0471055425

[2] 'Physical Chemistry, 7th Edition', Atkins P W, De Paula, J. *Oxford University Press*, 2002, ISBN 0198792859

[3] *Wikipedia*. Licenced under the Creative Commons licence.

[4] 'Modern Physics', Serway, R A, Moyer A, *Thomson*, 1996, ISBN 0030196825

[5] 'Chemical Kinetics', 3rd Edition, Laidler K J, *Benjamin-Cummings*, 1997, ISBN 0060438622

[6] http://www.bioanalytical.com/products/ec/digisim/

[7] www.elchsoft.com

[8] Rudolph M, *J Electroanal. Chemistry*, 1991, **314**, 13-22

[9] Rudolph M, *J Electroanal. Chemistry*, 1994, **375**, 89-98

[10] 'An Introduction to Electrochemical Impedance Spectroscopy,' Cogger, M D, Evans, M J, *Solartron Technote 06, http://www.solartronanalytical.com/technicalsupport/technicalnotes/technote06.htm*

Chapter 3: The effects of hydrogen bonding environments on thiol groups.

Mixtures of dimethylsulfoxide (DMSO) are widely used by molecular biologists in the study of intracellular interactions. This chapter investigates the effect of the hydrogen-bonding environment of DMSO:water mixtures on biological molecules, focusing on the S-H (thiol) groups of cysteine residues and the small-molecule protein analogue BMC. Confocal Raman spectroscopy is used to measure the effect of differing DMSO:water mixtures on the wavenumber and intensity of the S-H vibrational band.

3.1. Introduction

3.1.1. Thiol groups in biology

A thiol functional group, simply an R–SH group, is extremely important in molecular biology. When two thiols are oxidised under mild conditions, a disulphide bond (RS-SR) is formed[1]. A simple reduction will likewise convert a disulphide to two thiols. Cysteine, (Cys), is the only amino acid that contains a thiol group. When two cysteine molecules undergo mild oxidation, a disulphide, cystine, consisting of two cysteines connected by a disulphide bond, is formed.

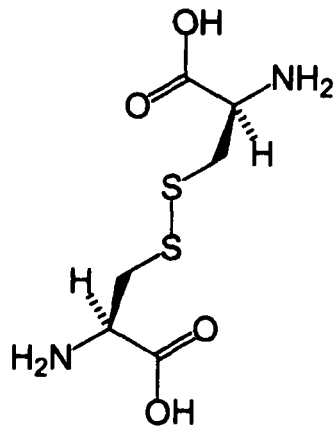

Figure 3.1.1.1: Molecular diagram of cysteine, showing the S-S disulpide bridge between the two cysteine residues.

Two cysteine residues in a protein can therefore be connected by a disulphide bridge. Importantly, disulphide bridges are the only way of connecting nonadjacent amino acid residues covalently. Disulphide bridge in proteins play two major roles. They either stabilise the protein in a particular folded state by holding cysteine residues close together, or are formed transiently as part of a regulatory or catalytic cycle.[2]

The formation of cys-cys disulphide bonds is the rate-determining step in the formation of many proteins. A newly synthesised protein firstly needs to have its thiol groups oxidised to disulphide bonds. Reduced proteins in the unfolded state will oxidise in a non-specific fashion, creating disulphide bonds between cysteine residues that lead to an incorrectly folded protein structure. The disulphide bonds thus formed must then be 'unscrambled', isomerised into the correct structure by enzyme catalysis.

A sufficiently oxidising environment is required for the oxidation of protein thiols to disulphide bonds to occur. These environments are found in the lumen of the endoplasmic reticulum (ER) of cells, a highly efficient protein folding compartment, (so efficient that some cell types have a daily folded protein output greater then their own mass), where oxidative native folding can occur[3]. The ER's high output is accomplished by a highly optimised environment for protein folding. The lumen contains a rich variety of molecular chaperones and isomerases, as well as a powerful quality control system that degrades proteins folded into non-native states.

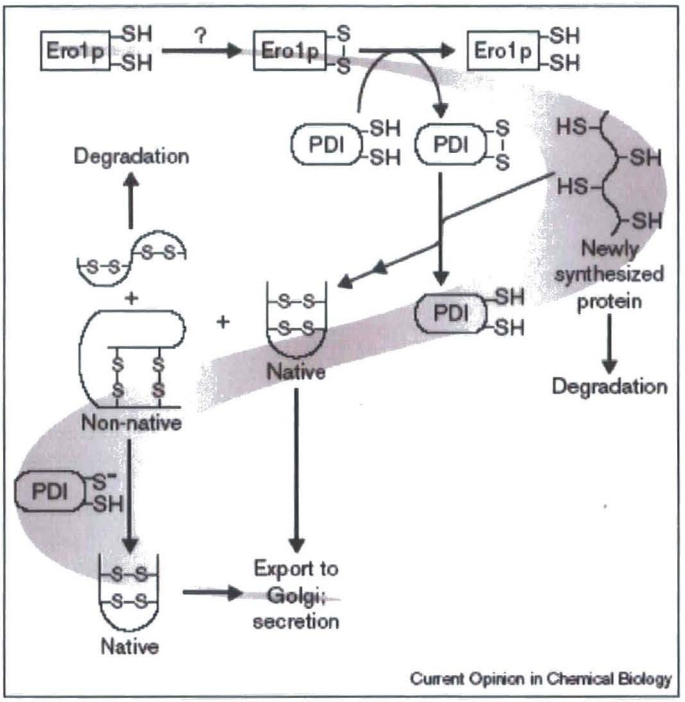

*Figure 1.1.1.1 : Primary pathway of native disulphide bond formation in the ER. (Curr. Op. Chem. Biol, 2000, **4**, 533)*

The ER is distinctive from other cellular protein folding structures in its ability to produce folded proteins containing native disulphide bonds. Such proteins are found in abundance in secretory pathways originating from the endoplasmic reticulum, but are mostly absent in cytosolic proteins[4]. Disulphide bond formation requires a mild oxidative environment – a strongly oxidising environment results in spontaneous disulphide bond formation, leading to the formation of non-natively folded proteins, whereas a reducing environment discourages the formation of disulphides thermodynamically. The endoplasmic reticulum is surrounded by cytosol, which is a highly reducing environment. The endoplasmic reticulum must therefore be maintained at an oxidising potential by an oxidoreductase mechanism.

3.1.2. Enzymatic protein folding

Oxidative folding is arbitrated by two proteins, Protein Disulphide Isomerase (PDI), a member of the thioredoxin family, and Endoplasmic Reticulum Oxidoreductin 1 protein (Ero1p)[5], a glycoprotein. PDI catalyses the native formation of disulphide bonds in target proteins, and Ero1p oxidises PDI after it has been reduced.

PDI is a 57kDa resident of the ER, containing five separate domains. The three-dimensional structure of the entire enzyme has not been determined. Four domains are homologous, the a, a', b and b' domains. PDI contains two catalytic sites, located at the end of the a and a' sites. Each catalytic domain ends with a Cys-Gly-His-Cys sequence. (commonly found in oxidoreductase proteins, this motif is known as CXXC, due to the recurring bi-cysteine pattern, separated by two other residues). This sequence places the two cysteine thiol groups in close proximity, allowing ready oxidation/reduction to occur. The b and b' domains have been found to have a role in binding of the substrate to the active site[6]. The c domain is acidic, and is not required for catalytic activity. It is thought that the domain is used to signal retention of the PDI enzyme to the ER mediators.

Ero1p is a recently-discovered endoplasmic reticulum resident with a 65 kDa weight. Its presence has been found to be essential for cell viability, and its absence or loss of function in the endoplasmic reticulum results in a buildup of unfolded and reduced proteins in the ER. Overproduction of unfolded proteins leads to a high rate of Ero1p formation. This indicates that Ero1p has a significant function in the ER, and in the ability of PDI to oxidise and isomerise new proteins. Ero1p is dependent on the flavin adenine dinucleotide (FAD) cofactor, and has been found to include a CXXXXC motif, which is involved in binding to PDI.

The ability of PDI to function as an isomerase and an oxidoreductase is governed by the redox potential of its active-site disulfide bond (E°) and by the acid dissociation constant of its nucleophilic active-site thiol (Ka). The optimal E° for isomerase activity is reported as -0.18 V and a pKa close to the pH of the biological

environment i.e. close to 7.0 . The pKa value of the N-terminal cysteine of the CXXC motif in PDI has been reported as 6.7, an unusually low figure given that the pKa of a typical cysteine residue is 8.7.

3.1.3. BMC: A small-molecule analogue of PDI

(±)trans-1,2-bis(2-mercapto-acetamido)cyclohexane, commonly abbreviated to BMC, is an attempt to synthesise a small-molecule catalyst of oxidative protein folding based on what is known of the properties of PDI . BMC, although hundreds of times smaller then PDI, mimics PDI's active site pKa and E0 values as well as the active thiol groups.

BMC is structured around a cyclohexane ring, with two identical chains (mercaptoacetamido groups) leading off. These chains end in thiol groups, close enough together to oxidise to a disulphide bond. Inductive effects from the electronegative carbonyl and nitrogen lower the thiol pKa values to a range closer to PDI's, ensuring fairly ready oxidation to a disulphide bond at neutral pH. (100-fold more so than a standard thiol)

In vitro, BMC has been found to unscramble proteins to their native configuration, increasing both the rate of activation and final yields of proteins containing multiple disulphide bonds. A monothiol equivalent of BMC was also tested, which resulted in slower activation and less protein yield. This indicates the importance of the disulphide bond as an electron acceptor in folding catalysis, BMC is marketed commercially as Vectrase-P, an in vitro protein-folding catalyst which increases active yields by 2-3 times.

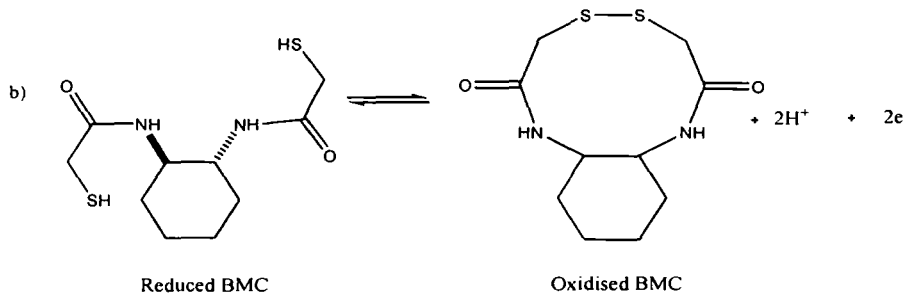

Figure 3.1.3.1. Structures of the reduced and oxidised forms of BMC, a small-molecule analog to protein disulphide isomerise.

3.1.4. Dimethyl Sulfoxide

Dimethyl sulfoxide (DMSO), a polar aprotic clear colourless liquid at room temperature, is a frequently used solvent for chemical reactions. DMSO has excellent solvating properties and is used in reactions involving salts such as the halide-exchange Finkelstein reaction[7]. DMSO is weakly acidic, and as such can solvate relatively strong bases. The methyl groups on DMSO are slightly acidic, possessing a pKa of about 35.

DMSO has an extremely high boiling point of 189^{0}C, which makes it difficult to evaporate off when required. DMSO:water mixtures are often used to precipitate organic solvents. DMSO and water are completely miscible, interacting via hydrogen bonding between the basic oxygen of DMSO and the acidic protons of water[8]. Molecular dynamics simulations of DMSO:water mixtures reveal several hydrogen-bonded aggregate patterns. 1:2 2:1 and 1:3 DMSO:water aggregations are common, with the 1:2 DMSO:water linear structure being the most stable[9]. The hydrogen bonds between DMSO and water have been found to be very stable, more so then the bonds between two water molecules[10]. As the concentration of DMSO increases in a mixture, the physical characteristics of the mixture change. The pK_w of water in an 8:1 DMSO:water mixture has been reported as 18.38[11]. The comparative physico-chemical properties of water and DMSO based on Gutmann and Gerger's

acceptor (AN) and donor number (DN) values are shown in Table 3.1.4.1. The solvent basicity increases with increasing DN and solvent acidity increases with increasing AN. Both water and DMSO have high permittivities (ε_r>30).

solvent	H^+ donor number (DN)	H^+ acceptor number (AN)	pK_{SH}	ε_r
water	33	54.8	14.0[*2]	78.4[*3]
DMSO	29.8	19.3	33.3[*4]	46.5[*4]

Table 3.1.4.1. Physical characteristics of DMSO and water.

DMSO is used extensively in biology. It is used in the polymerase chain reaction (PCR) procedure for rapidly replicating DNA strands, acting as an inhibitor to the self-complementarity reactions that otherwise occur. It is also used in cellular cyroprotection mechanisms, helping to prevent cellular death when freezing samples by preventing the formation of ice crystals through strong DMSO:water hydrogen bond formation. This process, freezing a solid without crystal formation, is known as vitrification.

DMSO:water mixtures are frequently used in a range of biological and pharmaceutical techniques. Mixtures are commonly used in protein analysis, as DMSO has the ability to solvate polar and non-polar compounds. DMSO is therefore often used as the preferred solvent to prepare standard stock solutions of biological molecules. DMSO has also been found to have a range of possible pharmaceutical uses, including analgesic and anti-inflammatory applications[12].

3.1.5. Objectives

Mixtures of DMSO and water are commonly used when working with peptides and proteins. Proteins are folded in their native configuration by the formation of S-S bonds between thiol groups attached to cysteine residues in the protein. This process is catalysed by the enzyme protein disulphide isomerise, (PDI), of which several small-molecule analogues have been constructed. The most successful analogue is BMC, which is administered *in vivo* in a DMSO:water mixture.

DMSO:water mixtures have been noticed to have significant effects on the pKa of thiol groups, due to the differing hydrogen-bonding environment present in the mixture. This will affect the ionisation potential of cysteine and BMC thiol groups, and thus the rates and outcomes of the isomerisation reaction. The thiol group may act either as a hydrogen donor (S-H...O) or as an acceptor (H.....S-H).

This investigation uses Raman spectroscopy to examine the effect of different concentrations of DMSO in aqueous solutions on the strength and disassociation of the S-H bond. The Raman S-H, thiol band is a very sensitive probe of local S-H interactions. As the strength of the hydrogen bonding increases, the vibrational energy of the S-H bond decreases leading to a lowering in the band wavenumber. The Raman S-H stretching vibration, σ_{SH}, occurs at 2525-2560 cm^{-1}, 2560-2575 cm^{-1} and 2575-2580 cm^{-1} corresponding to strong, moderate or weak S-H hydrogen bonds, respectively. Hydrogen bond acceptance by S, on the other hand, is apparent as a slight elevation of the order of <4 cm^{-1} in the σ_{SH}.[13]

Close observation of the S-H stretching vibration will therefore infer the strength of the thiol bond. Comparison of cysteine and BMC S-H bands from different DMSO:water ratios should therefore provide insights into how the hydrogen-bonding environments of different mixtures affect the strength and characteristics of the S-H bond in biological molecules.

3.2. Experimental Details

3.2.1. Solution preparation

The chemicals used were cysteine, L-CSH (≥99.5%, Biochemica Ultra (Sigma)); cystine L-CSSC (≥98.5%, from non-animal source, cell culture tested (Sigma)); DMSO (puriss. p.a., ≥99.5% (GC) (Fluka)) and BMC, which was synthesized in- house according to previously published procedures[14].

Solutions of cysteine at 10mMdm^{-3} were prepared in pure aqueous medium, as well as mixtures of DMSO and water at 2%, 10%, 30%, 50% 70% and 90% DMSO composition with respect to weight. BMC was used both in a solid crystal form as well as dissolved in a 30% DMSO:water w/w solution. Solutions were acidified using stock concentrated H_2SO_4. (98%) Dilute 1M NaOH was used to raise the solution pH. A Jencons-PLS 3345 pH meter was used to monitor the solution pH.

3.2.2. Raman spectroscopy measurements

Raman measurements with cysteine and oxidised BMC were recorded with a Jobin Yvon LabRam 300 spectrometer using a HeNe 633nm laser. A CaF_2 multipass cell-holder, which allows measurement of Raman spectra in the solution phase, was used for measurements in aqueous and DMSO/water mixtures. Measurements were performed with a confocal hole diameter of 300 μm and a spectral slit width of 150 μm.

Frequency calibrations were performed using a block of pure silicon at 520cm^{-1}. The scan integration times used were 5s for the aqueous solutions and 60s for DMSO/H_2O solutions. Solutions of 10 mmol dm^{-3} concentrations were used for cysteine and BMC. Acidified solutions were pH titrated in situ and the pH measured with calibrated combination glass electrodes. LabSpec software, version 4.14, was used to collect and analyse the data.

3.3. Results and Discussion

3.3.1 Raman spectra of cysteine

Raman spectra were taken of 10mM solutions of cysteine in DMSO and water mixtures. Spectra were taken for pure aqueous solutions, as well as for 2%, 10%, 30%, 50% and 70% DMSO w/w mixtures.

Cysteine in aqueous solution shows a clear σ_{SH} stretch at 2576 cm^{-1}. This is in line with literature values for the σ_{SH} stretch[13], which place it at 2580 cm^{-1}.

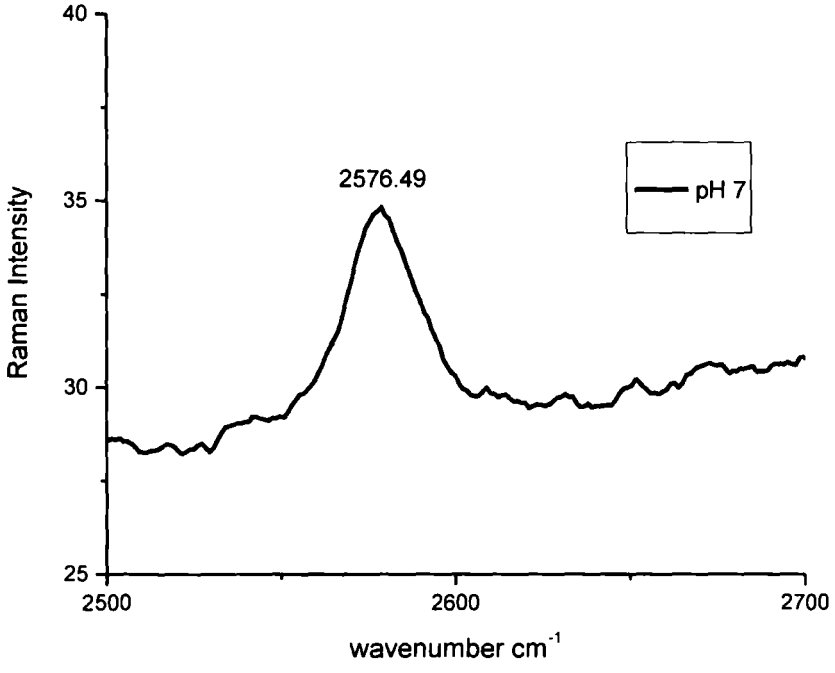

Figure 3.3.1.1. Raman spectrum of cysteine, focused on the –SH bond stretching vibration region.

To ensure that the –SH band was the peak being observed, the aqueous cysteine solution was acidified down to pH 3 using concentrated H_2SO_4, added dropwise until the required pH was reached. Dilute 1M NaOH was used to raise the solution pH to

9. The aqueous ionisation constant, the pKa, of the thiol group is approximately 8.3. The S-H bond should therefore be almost completely associated at pH 3, partially associated at pH 7 and almost completely disassociated at pH 9.

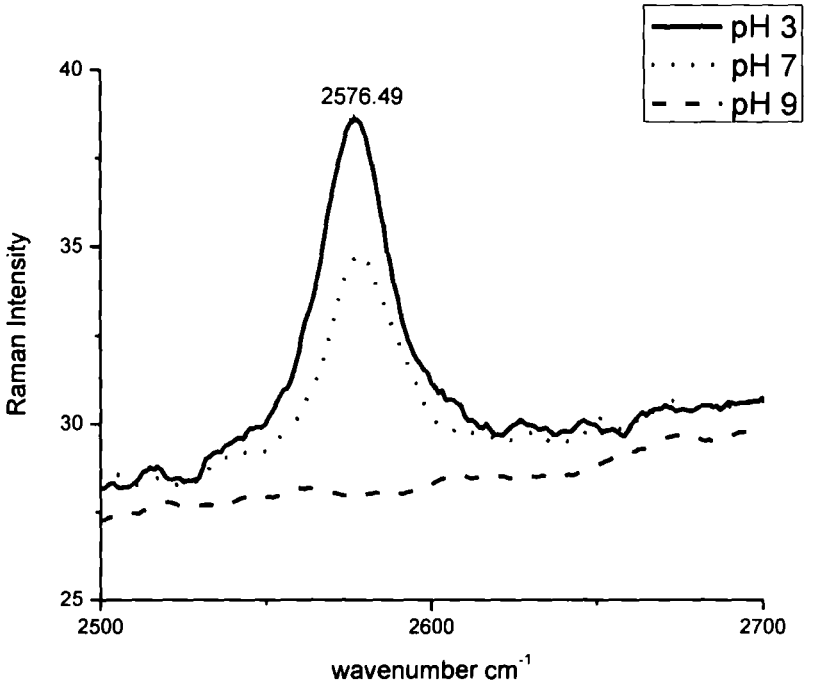

Figure 3.3.1.2. Raman spectra of cysteine, taken at three differing pH levels.

The peak follows the expected trend, diminishing in intensity as the pH increases. At pH 7, the peak is roughly half the intensity of the pH 3 peak, and at pH 9 the peak disappears completely. This corresponds to measurements made potentiometrically to determine the pKa[16], which predict almost complete dissociation at this point.

Spectra were then taken of 10mM cysteine solutions in various DMSO:water mixtures.

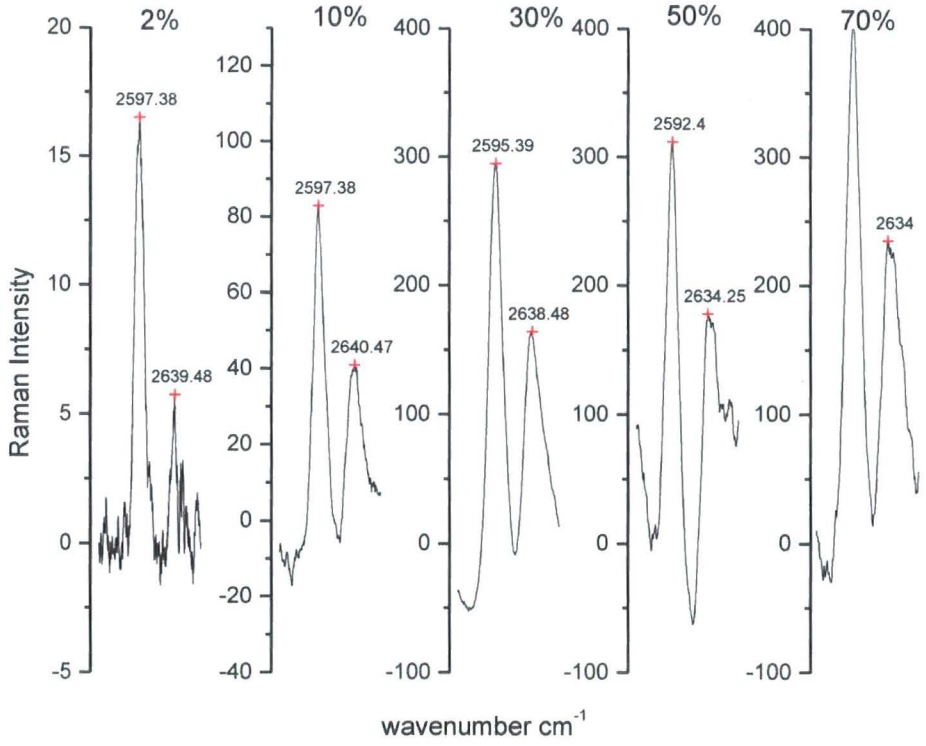

Figure 3.3.1.3. Raman spectra of cysteine in varying DMSO/water compositions.

A significant effect is shown even at the 2% DMSO w/w mixture, with a shift in the σ_{SH} from the value of 2576cm^{-1} seen in a the purely aqueous solution to a value of 2597.38 cm^{-1} ±0.5. This value stays constant at a 10% w/w mixture, dropping slightly to 2595±0.5 cm^{-1} at 30% w/w mixture and 2592 ±0.5 cm^{-1} at 50% and 70% w/w mixtures.

These results suggest that even a small quantity of DMSO changes the hydrogen bonding environment significantly. As H_2O and DMSO form aggregates of well-defined hydrogen bonding motifs which compete against the SH.....OH hydrogen bonds, considerably inhibiting the bonding and leading to the strengthening of the –SH bond. This shift is not noticeable in non-polar solvents such as

tetrachloromethane and dimethyl ketone, which exhibit σ_{SH} values of 2582 and 2577 cm^{-1} respectively.

DMSO-water mixtures appear to exhibit an extra peak compared to a pure aqueous mixture. This peak exists at 2635±3 cm^{-1}, and would appear to represent the –OH bond stretch in the $(CH_3)_2S{=}O....OH$ species, as suggested by computational spectral analysis of the species using the Know-it-All software package published by BioRAD Ltd.

The intensities of the σ_{SH} peaks were plotted on a scatter graph to investigate the relationship between the percentage of DMSO in the mixture and the intensity of the peak. Increased band intensities and larger band widths may imply the formation of S-H....S associative bonds,[13] in which the thiol group acts as both donor and acceptor. These have been seen to occur[13] in non-polar solvents such as CCl_4, increasing in intensity with higher concentrations of solute. They have also been observed in pure thiol compounds.

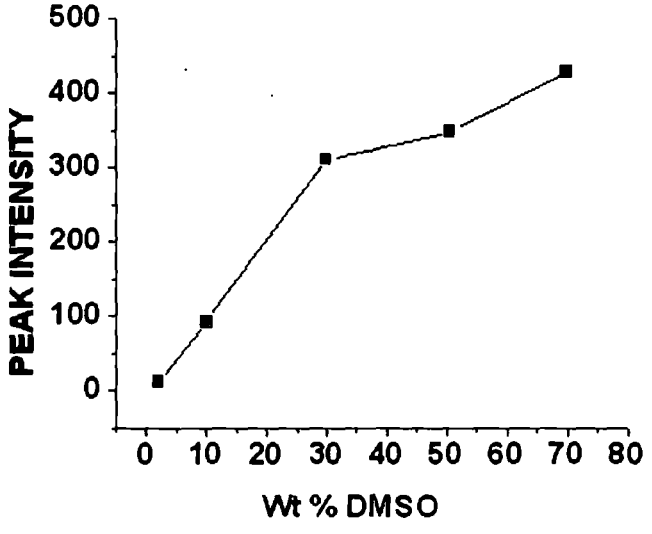

Figure 3.3.1.4. σ_{SH} peak intensity at various concentrations of cysteine in 10 % w/w DMSO/water.

This graph shows a roughly linear relation between the intensity and the percentage w/w of DMSO present, up to approximately 30%. There is a change in the slope at 30%, at the point the σ_{SH} band shifts slightly from 2597 to 2595 cm^{-1}. DMSO-water mixtures hit the point of maximum non-ideal behaviour at between 30-40% DMSO w/w, the point at which the 1:2 DMSO:water hydrogen-bonded aggregates become most common. Physical properties are affected by hydrogen-bonded aggregates, including freezing point, viscosity and dielectric constants[15]. The intensity increases quickly up to the point of non-ideal behaviour due to the rapid strengthening of the S-H bond because of competitive hydrogen-bond formation. Beyond this point, the intensity increases more slowly, as S-H...S associative bonds form. These bonds form both between different –SH groups and between –SH groups and the lone pairs on the accessible central sulphurs of DMSO.

Solutions of 10mM cysteine in a 90% w/w DMSO solution were prepared and the pH was varied between 3 and 12, in order to investigate the effect of a concentrated DMSO environment on the pKa of the thiol group.

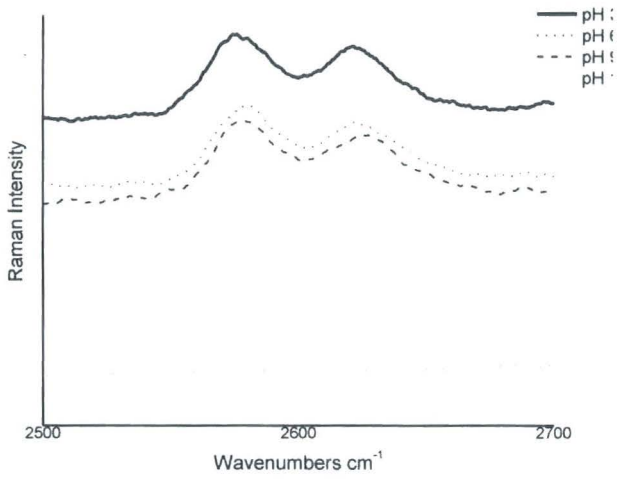

Figure 3.3.1.5: Raman spectra of Cysteine in 90% w/w DMSO/water compositions at varying pH.

The wide dual peaks associated with the S-H bond stretch are present at pH 9, unlike in a fully aqueous solution, and do not fully disappear until pH 12. This suggests that the thiol group is more basic in DMSO due to the increased bond strength. Potentiometric titrations[16] confirm this, showing the pKa of the cysteine thiol group to be 13.43 in a 90% w/w DMSO solution compared to 8.38 in a fully aqueous solution. This is a considerable difference of 5 units.

3.3.2 Raman Spectra of BMC

Crystals of BMC were synthesised and purified[14], before Raman spectra were taken. A spectrum was first taken in the solid-state.

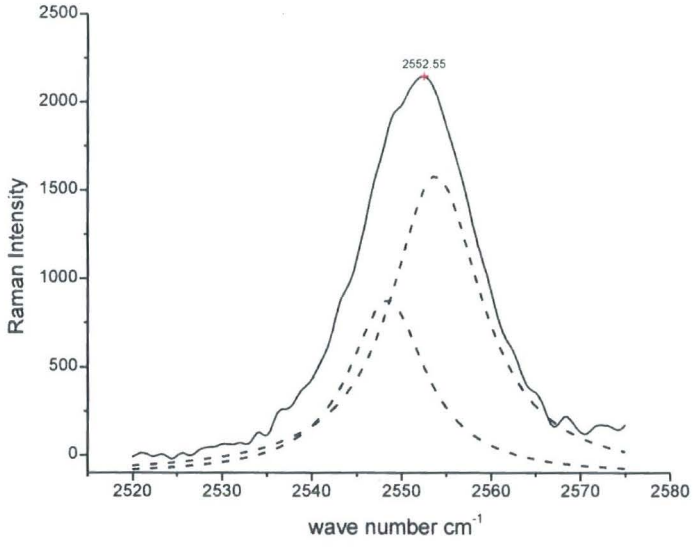

Figure 3.3.2.1. Raman Spectrum of BMC crystal showing the observed Raman S-H band (solid line) and the fitted profile representing the optimum least squares fit of the data to two Lorentz curves including two S-H stretching bands.

Solid BMC crystals show one large wide S-H bond peak. This corresponds to both of the thiol groups of BMC. Pure BMC would be expected to show self-associative hydrogen bonds between the thiol groups, forming hydrogen-bonded sulfhydryl multimers. This would be indicated by a widening of the peak, as seen above.

An optimum least-squares fitting of the single wide BMC peak using Originlab to two Lorentz curves shows two σ_{SH} stretches. The larger Lorentz peak at 2555 cm^{-1} refers to the S-H stretch, whereas the more minor shifted peak at 2549 cm^{-1} relates to the multimer states. This peak is shifted due to the weakening of the S-H bond, caused by greater hydrogen bonding.

When dissolved in a 30% DMSO w/w solution at pH 7, BMC produces a complex peak in the σ_{SH} stretching region.

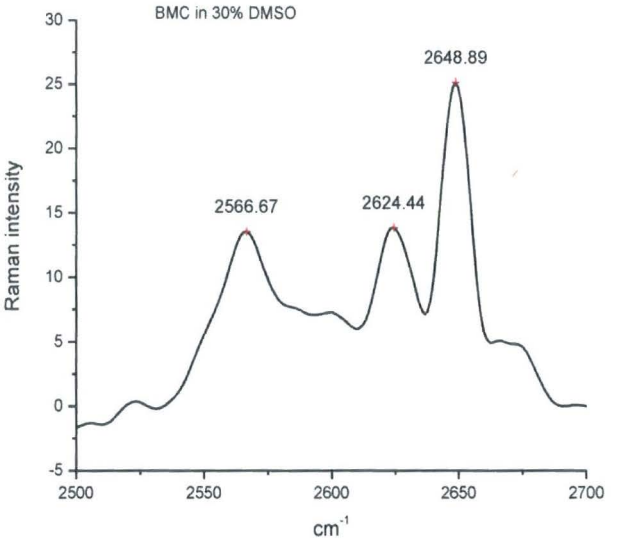

Figure 3.3.2.2. Raman spectrum of BMC IN 30% w/w DMSO:water mixture in the S-H stretch region.

Two separate peaks of equal height are seen in the region, with a third peak of greater intensity beyond them. The two peaks relate to the two thiol groups of BMC, which can be seen as one peak in the solid crystalline form (Figure 3.2.1). The peaks are positioned at higher wave numbers then the peaks seen in the solid form, showing a loss of hydrogen bonding and a strengthening of the S-H bonds. A spectrum was also taken of the S-S bond stretch region at ~500 cm^{-1}.

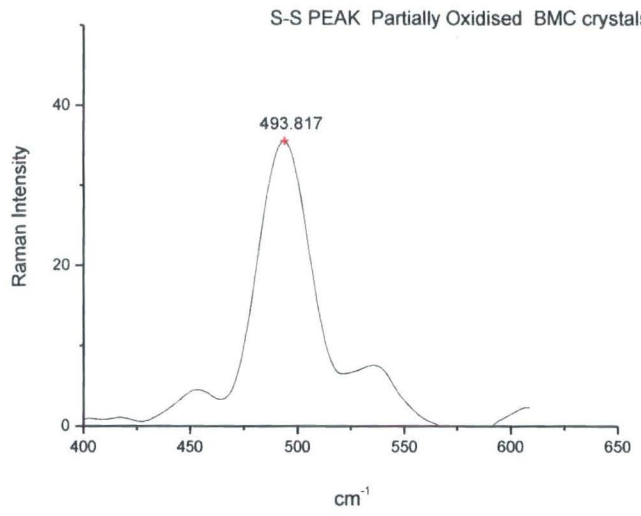

Figure 3.3.2.3. σ_{SS} stretch of a partially oxidised BMC sample.

This peak shows the presence of S-S bonds, and thus the presence of the oxidised form of BMC. Redox potential measurements were carried out[16] on BMC in differing DMSO:water mixtures. A substantial change in potential was found, which was greatest at a 30% w/w DMSO solution.

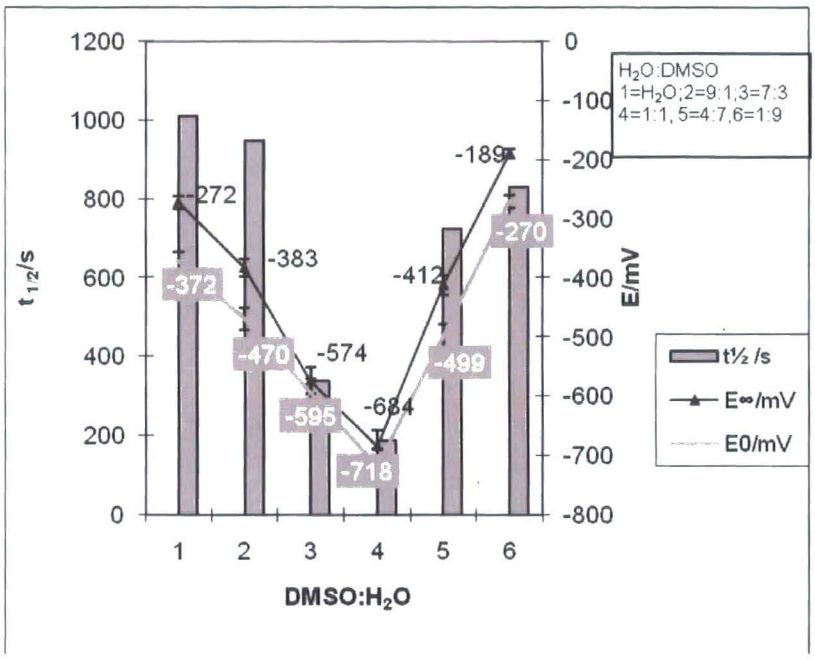

Figure 3.3.2.4. Half life times and changes in redox potentials of a freshly prepared BMC solution in various DMSO/water compositions.

BMC's initial redox potential was -189mV in a purely aqueous solution, dropping to -684mV in a 30% w/w DMSO solution. The redox potential then rose again, to a maximum of -189 mV in a 90% w/w DMSO solution. The half-life of reduced BMC reduced correspondingly significantly, from 1010s in 10% DMSO:water mixtures to 190s in 30% mixtures. The half-life time again increases by a large amount when a 90% mixture is used, up to 725s. These massive change in redox potential and half-life show that BMC will have significantly different physical properties when solvated in a DMSO:water mixture then when dissolved in a purely aqueous solution.

These results indicate that studies of BMC in a DMSO solution as an analogue of protein disulphide isomerase will need to take into account the differing hydrogen bonding environment in the solution from that found inside a living cell.

3.4 Conclusions

Investigations with Raman spectroscopy showed that the presence of DMSO as a solvent has profound effects on the properties of the thiol group. In pure aqueous conditions, the thiol group of cysteine is seen as a sharp peak at 2576.6 cm^{-1}. With even tiny quantities (2%) of DMSO added, this peak shifts markedly to 2597 cm^{-1}, indicating that the hydrogen-bonding environment in a DMSO:water mixture has significant effects on the strength of the S-H bond and its ability to form hydrogen bonds with solvent molecules. Dramatic increases in intensity are seen with increasing weight of DMSO, suggesting the formation of S-H....S bonds between adjoining thiol groups and between thiol groups and DMSO. The basicity of the thiol group also increased significantly, from complete disassociation at pH 9 in an aqueous solution to complete disassociation at pH 12 in a 90% DMSO w/w solution, an increase in the pKa of 5 units.

BMC also shows some considerable differences in a DMSO solution compared to its pure crystalline form. At a 30% DMSO w/w solution, BMC's redox potential drops by 495mV compared to a fully aqueous solution. This has a considerable effect on the strength and association of the thiol groups in BMC, and thus on the Raman spectrum (figure 3.3.2.3).

These results have interesting implications for the use of DMSO as a solvent when studying reactions in the endoplasmic reticulum. Although intracellular environments are aqueous, they are densely packed with macromolecules. These results suggest that changing the polarity or hydrophobicity of the local redox environment could have a profound effect on thiol based drugs and probes such as BMC.

References

[1] 'Organic Chemistry', 3rd Edition, P, Bruice, Prentice Hall, (2001)

[2] 'Roles of Thiol-Redox Pathways in Bacteria', Ritz D, Beckwith J, *Annu Rev Microbiol.* 2001;**55**:21-48

[3] Pollard M, Travers K J, Weissman J S, *Mol. Cell,* 1998, **1**, 171-182

[4] Braakman, I, Helenius, J and Helenius, A. *EMBO J,* (1992).**11,** 1717–1722.

[5] Woycechowsky, K J, Raines, R T. *Curr. Op. Chem. Biol*, 2000, **4**, 533-539

[6] 'Recognition of protein substrates by protein-disulphide isomerase', Cheung P Y, Churchich J E, *J. Biol Chem,* 1999, **274**, 32757-32761

[7] Streitwieser, A. *Chem. Rev.* 1956, **56**, 571-582

[8] R. L. Mancers, M. Chalaris, K. Refson, J. Samios, *Phys. Chem. Chem. Phys.*, 2004, **6**, 94-102.

[9]Borin, I. A. and Skaf, M. S., *J. Phys. Chem.*, 1999, **110**, 6412

[10] Luzar A., *J. Chem. Phys.*, 1989, **91**, 3603.

[11] Baughman E. H. and Kreevoy M. M., *J. Phys. Chem.*, 1974, **78**, 421.

[12] 'Lockie, L.M., Norcross, B', *Ann NY Acad Sci* 1967, **141**, 599-602.

[13] Li H, Thomas, Jr G. J.., *J. Am. Chem. Soc.*, 1991, **113**, 2.,456-463

[14] Woycechowsky K. J., Wittrup,K. D. and Raines, R. T., *Chem. & Biol.*, 1999, **6**, 871.

[15] Luzar, A. Chandler D., *J. Phys. Chem.*, 1993, 98, 10, 8160-8173

[16] Kruusma. J, Rhodes. A, Bhatia. R, Kataky. R, *J. Sol. Chem,* 2007, **36**, 517-529

Chapter 4: SKN and Electrochemical Investigation of Nanostructured films of Phthalocyanine Derivatives

Appropriately designed phthalocyanine derivatives have the ability to form size and charge selective nanoporous assemblies on substrates such as gold and silver. Several such derivates were investigates using Scanning Kelvin Nanoprobe Microscopy, as well as Atomic Force Microscopy and cyclic voltammetry to show that phthalocyanine derivatives which have been designed to avoid traditional crystalline aggregation can create thin films on electrodes that are selective to size and charge.

4.1. Introduction

4.1.1 Phthalocyanine

A phthalocyanine is defined as an 18 π-electron symmetrical macrocyclic ring compound having an alternating nitrogen-carbon ring structure[1]. The structure of phthalocyanine is closely related to the porphyrin. It is able to coordinate to metal cations contained in the central ring cavity by forming coordination bonds using the four nitrogen atoms evenly spaced around the ring structure.

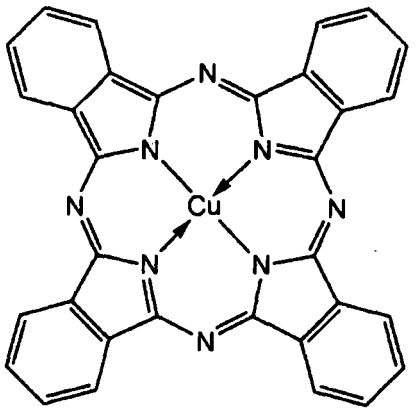

Figure 4.1.1.1: Phthalocyanine Blue BN, a copper phthalocyanine used as a paper dye. The copper cation is held in the middle by ligand bonds from the four isoindole nitrogen atoms.

Phthalocyanine was discovered in 1907 by accident as the byproduct of an organic reaction. The blue substance produced was uncoordinated, metal-free phthalocyanine. 1927, copper phthalocyanine and several variants were again accidentally synthesised by researchers in Switzerland. Phthalocyanine's true usage of a dye came when the same experiment was repeated by Scottish Dyes, which later became ICI. Phthalocyanine's main industrial use is as a dye, but the possibilities of phthalocyanine are far greater than this, as evidenced by the vast wealth of scientific literature pertaining to phthalocyanine compounds. On average, three scientific articles involving phthalocyanine are published every day[2], and over 5000 phthalocyanine compounds have been synthesised. The reasons for phthalocyanines popularity lie in its optical and electronic properties, which are predictable, reducible and stable. This is due in large part to the extent of the intermolecular π-π stacking interactions between the planar aromatic faces of the phthalocyanine macrocycles. These strong interactions often lead to fluorescence quenching and a blue-shifted Q-band due to excitation coupling[3], making phthalocyanine an attractive dye, as well as allowing phthalocyanine to be used for many highly-technological uses, including photoconducting material in laser printers and the adsorbing layer in recordable optical media such as DVDs[4]. Phthalocyanines have many uses in physical and analytical chemistry, including chemical sensors, modified electrodes[5] and fuel cells[6].

4.1.2 Phthalocyanine thin-films

Phthalocyanine compounds have a natural tendency to organise into crystalline thin-films upon surfaces. Thin-films of phthalocyanine, with various functionalisations and central metal atoms, have been heavily studied. The formation of thin-films of phthalocyanine with one or two trichlorosilyl alkylchains on glass and silicon has been reported by Cook.[7] More recently, thiol and disulphide-functionalised phthalocyanines were found to self-assemble on gold surfaces[8]. Infrared reflection-absorption spectroscopy and evanescent wave-excited fluorescence emissions suggested that the orientation of the phthalocyanine

macrocycle was dependent on the length of the spacer between the macrocycle and the gold substrate.

Self-assembled monolayers of thio-tethered and axially-ligated phthalocyanine compounds have been reported by Li[9]. The molecular formation of a thin-film of 2,9,16,23-tetraaminometal phthalocyanines, with the central metal being cobalt, copper or iron was reported by Sampath[10]. Cyclic voltammetry, impedance and FT-Raman spectroscopy showed that the films exhibited a blocking behaviour when deposited on a gold electrode. FT-Raman studies showed characteristic bands around 236 cm^{-1} revealing the interaction between the metal substrate and the nitrogen of the $-NH_2$ group on the phthalocyanine molecules. The behaviour of the filmed electrodes in the presence of the $Fe(CN)_6^{3-/4-}$ redox couple suggested a percentage coverage of approximately 85% in the case of the copper and iron phthalocyanines, and almost complete coverage in the case of the cobalt-centred phthalocyanine.

4.1.3 Axially-substituted phthalocyanine derivatives

Phthalocyanine derivatives that have been axially-ligated have the ability to form films with a more amorphous character, due to the axial substituents interfering with the intermolecular π-π stacking interactions between the phthalocyanine rings. These help to prevent aggregation, and therefore form well-ordered nanoporous films. Phthalocyanines which are unable to aggregate properly due to the presence of structural steric hindrance give higher photoluminescence quantum yields than normal, as well as sharper UV-vis absorption and emission peaks[11], making them of interest for fluorescence studies.

These phthalocyanine derivatives are also of interest to electro- and analytical chemists. As seen in section 4.1.2, axially-substituted phthalocyanine thin-films exhibit blocking behaviour at electrode surfaces. The blocking percentage depended both on the central metallic ion of the phthalocyanine as well as the electrochemical probe molecule being used. Judiciously-synthesised phthalocyanine

derivatives can therefore serve as size- and charge- selective thin-films for electrode surfaces, with potential applications in diagnostic and medical technology as well as in process engineering and environmental contaminant detection.

4.1.4 Objectives

This chapter details an electroanalytical study of a novel axially-substituted phthalocyanine derivative, silicon phthalocyanine bis(3,5-diphenylbenzoate), using Scanning Kelvin Nanoprobe (SKN) scans, Atomic Force Microscopy (AFM) scans and confocal Raman spectroscopy. Electrochemical studies using cyclic voltammetry were also carried out with a further two derivatives thought to form more crystalline depositions, silicon phthalocyanine bis-(3-thienyl) acetate and silicon phthalocyanine bis(4-tertbutyl)benzoate. Simple computational molecular modelling of the phthalocyanines was also carried out.

The three phthalocyanine derivatives under investigation were;

1. silicon phthalocyanine bis(4-tert-butylbenzoate). (Figure 4.1.4.1a)
2. silicon phthalocyanine bis-(3-thienyl)acetate. (Figure 4.1.4.1b)
3. silicon phthalocyanine bis(3,5-diphenyl)benzoate. (Figure 4.1.4.1c)

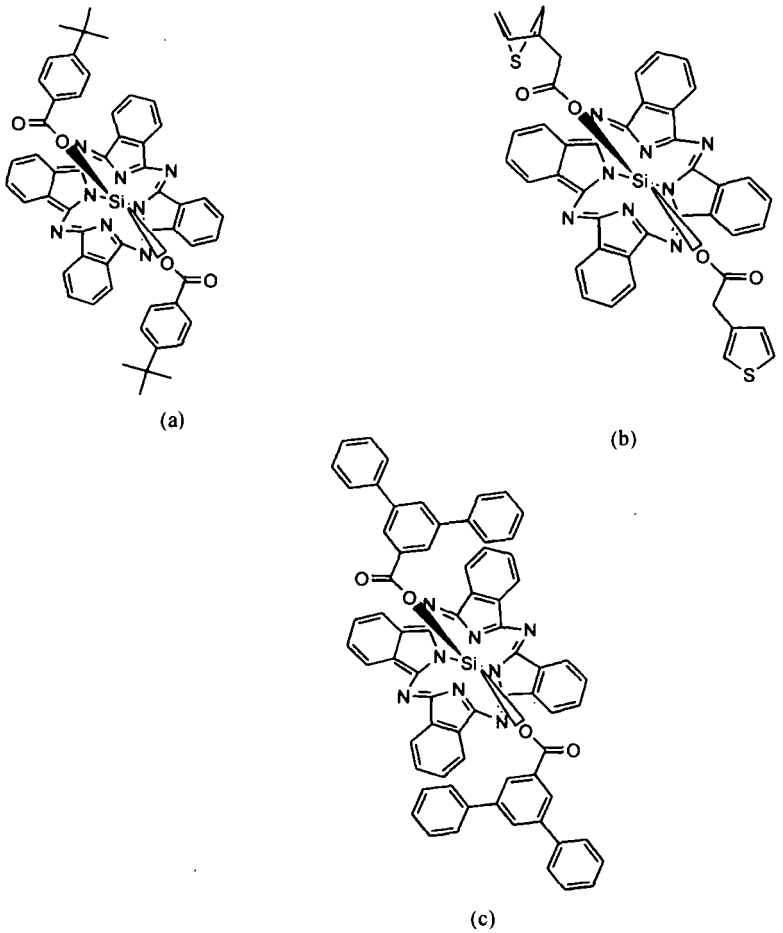

Figure 4.1.4.1: Molecular structures of phthalocyanine derivatives.

The derivatives were synthesised by Carl Barker *et al* of Durham University[12], utilising a nucleophilic displacement of chloride substituents from $Si(Pc)Cl_2$. Compound **1** formed a green solid at room temperature, while compounds **2** and **3** formed bright blue solids, all with melting points over 400°C. The compounds were insoluble in aqueous solutions, but proved to be readily dissolvable in chloroform and dichloromethane.

4.1.5 Analytical Methods

4.1.5.1 Molecular modelling

Simple semi-empirical molecular modelling was carried out on the phthalocyanine derivatives using the Hyperchem 6 molecular modelling package. This modelling, although simplistic and rough compared to a dedicated mainframe-based package, allows the graphical representation and manipulation of the arrayed molecules and thus is greatly useful for visualisation of the thin-film structure.

4.1.5.2 Scanning Kelvin Nanoprobe Microscopy

SKN microscopy was used to investigate the phthalocyanine thin-film formation on gold. Although a new and not-widely used analytical method, SKN shows promise as a powerful tool for probing of organic and biological films and monolayers, having been employed before in the study of deposited materials[13] and thus was employed here in conjunction with other, better known methods.

4.1.5.3 Atomic Force Microscopy

Atomic force microscopy is one of the oldest and best known forms of probe microscopy, and is used regularly to image the topographical layout of many kinds of material. AFM has been used here to investigate the magnitude of crystalline aggregation present for each phthalocyanine derivative by using both straight topographical (tapping mode) and phase mapping on thin-films of the three derivatives.

4.1.5.4 Confocal Raman Microscopy

Simple Raman spectra have been taken of bare and filmed substrates to confirm correct deposition and to characterise the material. Raman spectra can provide information about the crystalline structure of a material by the width and shift of vibrational peaks, and this information can be used in combination with other data to provide an estimate of the deposited structure.

4.1.5.5 Cyclic Voltammetry

Cyclic Voltammetry is a simple yet powerful electrochemical technique which is widely used to obtain details about molecular structure and reaction kinetics. It is used here to probe the properties of the nanoporous phthalocyanine thin films when deposited upon an electrode. Known electroactive probe molecules of various sizes and charges have been used in cyclic voltammetry experiments using a filmed electrode as the working electrode, and the results analysed against a bare control. Kinetic properties of the thin-films were then analysed using Digielch 2.1, a computer program for the simulation and fitting of cyclic-voltammograms, created by Manfred Rudolph of the Institut für Anorganische und Analytische Chemie[14].

4.2 Experimental Details

4.2.1 Thin-film preparation

All phthalocyanine derivatives were dissolved in chloroform, due to the high volatility of the solvent and the derivatives' high solubility in chloroform. The derivatives were dissolved at two concentrations, $1x10^{-5}$M and $1x10^{-4}$M, in order to investigate the optimal concentration for deposition of the films.

The substrate used for deposition changed depending on the analytical method being undertaken. SKN studies were performed on a substrate made up of a screen-printed gold electrode surrounded by an insulating border. AFM and Raman studies were carried out on a freshly-cleaved piece of highly-ordered pyrolytic graphite (HOPG). Thin-films for use in cyclic-voltammetry experiments were deposited on a glassy-carbon working electrode.

Preparatory to deposition, all substrate surfaces were cleaned with acetone and then deionised water, before being left in an oven at 80^{0}C for 30 minutes. A freshly-calibrated Gilson micropipette was then used to deposit 50µl of derivative in chloroform onto the substrate surface. The substrate was then left in a stoppered test-tube filled with a small quantity of chloroform to create a chloroform-rich atmosphere. These were left overnight to ensure evaporation before being removed from the tube, washed gently with distilled water and dried with nitrogen.

4.2.2 Scanning Kelvin Nanoprobe Microscopy

For the SKN measurements, a substrate consisting of a screen-printed gold electrode surrounded by a dielectric layer was chosen. This substrate was chosen for two reasons; firstly, the contrast in contact potential difference between the conducting gold substrate and the insulating surround allowed for a baseline value

for the conducting substrate, and secondly, the electrode was able to be easily conductively connected to the piezo table of the SKN, to allow charge to flow between them. The screen-printed electrodes were prepared by Gwent Electronic Materials. The derivative was deposited as described in section 4.2.1.

SKN scans were carried out in standard conditions, but inside an enclosed environment to minimise air movements and vibrations. The SKN tip was constructed of tungsten, with a diameter of roughly 100nm. The large-scale scans were taken in a 2x2mm square area, with distance between data points of 10μm. Smaller scale detailed scans were taken in a 25x25μm area with distance between data points of 1μm.

4.2.3 Atomic Force Microscopy

For the AFM measurements, a highly-ordered pyrolytic graphite (HOPG) substrate was chosen. HOPG was chosen due to its exceptional flatness when freshly-cleaved, which makes it an excellent substrate for AFM work. 10x10x1mm slices of SPI-2 grade HOPG were ordered from Structure Probe Inc (SPI) Supplies, and cleaved onto adhesive tape just before the cleaning and deposition process detailed in 4.2.1. $1x10^{-4}$ and $1x10^{-5}$M films were prepared.

AFM studies were conducted on a Digital Instruments Multimode SPM, managed by a Nanoscope IV controller. Experiments were carried out in the instrument's tapping contact mode, with both topographical and phase maps (used to determine surface elasticity) saved of the same areas. The areas scanned were at 2x2μm for large-scale structural imaging, and 500x500nm for detailed, smaller scale scans.

4.2.4 Confocal Raman Microscopy

Confocal Raman Microscopy substrates were prepared on HOPG in the same manner as the AFM substrates and were mounted on glass microscope slides with

adhesive tape prior to spectrum collection. Raman measurements were performed with a confocal hole diameter of 300μm and slit width of 150μm and a acquisition time of 45s. The Raman microscope was calibrated at 520cm^{-1} using a block of pure silicon before every group of scans.

4.2.5 Cyclic Voltammetry

Phthalocyanine-derivative filmed electrodes were prepared as shown in section 4.2.1. The electrodes used were a BASi MF-2012 glassy carbon working electrodes, a 1cm 2 platinum counter electrode prepared by the departmental glassblowers and a BASi MF-2078 Ag/AgCl reference electrode. Cyclic voltammetry measurements were performed using a Princeton Applied Research VMP multichannel potentiostat. All experimental solutions were originally prepared with a 1x10^{-3} mol dm^{-3} solution of the probe molecules dissolved in de-ionised water containing a 1x10^{-2}M concentration of KNO_3. All chemicals except the phthalocyanine derivatives and the Fe(di-SO_3-batho-phen)$_3^{4-}$ were sourced from Sigma-Aldrich, the Fe(di-SO_3-batho-phen)$_3^{4-}$ was synthesized by Nilotpal Barooh in Durham according to previously published procedure[15].

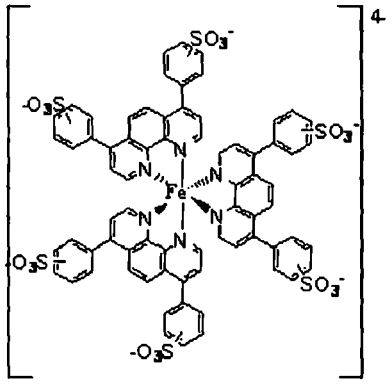

[Fe(di-SO_3-batho-phen)$_3$]$^{4-}$

Figure 4.2.5.1 Molecular structure of Fe(di-SO_3-batho-phen)$_3^{4-}$

4.3 Results and Discussion

4.3.1 Molecular Modelling

Molecular modelling took place in Hyperchem 6, a molecular modelling program for use with a Windows PC, published by Hypercube. Inc[16].

Construction of the Pc structure required the adoption of arbitrary valence for the central silicon atom, allowing an octahedral geometry to be assumed. For each compound, two geometry optimisations were run. In each case, the first of these optimisations was performed on the unrestrained molecule so as to find a local minimum for the structure in the gas phase. Two torsional restraints were then applied between the silicon atom and the two ligands in order to force the aromatic rings in the ligands into a more parallel orientation with respect to the Pc plane. A second geometry optimisation was run on these restrained structures and an energy difference between the two orientations was then calculated for each compound.

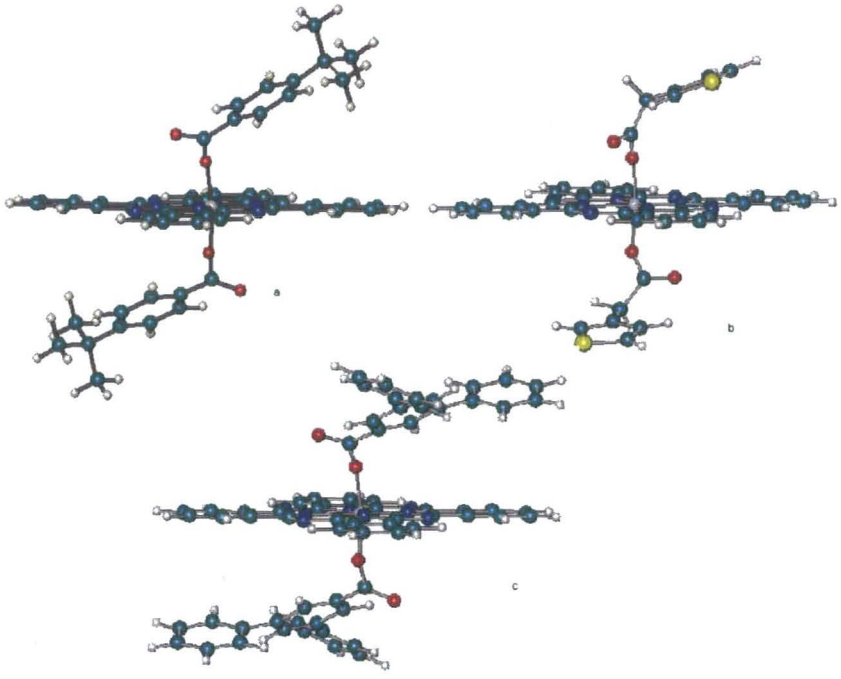

Figure 4.3.1.1: Energy-minimised molecular models of the three phthalocyanine derivatives.

Table 4.3.1.2: Calculated energy values and differences for all phthalocyanine structures.

Compound	Total energy of unrestrained structure (kcal/mol)	Total energy of restrained structure (kcal/mol)	Calculated energy difference (kcal/mol)
1a	-242356.874	-242347.256	9.62
1b	-216692.231	-216690.796	1.44
1c	-289527.137	-289518.044	9.09

These energy calculations act as a guide to explaining the observed surface properties of the different Pc derivatives. It is therefore important to note that two assumptions must be taken into account when considering these optimised structures:

Firstly, the calculated energy differences will not take into account the possibility of an energy maximum between the two structures which would represent a greater energy barrier. However, it can be said that the values of these energy differences are sufficiently low that these geometrical changes can be achieved when molecules are ordered on the surface.

Secondly, ordering of the molecules upon the surface of the high order pyrolytic graphite (HOPG) takes place in solution and not in the gas phase; therefore the actual energy differences between these structures may be lower due to solvation effects.

As expected, compound **a** gives the largest energy difference between the two optimised structures due to the sterically bulky *tert*-butyl groups and this compound displays the least ordering upon the graphite surface. Irrespective of the angle between the ligands' aromatic rings and the Pc plane, the butyl groups result in a poor interaction between the compound and the surface.

The energy difference for compound **c** is not noticeably lower than that for compound **a**. The high degree of ordering of the molecule upon the graphite surface is most likely due to both the increased number of aromatic rings in the axial ligands giving a better electronic interaction with the graphite, and the favourable orientation afforded by the degree of rotation of the additional phenyl rings.

The main consequence of the additional methylene spacer in compound **b** is that smaller rearrangement energy is needed to adopt a favourable orientation for interaction with the graphite surface. The torsional strain placed on the ester linkage is therefore reduced and the observed energy difference is noticeably lower. The fact that **c** gives the highest degree of ordering on the graphite surface indicates

that the overriding factor in the ordering of these films is the number of aromatic moieties within the ligand, and not the degree of rotational freedom within the ligands.

An energy minimization of four molecules of **c** was performed via the Polak-Ribiere method (with an RMS gradient of 0.1) and suggested the formation of nanoporous sieve-like structures with the four molecules arranged in a cross-like formation with an interstice of *ca.* 0.9 nm diameter (Fig 4.3.1.2)

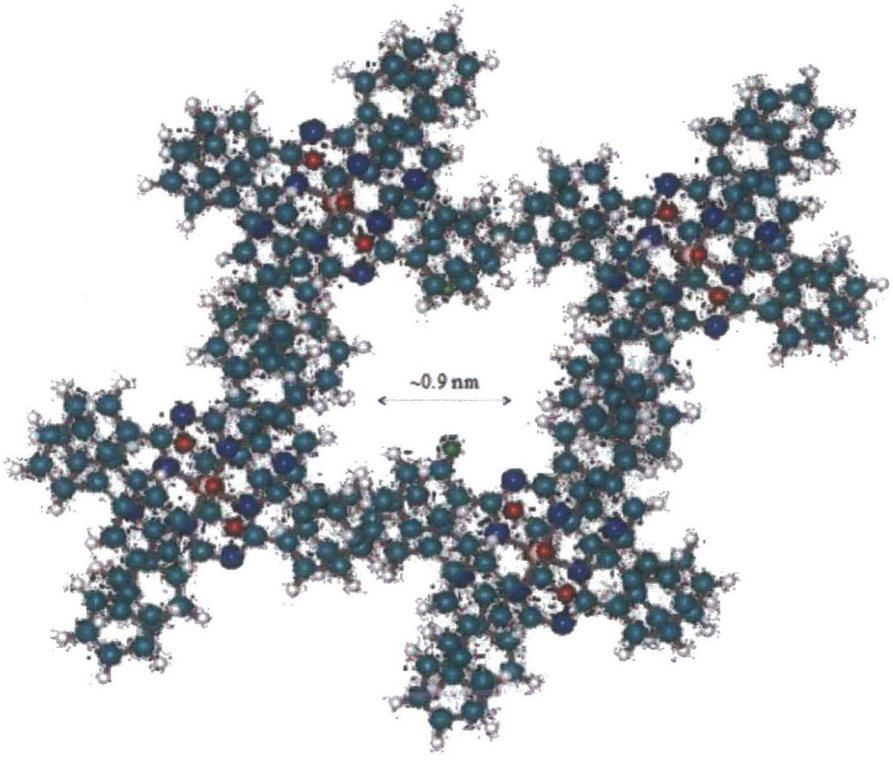

Figure 4.3.1.3: Energy-minimised arrangement of four molecules of silicon phthalocyanine bis(3,5-diphenyl)benzoate, showing a nanopore of approximately 0.9nm in diameter.

4.3.2 Scanning Kelvin Nanoprobe Microscopy

The SKN was used to scan bare screen-printed gold electrodes as well as electrodes treated with a thin-film of compound **c**, the silicon phthalocyanine bis(3,5-diphenyl)benzoate. Full scans were obtained for the bare and filmed electrodes. More negative values are more conducting. Topographical images are not provided here – the SKN has a systemic fault due to the angle of the tip being slightly slanted compared to the piezo table. This does not affect the collection of CPD images, but ensures that topographical images are slanted enough to appear useless.

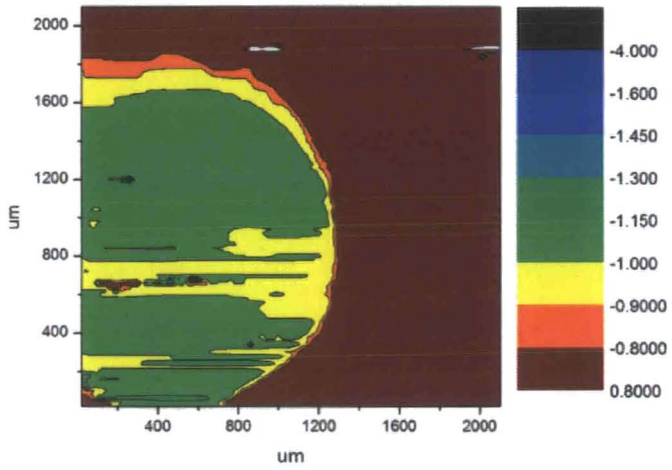

Figure 4.3.2.1: Contour image of bare electrode, showing the conducting and insulating areas.

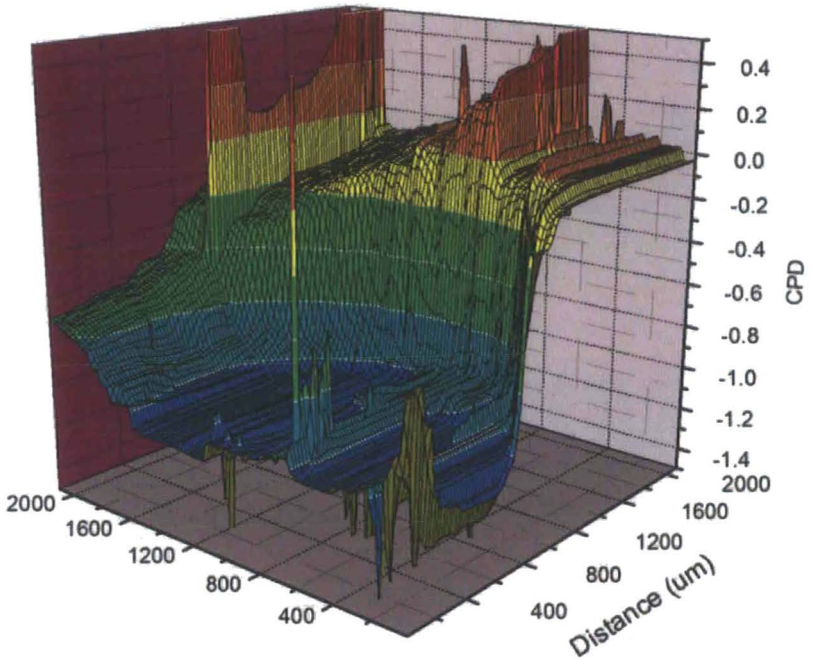

Figure 4.3.2.2: 3 dimensional image of the area in Figure 4.3.2.1.

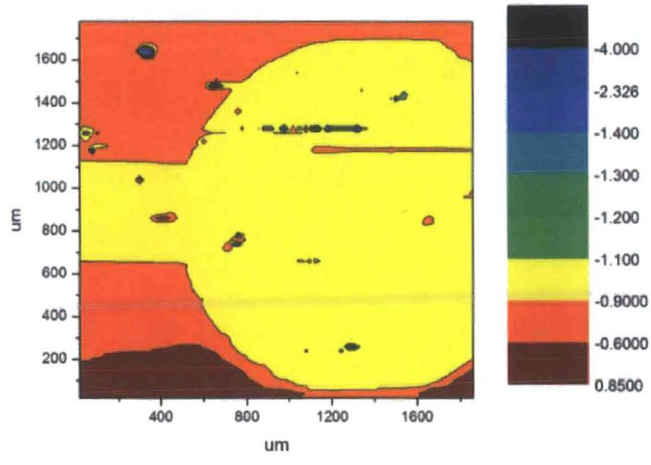

Figure 4.3.2.3: Contour image of electrode coated with compound ***c*** *, showing bare and conducting areas.*

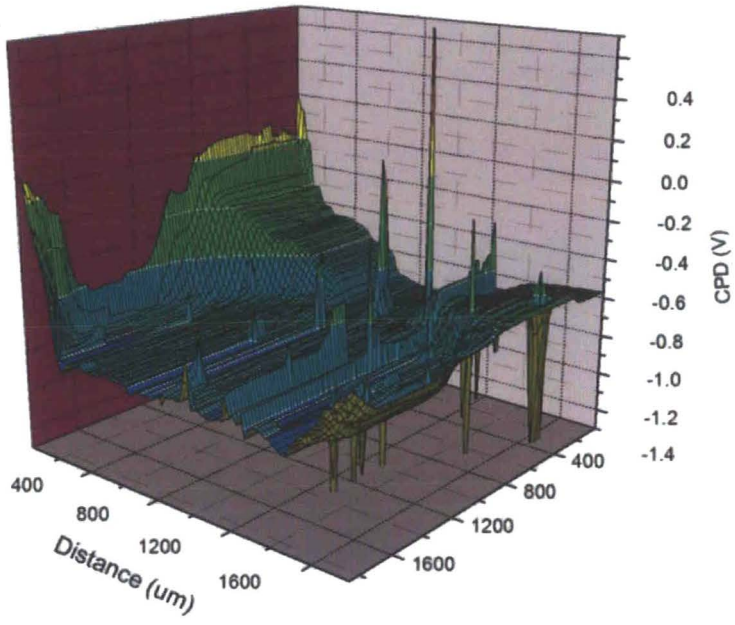

Figure 4.3.2.4: 3 dimensional image of the area in Figure 4.3.2.3.

Figures 4.3.2.1 and 4.3.2.2 clearly show a good contrast between the conducting (more negative CPD values,) and dielectric (more positive values) areas on the electrode surface. The conducting surface was smooth, with an average CPD value of -1.08V on the gold and 0V on the insulator, in line with expected readings. (The more negative the CPD reading, the more conducting the surface). The occasional large spike on the scan is caused by the tip briefly brushing the surface, leading to a sudden and great increase in voltage.

The scan of the film-covered surface in figure 3.3.6.2 indicates a much lesser contrast between the conducting and insulating surfaces covered by the film. The CPD of the conducting surface averages -0.97V and the dielectric surface area covered by the film averages -0.43V. This suggests that the film conducts laterally, shifting charge from more conducting to more insulating areas, which would explain the increase in conductance of the dielectric surround.

The contrast between the bare and filmed electrodes can be viewed most clearly by comparison of the images 4.3.2.2 and 4.3.2.4. These 3d figures, taken from the same virtual observation point, illustrate the large difference the film coverage has had on the dielectric surround, (about 400mV) compared to the conducting surface (about 80-90mV).

The difference in the conducting surface can be viewed directly via detailed surface CPD images of the conducting electrode. These scans show the surface of the bare electrode as well as the surface of the electrode when covered with compound **c**. The SKN probe tip was used to create a thin scratch in the film to enable direct imaging of the CPD difference between the uncovered and filmed gold.

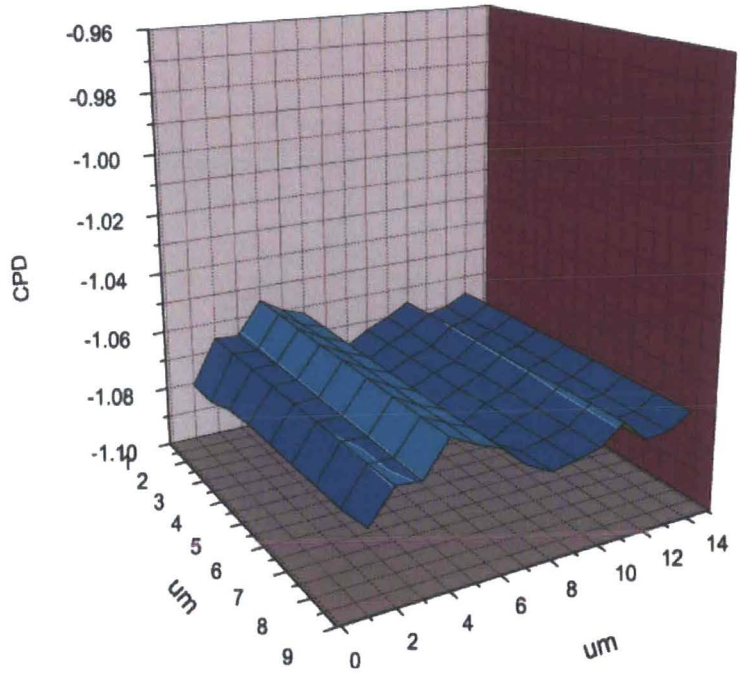

Figure 4.3.2.5: Detailed SKN scan of bare gold electrode.

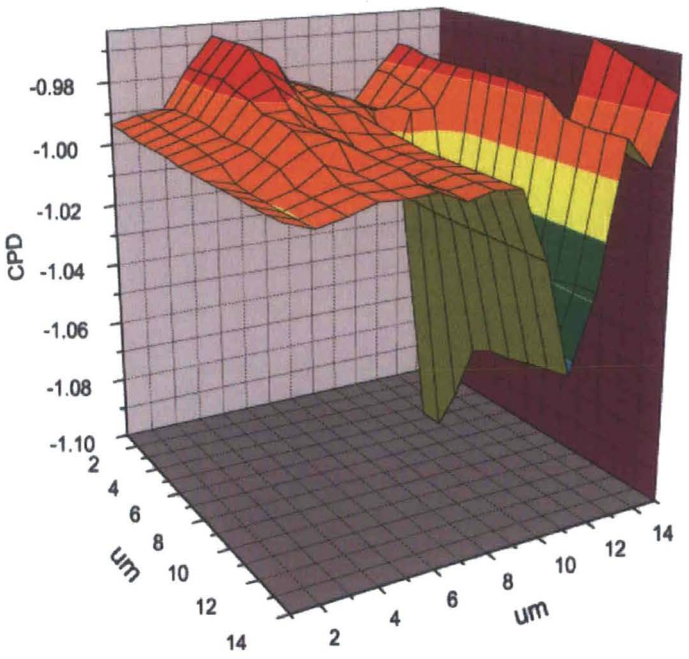

*Figure 4.3.2.6: Detailed SKN scan of gold electrode coated with **c**.*

The scratch in the film shows clearly the CPD difference between the thin film and the gold. In contrast, the conducting gold surface has changed far less, becoming 80mV more insulating, a change appropriate with the presence of a monolayer film of approximately 2nm thickness (see Chapter 6 for more details).

4.3.3 Atomic Force Microscopy

AFM images were obtained from $CHCl_3$ solutions of compounds **a**, **b** and **c** evaporated onto freshly cleaved surfaces of highly ordered pyrolytic graphite (HOPG) focussed on the basal plane. A scan was performed on the freshly cleaved basal plane of the HOPG before deposition in order to confirm the flatness of the substrate.

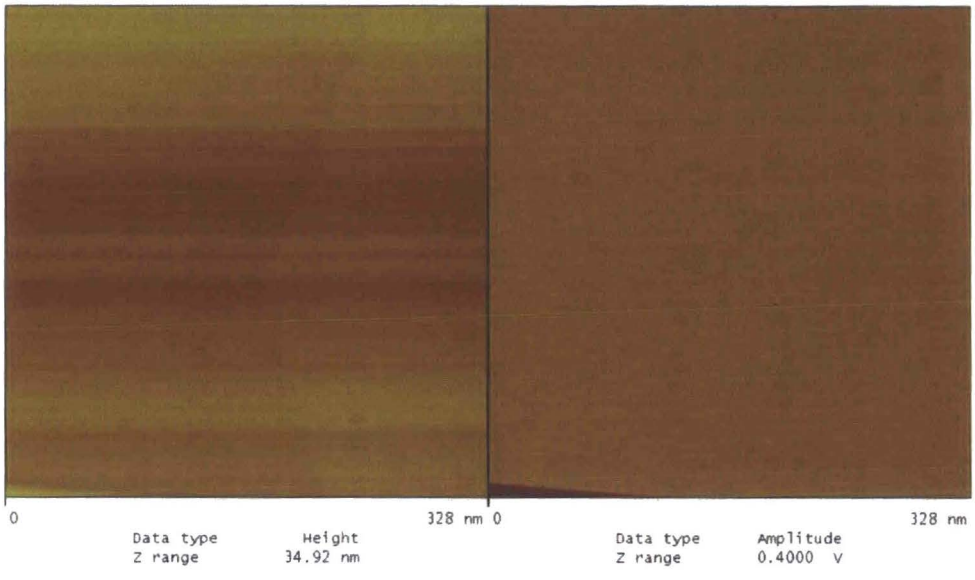

Figure 4.3.3.1: 320nm wide AFM scan of basal plane of freshly-cleaved HOPG. RMS roughness: 0.145nm.

Images of **c**, silicon phthalocyanine bis(3,5-diphenyl)benzoate, at $1x10^{-5}$M showed small islands of aggregated derivative, approximately 30nm in diameter, surrounded by bare surface.

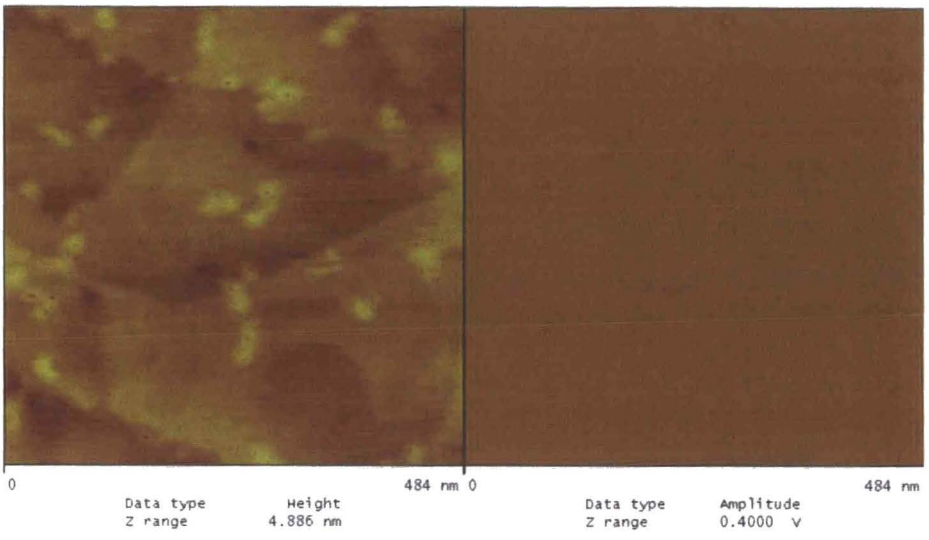

Figure 4.3.3.2: AFM scan of deposition of compound ***c*** *on HOPG at 1x10^{-5}M concentration. RMS Roughness: 0.3nm.*

At a concentration of 1x10^{-4}M, larger, dome-shaped aggregations begin forming across the surface. Larger quantities of phthalocyanine have formed, and seem to cover the surface almost contiguously. The fuzzy sections on the lower right of the scan are where the height-tolerance of the AFM tip has been exceeded. The darker areas on the topography map are where there are holes of little-to-no coverage over the substrate.

The phase map on the right shows an area of 'bubble' structure, of similar sizes to the topographical globules seen on the left, about 200-300nm in diameter. The structures seem to consist of a central 'nucleus', of about 30nm across, and a circular 'wall' about 100nm from the nucleus. The structures can be seen in greater detail in the zoomed-in scan in figure 3.3.2.7. Note that darker areas on the phase scan do not correspond to areas of lower height, but to areas which showed greater adhesion to the probe tip. The phase map therefore shows areas of hardness, with a 'sticky' edge and a very hard nucleus.

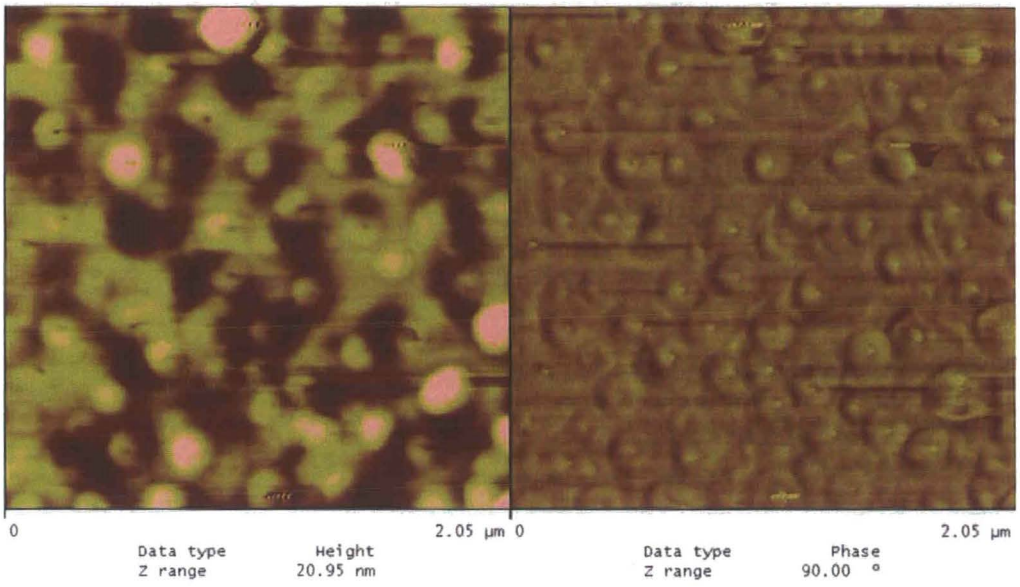

*Figure 4.3.3.3: AFM scan of deposition of compound **c** on HOPG at 1x10^{-5}M concentration. RMS roughness: 6.3nm.*

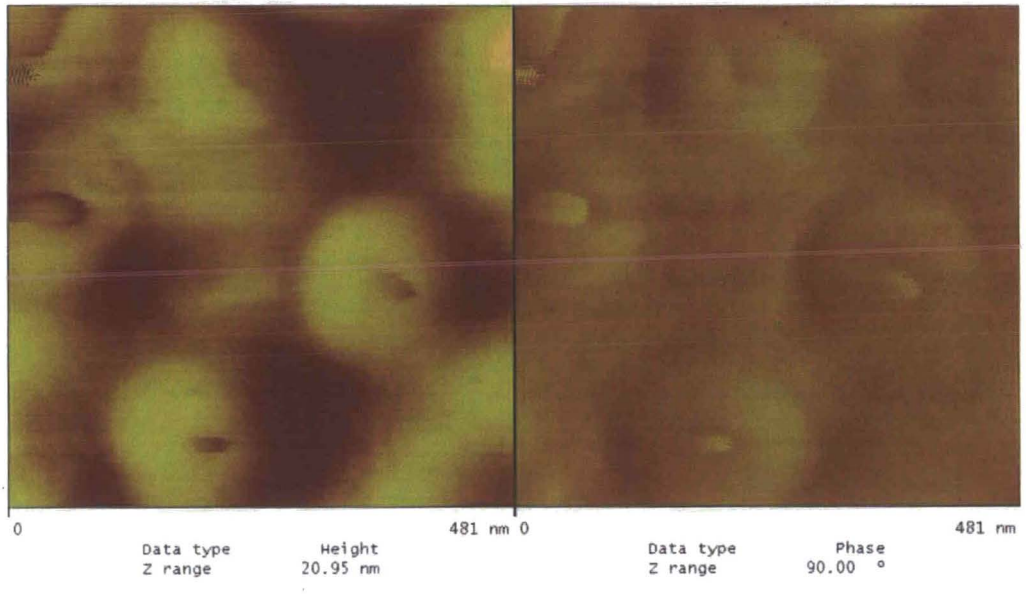

Figure 4.3.3.4: Detailed scan of part of Figure 4.3.3.3.

This structure appears to support the notion that the large axial 3,5-diphenyl benzoate substituents attached to the central silicon in compound **c** discourage large scale crystalline aggregation, due to the axial substituents blocking the π- π interactions between the phthalocyanine rings.

The phase images at 0.1 mmol dm-3 concentrations indicate that compound 1a covers the HOPG surface (Fig. 6a). At 0.01 mmol dm-3 concentrations, however, discrete islands of 1a were observed with the molecules tending to align along the edge-plane of HOPG (Fig. 6a'). At similar concentrations, compound 1b appears to form microfibril-like structures (Fig. 6b and b'), an observation which could probably be explained by previous work[17] in which MALDI-TOF mass spectra suggested that compound 1b formed μ-oxo-bridged dimeric structures, a phenomenon observed in several bis-substituted silicon phthalocyannines. A film with a porous structure appears to form with compound 1c, which was designed to enhance π–π interaction between the axial ligands (Fig. 6c and c').

4.4.4 Confocal Raman Microscopy

Confocal Raman microscopy was used to obtain spectra of a $1x10^{-4}$M deposition of compound **c** of HOPG. The bare surface of HOPG was imaged before deposition to provide a background spectrum.

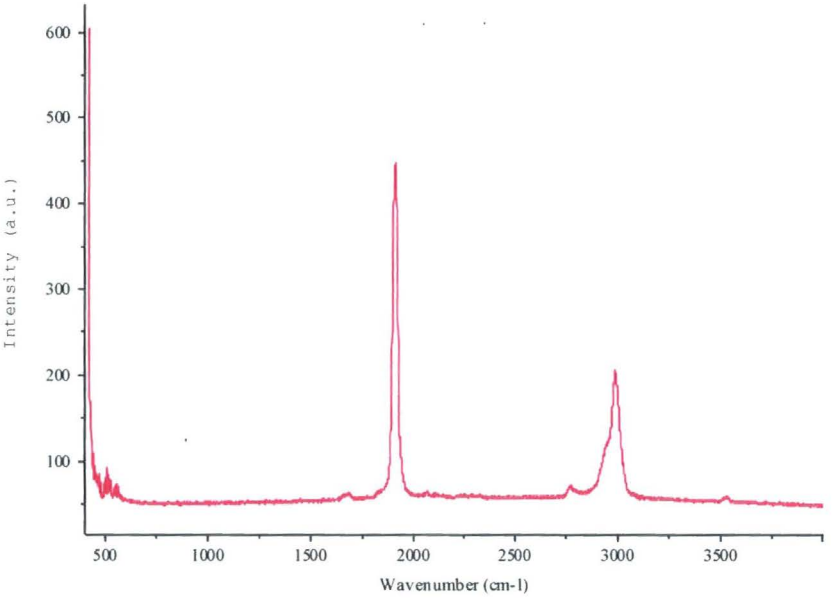

Figure 4.4.4.1: Raman spectrum of freshly-cleaved bare HOPG.

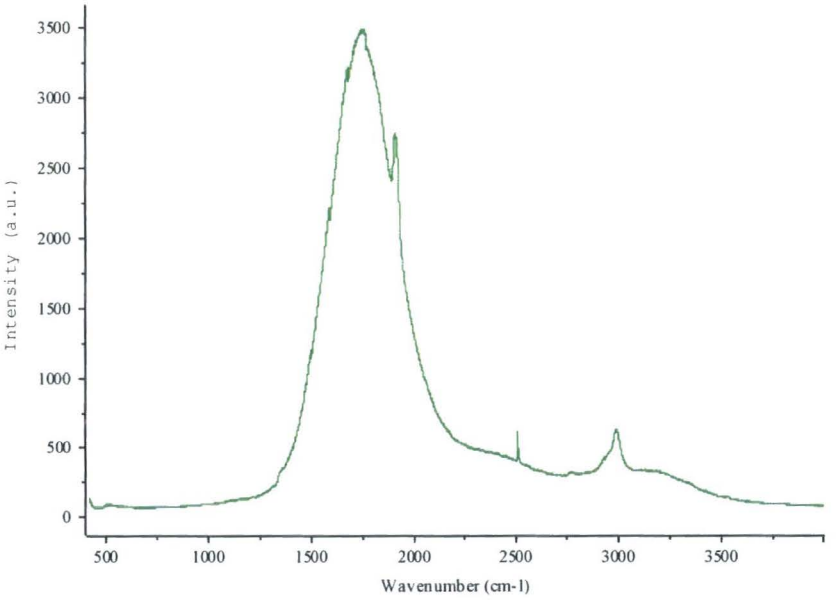

*Figure 4.4.4.2: Raman spectrum of thin-film of **c** deposited on HOPG.*

Figure 3.3.9.1, the Raman spectra of the plain HOPG shows a standard baseline, with the two peaks representing the basal and edge planes of HOPG clearly visible as sharp peaks at 1850 and 3000 cm^{-1}. 3.3.9.2, the phthalocyanine-filmed HOPG,

shows a very intense broad peak with the midpoint at 1700 cm^{-1}. This is in the C-C bond-stretching range for Raman spectra, and as such corresponds to the wide range of aromatic C-C bonds present in the phthalocyanine derivative. The peak is almost certainly wider and more intense then may be expected due to the large quantity of different orientations of the phthalocyanine molecules in the film, another confirmation that they do not form a regular crystalline structure. The HOPG basal peak can still be seen on the side of this peak at 1850cm^{-1}.

4.4.5 Cyclic Voltammetry

Cyclic voltammetry was used to investigate the blocking abilities and structure of the thin-film when deposited on an electrode. This was done by analysing the response received when electroactive probe molecules of various size and charge were scanned using standard cyclic voltammetry techniques.

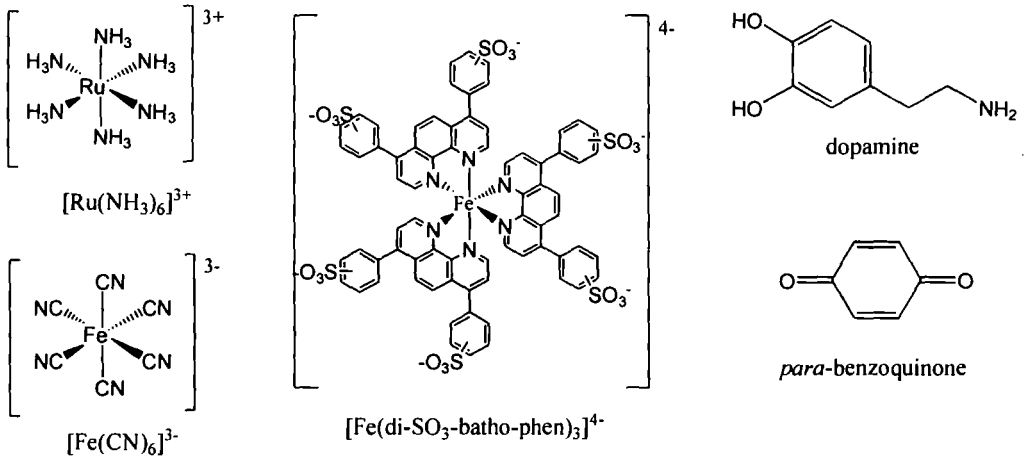

Figure 4.4.5.1: Molecular structures of electroactive probe molecules used in cyclic voltammetry experiments.

Five molecular probes were used. $[Ru(NH_3)_6]^{3+}$] and $[Fe(CN)_6]^{3-}$ are spherical molecules, with a diameter of approximately 0.6 nm. Dopamine and *para*-

benzoquinone are roughly rectangular, with diameters of 0.3×0.5×0.6 nm and 0.3×0.6×0.8 nm respectively. $[Fe(di\text{-}SO_3\text{-}batho\text{-}phen)_3]^{4-}$ has a diameter of approximately 2.4 nm. These probes were selected for their differing size and charge properties, allowing both the size- and charge- selectivities of the films to be tested. Cyclic voltammograms were taken using the molecular probes of the three phthalocyanine derivatives filmed onto glassy carbon electrodes at scan rates between 10-500 mV/s, using the procedure detailed in section 4.2.5.

Cyclic voltammograms of $[Ru(NH_3)_6)^{3+}]$ for the bare electrode and the three derivative-filmed electrodes are shown below. The horizontal axis represents potential in volts, the vertical the current response in amperes.

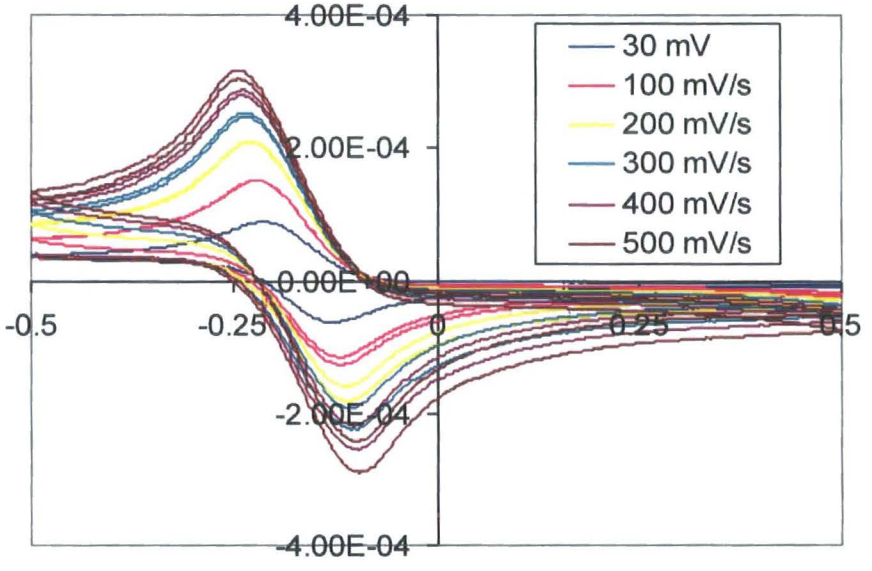

Figure 4.4.5.2. Cyclic voltammetry scans of $[Ru(NH_3)_6)^{3+}]$ using a bare glassy carbon electrode between 30-500 mV/s.

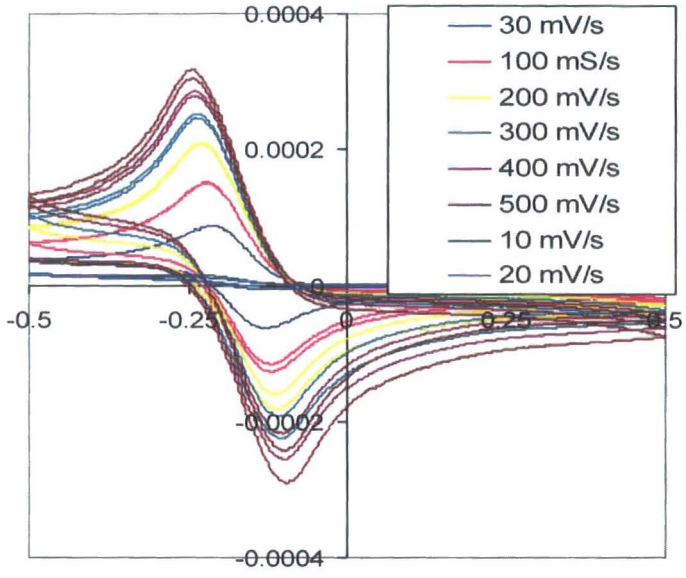

Figure 4.4.5.3. Cyclic voltammetry scans of $[Ru(NH_3)_6)^{3+}]$ using a silicon phthalocyanine bis(3,5-triphenyl)benzoate filmed glassy carbon electrode between 30-500 mV/s.

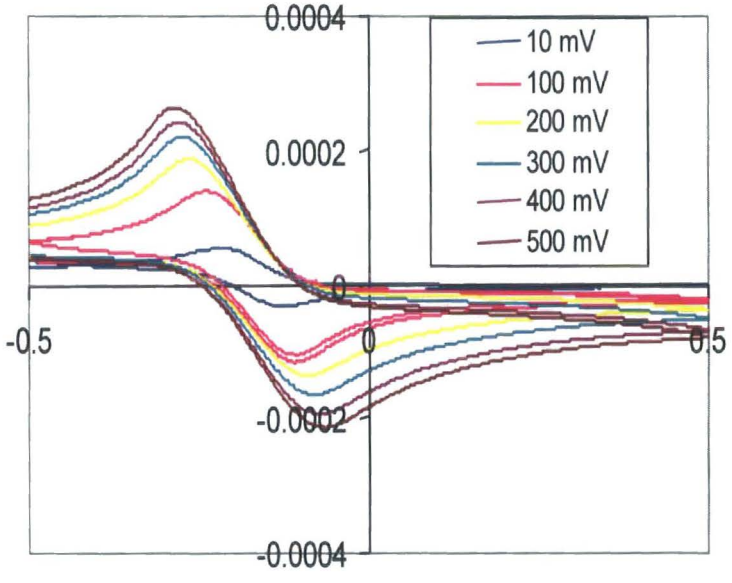

Figure 4.4.5.4. Cyclic voltammetry scans of $[Ru(NH_3)_6)^{3+}]$ using a silicon phthalocyanine bis-(3-thienyl)acetate filmed glassy carbon electrode between 10-500 mV/s.

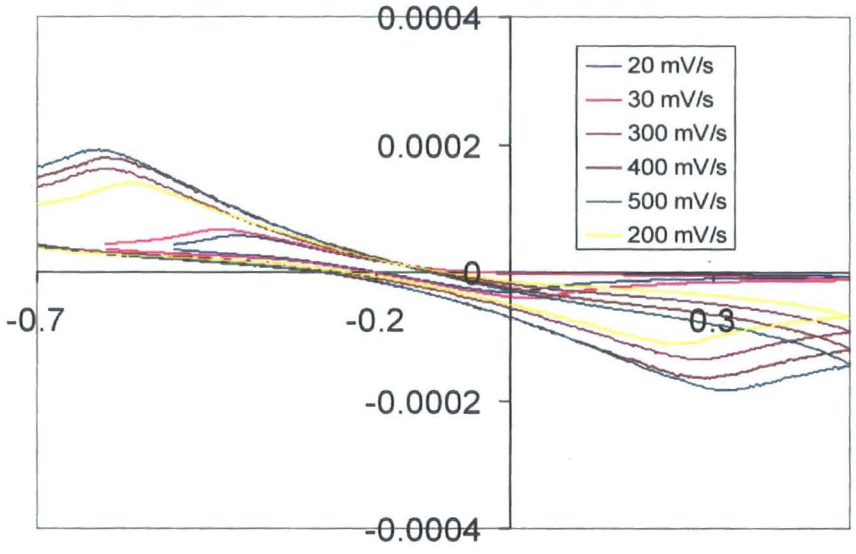

Figure 4.4.5.5. Cyclic voltammetry scans of $[Ru(NH_3)_6]^{3+}$ using a silicon phthalocyanine bis(4-tert-butylbenzoate) filmed glassy carbon electrode between 20-500 mV/s.

These results show the great variety of responses seen from the different phthalocyanine derivatives. The bis(3,5-diphenyl benzoate) derivative showed a very similar electrochemical response, showing that the ruthenium complex was able to penetrate the film readily, with no change in the diffusion coefficient or the rate of reaction. The bis-(3-thienyl)acetate derivative showed a slight lessening of the peak height and a widening of the peak-to-peak separation, indicating a slower rate of reaction and a decreased diffusion coefficient. This shows that the ruthenium complex has greater difficulty penetrating this film. The bis(4-tert-butylbenzoate) derivative showed an extreme peak-to-peak separation and a dramatic lessening of the peaks, demonstrating that this film manages to block the ruthenium complex far more completely then the other two complexes.

Different probe molecules led to dramatically differing results, as can be seen in these cyclic voltammograms of $[Fe(di\text{-}SO_3\text{-batho-phen})_3]^{4-}$].

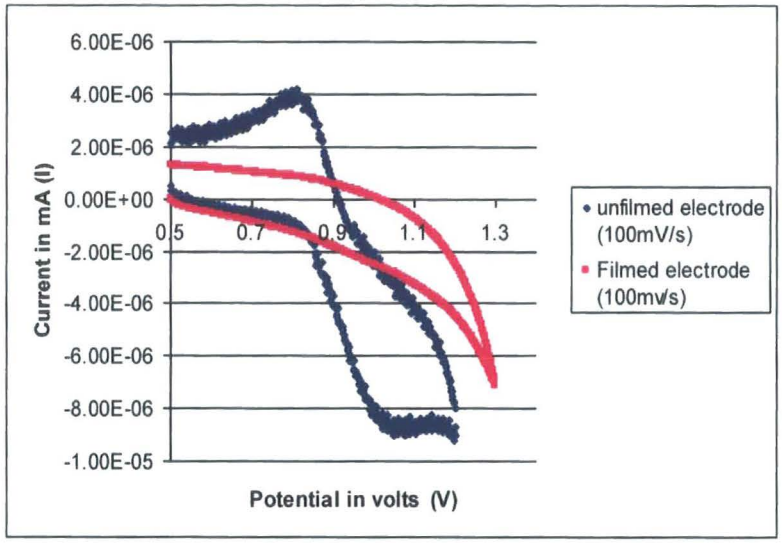

Figure 4.4.5.5. Cyclic voltammetry scans of $[Fe(di\text{-}SO_3\text{-}batho\text{-}phen)_3]^{4-}$ at a scan rate of 100 mV/s using bare and silicon phthalocyanine bis(3,5-triphenyl)benzoate filmed glassy carbon electrodes.

This graph clearly shows that the large $[Fe(di\text{-}SO_3\text{-}batho\text{-}phen)_3]^{4-}$ complex is completely blocked by the bis(3,5-triphenyl)benzoate filmed electrode, eliciting no electrochemical response. This, compared to the earlier $[Ru(NH_3)_6)^{3+}]$ results, shows that the bis(3,5-triphenyl)benzoate derivative has a size-selective blocking ability. The computational modelling conducted in section 4.3.1 predicted an interstice of approximately 0.9 nm in the arrangement of the bis(3,5-triphenyl)benzoate derivative on the surface – these cyclic voltammograms would appear to suggest that an interstice greater than 0.6 nm but less than 2.4 nm exists.

The results from the cyclic voltammograms were imported into Digielch 2.1, an electrochemical simulation and fitting software package. Digielch has the ability to compute the electrochemical response current and the concentration profiles at the electrode surface for any defined electrochemical mechanism. (See section 2.2.4).

Electrochemical simulations were set up for the five probe molecules. Standard conditions were assumed, and the reactions were assumed to be completely reversible (α value of 0.5). The number of electrons transferred, n, was set to one except in the case of dopamine, which reacts with a two-electron transfer

mechanism. The two values being fitted, the heterogeneous electron transfer rate constant k_s and the diffusion coefficient D, were set to standard literature values[18] for the initial simulation. For [Fe(di-SO_3-batho-phen)$_3$]$^{4-}$], no literature values were available. The values seen here were calculated using Digielch and he bare electrode simulation data.

Multiple sets of cyclic voltammetry data at different scan rates were fitted simultaneously to increase the accuracy of the fitted results. The simulation run was a fixed-grid type, with simulation occurring using the Butler-Volmer equation (see section 2.1.4). Iterative fitting was accomplished using the Monte Carlo statistical method.

Table 4.4.5.7. Table of values obtained for k_s and D using the Digelch electrochemical simulation software package.

Probe	Bare electrode		(butyl)benzoate		3-thienyl)acetate		3,5-triphenyl benzoate	
	k_s (cm s^{-1})	D (cm^2 s^{-1})	k_s (cm s^{-1})	D (cm^2 s^{-1})	k_s (cm s^{-1})	D (cm^2 s^{-1})	k_s (cm s^{-1})	D (cm^2 s^{-1})
$[Ru(NH_3)_6]^{3+}$	6.0E-02	7.1E-06	1.0E-04	7.0E-06	5.2E-04	6.9E-06	5.2E-02	7.0E-06
Benzoquinone	5.0E-02	6.6E-06	1.4E-02	5.7E-06	3.4E-02	6.3E-06	4.2-02	6.3E-06
Dopamine	5.1E-02	8.0E-06	2.3E-05	5.2E-06	5.0E-05	6.5E-06	3.0E-04	6.5E-06
$[Fe(CN)_6]^{3-}$	5.9E-02	7.4E-06	0.0	0.0	0.0	0.0	0.0	0.0
$[Fe(di\text{-}SO_3\text{-}batho\text{-}phen)_3]^{4-}$	3.2E-04	5.0E-07	0.0	0.0	0.0	0.0	0.0	0.0

The results in the table above suggest that all three phthalocyanine films are charge- and size- selective with respect to the probe molecules used. $[Ru(NH_3)_6]^{3+}$ dopamine and *para*-benzoquinone show penetration of the film, though at decreased rates and diffusion coefficients compared to the bare electrode. Of these three probe molecules, benzoquinone displayed the largest rate constant in all three films. This is due to its small linear cross-section, the smallest of all the molecules, which allows it to diffuse through the pinholes in the film at the greatest rate.

Neither $[Fe(CN)_6]^{3-}$ or $[Fe(di\text{-}SO_3\text{-}batho\text{-}phen)_3]^{4-}$ showed any penetration of the film. These molecules are both highly negatively charged, which suggests a charge-repulsion effect between these molecules and the electron-rich phthalocyanine layer. In the case of $Fe(di\text{-}SO_3\text{-}batho\text{-}phen)_3]^{4-}$, the molecule may also be too large to penetrate the films. A positively-charged or neutral probe molecule of similar size was needed to test this theory. However, unfortunately none was available.

In the case of the 3,5-triphenyl benzoate film, the diffusion rates noted for the uncharged dopamine and *para*-benzoquinone molecules were significantly higher than those recorded with the 4-tert-butylbenzoate and the (3-thienyl)acetate films, suggesting that the interstices in the 3,5-triphenyl benzoate are larger than those in the 4-tert-butylbenzoate films. Dopamine shows a greatly lower k_s value than *para*-benzoquinone for the 3,5-triphenyl benzoate film, (Dopamine $3x10^{-4}$, *para*-benzoquinone $4.2x10^{-2}$). This is unsurprising, as the molecular dimensions of dopamine are beginning to approach the size of the phthalocyanine film interstices calculated in section 4.3.1.

4.5 Conclusions

The investigation of the phthalocyanine derivatives has led to some very interesting findings. The principal derivative investigated was silicon phthalocyanine bis(3,5-diphenyl)benzoate, which was specifically designed to resist crystalline aggregation by the addition of large axial aromatic groups, forming amorphous thin-films when deposited on material. Two other derivatives were investigated and were expected to crystallise to a greater extent than the (3,5-diphenyl)benzoate, though still maintaining a degree of amorphous behaviour.

Simple molecular modelling was carried out on the three derivatives to investigate their minimised-energy configurations and the extent of surface interaction. The bis(3,5-diphenyl)benzoate derivative showed the greatest ability to interact with a surface due to its greater level of aromatic moieties. A set of four molecules was placed in an energy-minimised configuration, and showed an interstice between the molecules of approximately 0.9nm in diameter.

SKN measurements were carried out of the bis(3,5-diphenyl)benzoate derivative, deposited on a screen-printed gold electrode. These measurements showed an 85-90mV difference between the CPD of the bare gold and the derivative-filmed electrode. This was confirmed by producing a scratch on the filmed surface with the probe tip. The insulating surround of the electrode became considerably more conductive in character, suggesting that the film forms an electrically conducting layer on the surface.

AFM scans were carried out on freshly-cleaved HOPG section deposited with bis(3,5-diphenyl)benzoate. Phase-mapping showed the formation of soft, dome-like structures centralised around a hard core. The AFM images show that the film formed has very little crystalline structure or character. Confocal Raman microscopy spectra show an intense broad peak in the C-C stretching region, owing to the large quantity of differing molecular orientations present in the disordered amorphous film.

Cyclic voltammetry measurements were carried out using a variety of electroactive probe molecules on electrodes filmed with the three phthalocyanine derivatives. These scans were fitted to simulated cyclic voltammograms using the program Digelch in order to obtain values for the heterogeneous electron-transfer rate constant k_s and the diffusion coefficient D. These results found that all three films were size- and charge- selective, repelling negatively-charged probe molecules due to the electron-rich nature of the phthalocyanine films. The bis(3,5-diphenyl)benzoate derivative film admitted *para*-benzoquinone far more readily then dopamine, suggesting that the size of the interstices present in the film is approximately that seen in the molecular modelling simulations.

References

[1] 'Phthalocyanine Materials - Synthesis, Structure and Function'McKeown, N B, *Cambridge University Press*, 1998, ISBN 0521496233

[2] Phthalocyanine Research and Applications', Thomas, A L, *CRC Press*, 1990, ISBN 084934624X.

[3] Mizuguchi, J.; Matsumoto, S. *J. Phys. Chem. A*, 1999, **103**, 614–616

[4] Brewis M, Hassan B, *Journal of Porphyrins andPhthalocyanines*, 2000, **4**, 460-464.

[5] Kahl J J, Faulkner, L R, *J. Am. Chem. Soc.*, 1986, **108**, 5434-5440.

[6] Toshima N, Kawamura S, Tominaga T, *Chem. Lett.*, 1993, **22,** 1299-1302.

[7] Simpson, T R E, Cook, M J, Revell, D J, *Langmuir*, 1997, **13,** 373-598.

[8] 'The Phthalocyanines – Volume 1' Leznoff, C, Lever, A, *Wiley*, 1998, ISBN 978-0-471-23899-7.

[9] C-L Li, C-Chi Lee, K-Chuan Ho, *Journal of Electroanalytical Chemistry* (2002) **89,** 524-525.

[10] Somashekarappa, M P, Keshavava, J, Sampath, S, *Pure. Appl. Chem*, 2002, **74**, 1609-1620.

[11] Makhseed, S.; McKeown, N. B.; Msayib, K.; Bumajdad, A. *J. Mater. Chem.* 2005, **15**, 1865–1870.

[12] C A Barker, K S Findlay, I F Perepichka, M R Bryce, A Beeby, *Tetrahedron,* 2006, **62,** 9433-9439.

[13] Cheran, L E, Leiss, H D, Thompson, M, *Analyst,* 1999, **124,** 961-970.

[14] http://www.elchsoft.com.

[15] Hupp, J. T. Nguyen, S. T. *Proc. Nat'l. Acad. Sci.*, 2002, **99**, 5171-5177.

[16] http://www.hyper.com.

[17] C. Farren, S. FitzGerald, M. R. Bryce, A. Beeby, A. S. Batsanov, *J. Chem, Soc., Perkin Trans.*2002, ***2,*** 59.

[18] 'Standard Potentials in Aqueous Solutions', *ed* Bard A J, Parsons R, *Dekker,* 1985.

Chapter 5: Investigation of Self-Assembled Monolayers of Thiol-Containing Compounds on Gold.

Organothiol molecules have the ability to form self-assembling monolayers (SAMs) onto gold substrate surfaces. This chapter uses the scanning Kelvin nanoprobe (SKN) to investigate the effect of the length, configuration and functionalisation of organothiol molecules on the resultant change in work function with the formation of the resultant SAM. Electrochemical impedance spectroscopy (EIS) is used as a complementary technique, to study the resistance and capacitance of monlayers formed on gold working electrodes.

5.1 Introduction

5.1.1 Self-assembling monolayers

Self assembling monolayers, often referred to as SAMs, are surfaces consisting of a single layer of molecules deposited on a base substrate. Self-assembling monolayers have the ability to form from a solution of the monolayer molecules placed on the target substrate directly and with no chemical or physical intervention.

A self-assembling molecule can be typically divided into three distinct sections, each with differing chemical properties. The first is the anchoring group, the group which provides the greatest exothermic reaction when adsorbing onto the target substrate. In the case of the substrate being gold, this anchoring group is commonly sulphur, which has a very high (in the region of 85-145kJ/mol) binding energy to gold[1]. The second part is a spacer group, typically an alkyl chain, which separates the anchoring group from the functional or terminal surface group, which provides the properties of the monolayer surface. Self-assembled monolayers typically orient themselves together in a specific manner, which is determined by the affinity between the anchoring group and the surface substrates, as well as intermolecular

forces between the spacer groups and dipolar interactions between the terminal surface groups.

The most commonly encountered SAMs in chemistry tend to be alkylthiols, due to their high affinity for gold and readily understood surface properties. Alkyl silane molecules have been observed to self-assemble on silicon oxide surfaces, a process that could have great relevance for semiconductor engineering[2]. SAMS tend to exhibit different kinetic properties then the free molecule or substrate, and are an excellent model for the study of organic and biological interfaces, as well as interfacial electron transfer and other interface mechanisms.

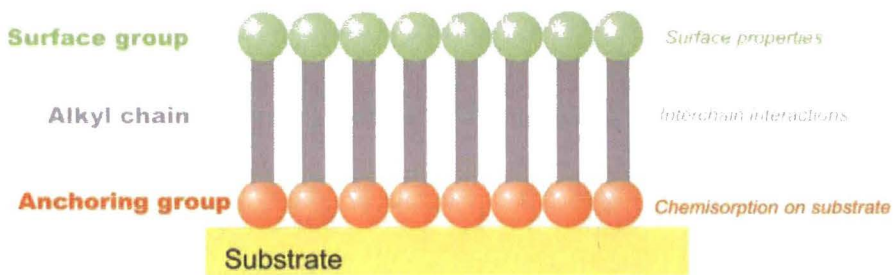

Figure 5.1.1.1: Schematic view of a self-assembling molecular layer, showing the three main sections. (Chico).

5.1.2. Organothiol monolayers

Organothiols are characterised by an adsorbing head thiol group coupled to an organic molecule. The most widely available and cheapest of these are the alkanethiols, simply a –SH group attached to an alkane chain. Due to the similar electronegativity of sulphur and hydrogen, thiol bonds are nonpolar and covalent, and therefore organothiols have lower boiling points and lower solubility in water then the alcohol equivalents.

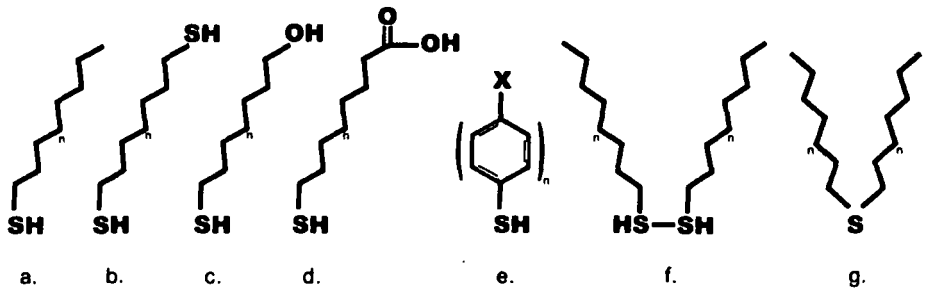

Figure 5.1.2.1. Frequently used organothiols for self-assembled monolayers, showing a) n-alkanethiols, b) n- alkanedithiols, c) n-mercaptoalkanol, d) n-mercaptoalkane carboxylic acids, e) n-Oligophenylthiols, f) n-dialkyl disulfides, g) n-dialkyl sulfides.

Thiols show similar chemistry to alcohols, forming thiolesters and thioethers. Thiol groups are fairly acidic, showing pKas of 10-11, and are readily oxidised to R-S-S-R. This oxidised form has an important role in biochemistry, and is integral to protein folding. The amino acid cysteine has a thiol group, and readily oxidises to cystine, a dimer of two cysteine molecules held together by an S-H bond.

Sulphur has a very high affinity for gold, and so will bind extremely readily when in the presence of a gold substrate. The adsorbtion of an alkanethiol onto gold can be described as an oxidative addition of the S-H bond to the gold, followed by the reductive elimination of hydrogen[3]. When the molecules are densely packed enough on the surface to interact with one another, they begin to repel each other and lift off the substrate surface, held only by the adsorbed sulphur head. The pattern of the adsorbed sulphur atoms upon the substrate surface is believed to be hexagonal to minimise sulphur-sulphur interactions while maximising density, as a hexagonal arrangement is the most efficient packing structure possible[4]. The Au-S-C bond angle is nearly 120^0, found by investigation of the twisting of the alkane backbone from surface normal[5].

The alkyl chains orientate themselves at a 30° angle, which has the lowest free-energy of any closely-packed tethered chain system[6]. Van der Waals forces between methylene groups amount to 1.4-1.8 kcal/mol, which forces the alkyl chains into an

almost all-trans configuration, parallel to each other[7]. 'Islands' of the 30° orientated chains slowly form and cover the surface, in a similar manner to a crystallisation process. Pinholes and other defects can be seen in a monolayer, once again analogously to a crystallisation process[8].

5.1.3 Preparation

Self-assembled monolayers are relatively quick and easy to prepare, with the greatest issues being the purity and cleanliness of the substrate and the solvent used.

Gold substrates should be arranged with the crystal face being in the (111) direction if possible. This can be obtained either by using single-crystal gold or by evaporation of gold films onto a flat surface, such as a silicon or glass slide[9]. This substrate should be immersed into a 1-2mM solution of the desired thiol in an organic solution. Thiols do not readily dissolve in water, and indeed dry solvents should be used if at all possible, due to the possible inclusion of water into the monolayer, which will affect its quality and properties. The most commonly used solvent for SAM formation is ethanol, due to its availability and low cost. When preparing mixed monolayers of two or more organothiols, it is imperative to check the relative solubilities of each organothiol, as this will directly affect the percentage of each molecule in the monolayer.

Although adsorption occurs very quickly, to obtain high-quality and defect-free monolayers it is advisable to leave the substrate in the solution for at least 6, and preferably 15 hours. Substrates with deposited monolayers must be rinsed and dried to remove excess solvent and unadsorbed molecules, which will affect the properties of the surface.

Alternative methods of preparing monolayers involve vapour-phase transfers between substrates with differing surface energies. Polydimethylsiloxane (PDMS) is a commonly used substrate for this technique, known as soft lithography. The

inorganic siloxane backbone in PDMS, after polymerisation and cross linking, will present the methyl group, which has very weak intermolecular forces, to the surface of the polymer. This makes the surface of a PDMS structure hydrophobic and possessing extremely weak surface energy. As PDMS is elastomeric, it is an extremely good material for stamping, as it will press and mould to the substrate surface. A PDMS stamp can therefore be immersed in an organothiol solution long enough for a self-assembled monolayer to form on its surface. The stamp can then be taken and pressed against a gold substrate, enabling vapour-phase transfer of the monolayer to the higher surface-energy gold substrate. This process takes around twenty seconds, and creates high-quality substrates which are patterned by the topography of the PDMS stamp.

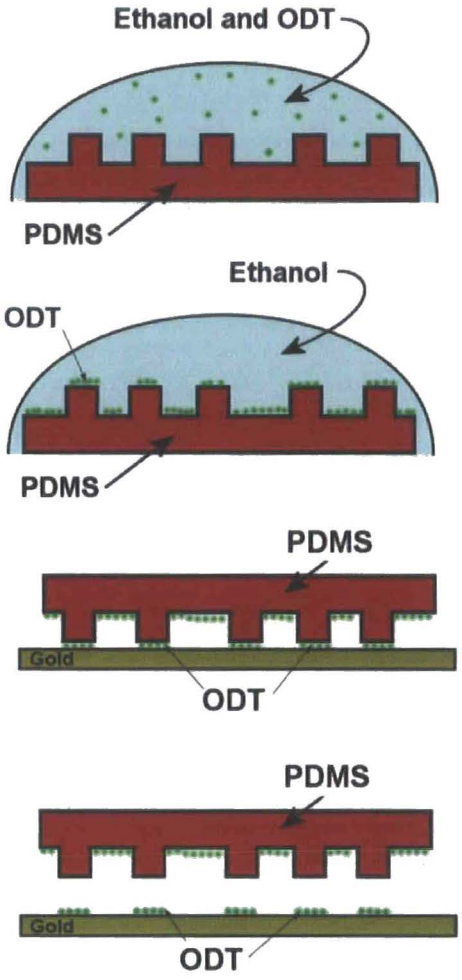

Figure 5.1.3.1: Series of diagrams showing the process by which octadecanethiol (ODT) is adsorbed onto a PDMS stamp before subsequently being transferred onto a gold substrate surface.

5.1.4 Objectives

This chapter details a systematic study of self-assembled organothiol molecules on gold substrates. The study was carried out using scanning Kelvin nanoprobe (SKN) and electrochemical impedance spectroscopy. The objective of the study is to investigate how contact-potential difference measurements are affected by differing monolayer conditions, and to do so in a systematic way which will allow prediction of future measurements.

Contact-potential difference is a complicated value, being intrinsically bound up with the work function of a material, which itself is affected by many factors, both environmental and intrinsic to the material. To make a useful measurement of a material therefore, environmental factors such as temperature and humidity must be controlled, and the measurements must be compared within a framework of similar measurements to be interpreted correctly. This investigation aims to provide such a framework for the case of organothiol monolayers, by measuring thiol compounds of differing length and functionality and comparing the results directly.

When a thiol molecule forms a self-assembled monolayer onto gold, the effective dipole of the molecule will point towards the surface of the gold.

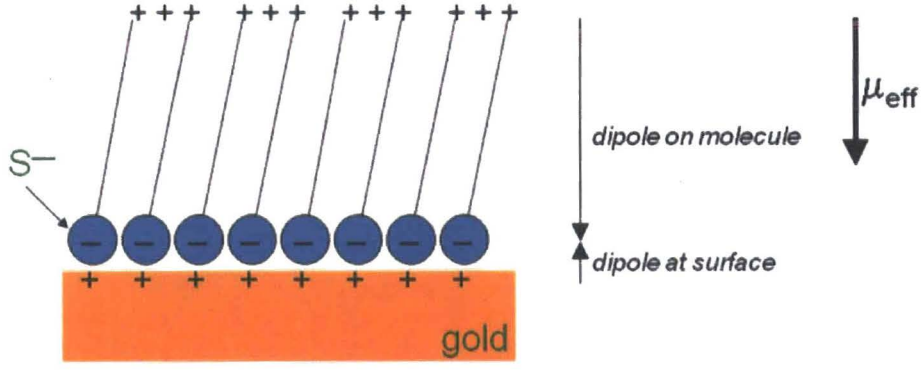

Figure 5.1.5.1. Diagram of the effective dipole, μ_{eff}, of an alkanethiol monolayer upon a gold substrate.

This corresponds to a drop in potential at the interface between the substrate and the monolayer, and can be therefore modelled as a Helmholtz double-layer.

$$eV_{CPD} = n \cdot \mu_{eff} / \varepsilon_0 \varepsilon \quad (1)$$

Where n is the electronic charge, μ_{eff} is the effective dipole of the system and ε_0 and ε are the permittivities of free space and the thiol monolayer.

Electrochemical impedance spectroscopy was also carried out, to provide a comparative study of the monolayers. Impedance spectroscopy has the ability to measure the capacitance value of a monolayer adsorbed onto the surface of a working electrode, and from that data, to calculate the depth of the monolayer, as well as its dielectric properties. As seen in section 1.1.5, the dielectric permittivity of a sample relates to the CPD value by the equation:

$$U = \frac{Q_d}{\varepsilon_{sample}} l \quad (2)$$

Where U is the voltage drop over the sample. Electrochemical impedance measurements should therefore be able to complement the contact-potential readings given by the SKN.

Standard, off-the-shelf thiol compounds were used for most of the experiments, as these compounds are well known and studied in literature.

An ethynylated aromatic compound, 4-((4-(biphenyl-4-ylethynyl)-2,5bis(hexyloxy)phenyl)ethynyl)benzenethiol, was synthesised and provided by the Bryce group at Durham University. This compound has a highly conjugated backbone, which allows electrons to pass readily down the chain[10]. This makes it of great interest as a molecular wire. This compound was subjected to the same experiments as the other compounds in order to quantify its conductive properties relative to the standard organothiol compounds.

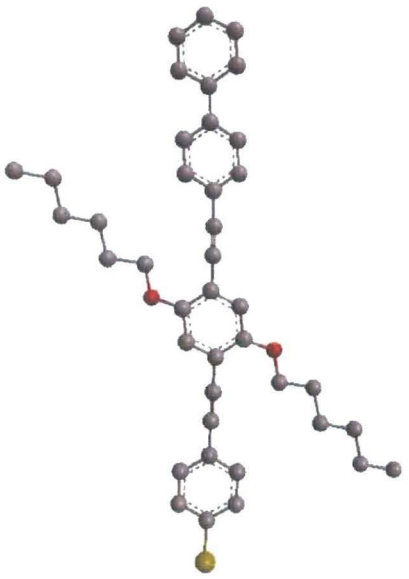

Figure 5.1.5.2. Computer model of 4-((4-(biphenyl-4-ylethynyl)-2,5bis(hexyloxy)phenyl)ethynyl)benzenethiol, showing the backbone of the molecule and the lateral chains, added to increase the solubility of the molecule. Provided by Francisco Aguiar, Durham University

5.1.6 Analytical Methods

5.1.6.1 Scanning Kelvin Nanoprobe microscopy

SKN microscopy was the principal analytical technique of this investigation, and was used to analyse all thiol-containing compounds used. The SKN, to our knowledge, has never been involved directly in a systematic study of simple compounds, having been mainly involved in the analysis of complex biomolecules[11] and semiconducting materials[12]. For this investigation, the SKN was set up in the same manner as in chapter 5.

5.1.6.2 Electrochemical impedance spectroscopy

Electrochemical impedance spectroscopy (EIS) is a rapidly developing electrochemical technique, able to investigate the capacitive changes occurring at

the surface of a working electrode. A basic overview of the theory behind the technique is given in section 2.3.1. EIS was used in this study to calculate the capacitive values of a series of organothiol monolayers adsorbed on a gold electrode surface.

5.1.8 Preparation concerns

The standard method of preparing self-assembled monolayers, as detailed above, is by immersing a substrate in a dilute solution of the monolayering compound. This approach will, however, not produce SAM substrates suitable for analysis with the SKN. This is due to the SKN's lack of a precise and constant baseline for measurement – the SKN does not measure the absolute work function, but rather the change in potential difference between the tip and the substrate. This value fluctuates somewhat, due to variations in the computer-controlled height positioning of the tip and the reduction of background noise. What can be measured accurately, however, is the variation in CPD value between an area of bare, uncovered substrate and an area covered with a monolayer.

This presents a problem when preparing a SAM, as there will be no areas of gold left uncovered using the traditional method. Covering an area with adhesive tape was dismissed as an approach, due to the residue left on the surface by the adhesive tape. Slanting the substrate so that a part was above the waterline was likewise dismissed, due to staining and excess deposition at the meniscus. Surfaces with patterns of covered and bare substrate offer the best contrast for the SKN, and several approaches were considered. The approaches are briefly summarised below, and their practical merits discussed in the experimental methods section below.

5.1.8.1 Solvent-drop evaporation

This simple method, used in chapter 4 for the deposition of phthalocyanines, was attempted for SAMs of thiols. A drop of organothiol in a dilute organic solution is deposited on a substrate and left in a humid atmosphere of the solvent until the drop evaporates, leaving the SAM behind[13]. This technique leaves characteristic 'crater' depositions, which need to be accounted for in scans.

5.1.8.2 Robotic microarraying

This method used a robotic contact printing array, identical to those used by biologists in DNA and protein microarray experiments, to prepare a patterned array of organothiols on a gold substrate. A robotic contact printing array consists of a printing head containing an arrangement of needles with heads on the μm scale, which are dipped into a solution and precisely positioned via computer to deliver an array of solvent spots on the substrate. This substrate is left to dry, with preparation times greatly faster than traditional solvent-drop evaporation due to the much smaller volumes required.

5.1.8.3 Soft lithography

This method used a polydimethylsiloxane (PDMS) stamp, firstly immersed in a dilute solution of organothiol in ethanol, to print arrays of SAMs onto gold substrates, as shown in figure 5.1.4.1. The stamps used had squares 200 by 200μm. This method has the advantages of speed and simplicity, but suffers from occasional incomplete transfer of organothiol, leading to monolayers of somewhat variable quality.

5.2 Experimental Details

5.2.1 Organothiols under investigation

A wide spectrum of organothiols were chosen for investigation, with samples taken from the most commonly used varieties of organothiol. Most groups seen in figure 5.1.3.1 were represented. All organothiols were sourced from Sigma-Aldrich, and were above 98% purity. When being prepared for monolayering, the compounds were dissolved in absolute ethanol at a concentration of $1x10^{-3}$ mol. Biological compounds were dissolved in purified water at the same concentration. The following sections contain lists of all the organothiols used in this investigation, subdivided into lists of alkanethiols, aromatic thiols and biological thiols.

5.2.1.1 List of alkanethiols

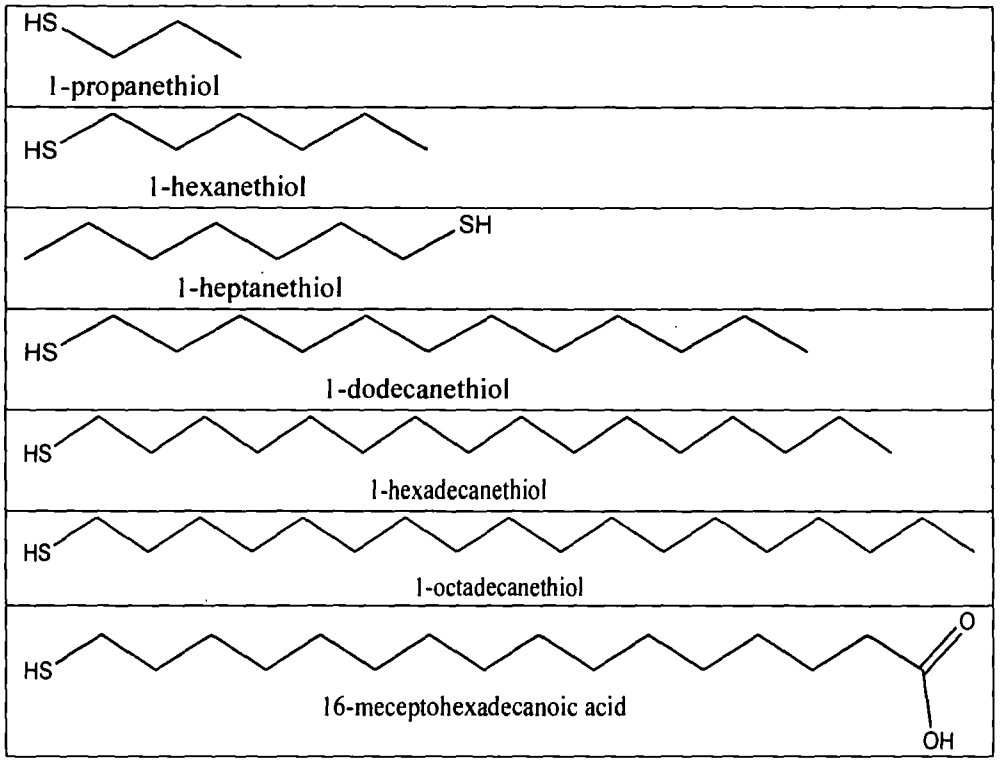

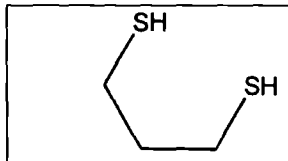

1,3-propanedithiol

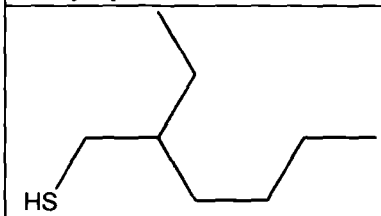

2-ethyl-1-hexanethiol

5.2.1.2 List of aromatic and cyclic thiols

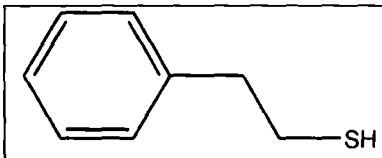

2-phenylethanethiol

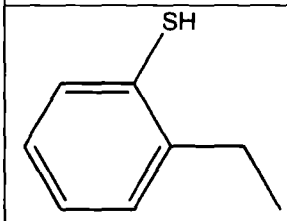

2-ethylbenzenethiol

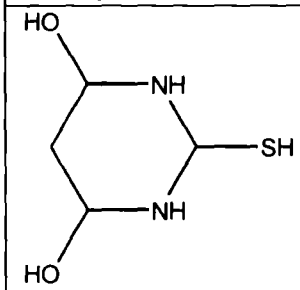

2-thiobarbituric acid

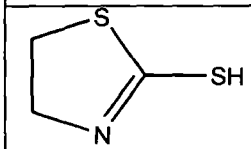

2-Thiazoline-2-thiol

5.2.1.3 List of biological thiols

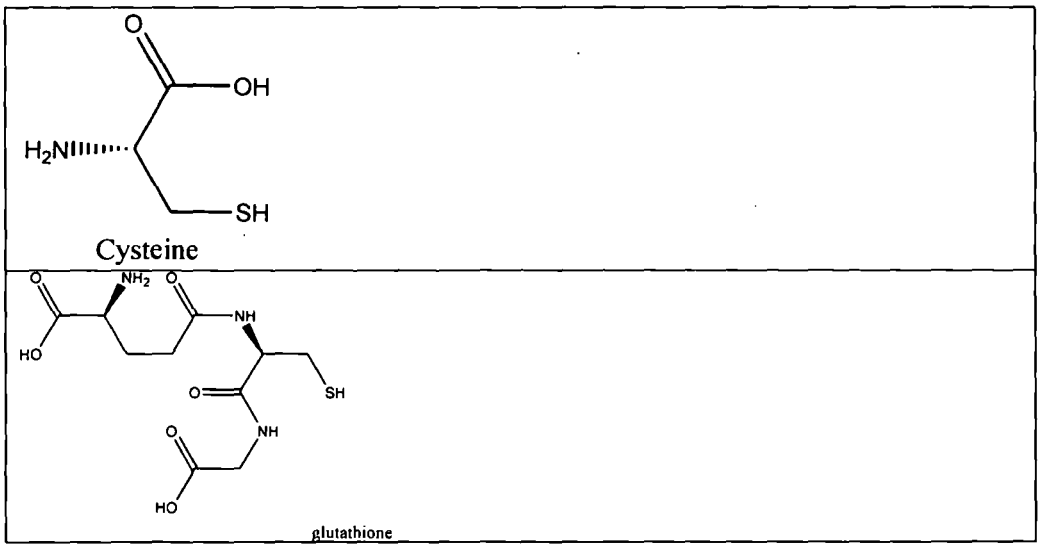

5.2.1.4 Molecular wire

4-((4-(biphenyl-4-ylethynyl)-2,5bis(hexyloxy)phenyl)ethynyl)benzenethiol, the molecular wire under investigation, was prepared by the Bryce group at Durham[10]. The molecule was provided in a solid powdered form. The thiol group was originally protected by a cyanoethyl group, which needed to be removed before use. To accomplish this, the powder was dissolved in dry THF, which was thoroughly degassed with N_2. A drop of tetrabutylammonium hydroxide-methanol was then added with vigourous shaking. This deprotected the thiol group, allowing the molecule to adsorb onto gold.

5.2.2 Substrate preparation

High-quality self-assembling monolayers will not form on a substrate unless that substrate is flat, highly cleaned and free from contaminants. Gold, being a soft metal, is readily contaminated by organic and inorganic species. Gold substrates were sourced from the Engineering Department of the University of Durham, where they were prepared by electron-beam physical vapour deposition. Standard glass microscope slides were ultrasonically cleaned before being placed in a deposition chamber, which is evacuated to a soft vacuum (~10^{-4}Torr). A film of 200Å of chromium followed by 1000Å of gold was then deposited onto the surface by vapour deposition. This process involves using an electron beam to heat a block of solid material until some evaporates. This gaseous material is then funnelled onto the substrate, causing a thin film of the material to form. Chronium is filmed before gold to provide a strong base for the gold deposition, increasing the resistance of the film to scratching and chipping.

Before use, the gold substrates were sonicated for twenty minutes in ethanol to remove surface dust and contaminants. They were then washed with ethanol, methanol and acetone before being dried under nitrogen and stored in a protective atmosphere until use.

5.2.3 Self-assembling monolayer preparation

As stated above in section 5.1.8, the organothiols needed to be monolayered in such a way that there are regions of bare substrate, due to the need to measure the change in contact-potential difference between bare and covered gold. Three methods were tested in order to accomplish this goal – solvent-drop evaporation, robotic microarraying and soft lithography using PDMS stamps. The results are summarised below.

For SAMs prepared onto gold working electrodes, (BASi MF-2014) the electrode was firstly sonicated in ethanol and cleaned with diamond slurry, before being dried

under a stream of nitrogen. The electrode was then immersed in a stoppered test-tube of 1mMorganothiol in ethanol and left overnight.

5.2.3.1 Solvent-drop evaporation

The solvent-drop evaporation method was attempted with two $1x10^{-3}$M solutions of dodecane and hexadecane thiol in ethanol. Two 3µl drops were deposited by a 100µl capacity Gibson micropipette in the vicinity of each other on a cleaned gold substrate, and were left overnight in a humid ethanol atmosphere. The substrate was then scanned by the SKN and the following image was obtained:

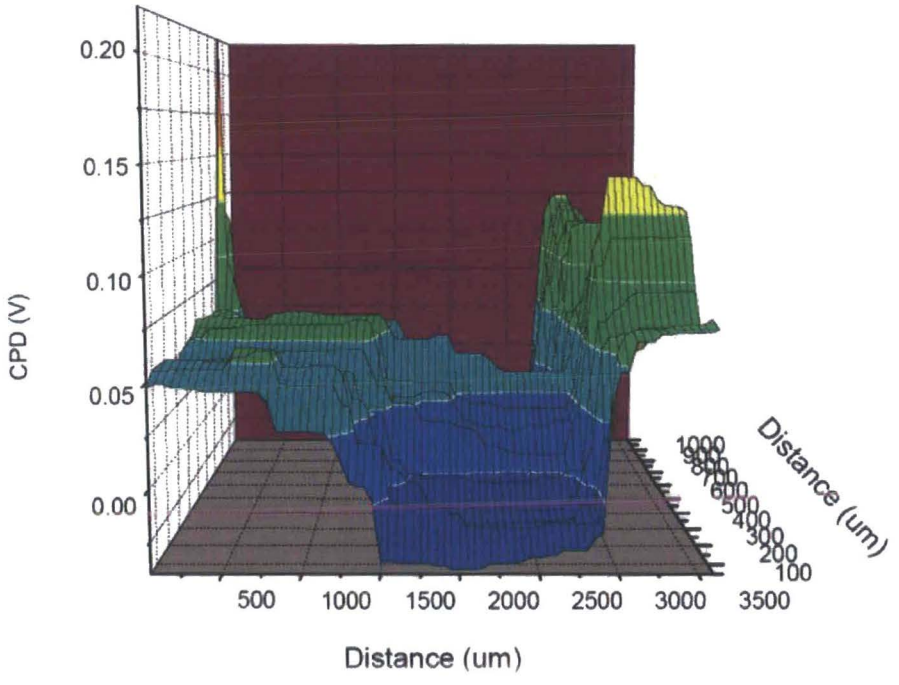

Figure 5.2.3.1.1 SKN scan of an area of gold substrate, showing areas covered by dodecanethiol (left) and hexadecanethiol (right)

This image clearly shows a difference in the work function between the area of bare gold (middle) and the two thiol coverings. A difference of approx 0.05V was observed for dodecanethiol and a difference of approx 0.08V for hexadecanethiol. However, the image shows both considerable variance and, more worryingly,

contaminination of the bare gold with material from both sides, making the contrast between the bare and covered areas of the gold difficult to determine. Cratering effects, where the concentration of material was clearly greater at the edges of the drop then the centre, were noticed on the drops when examined under optical microscope. This suggests that SKN scans, of necessity carried out only on a small portion of the drop, would prove inaccurate.

Due to these concerns, the solvent-drop evaporation method was not deemed suitable to use for the investigation.

5.2.3.2. Robotic microarraying

Robotic microarraying was carried out using a Genetix Systems Qarray microarrayer situated in the Biology Department of the University of Durham. Samples of $1x10^{-3}$M solvated hexadecanethiol in ethanol were prepared and placed into each well of a 96-well plate. A standard 24-pin head with 50μm tip diameters was used to print arrays of solution onto a gold-coated microscope slide using a standard 24-drop print scheme. This method was hoped, by the tightly-controlled printing method and very small quantities of material, to avoid the difficulties of cratering and unevenness that occurred with larger-scale solvent dropping.

This method encountered severe difficulties when monolayering thiols, as an atmosphere of ethanol could not be placed around the evaporating drops to control the speed of evaporation, and the time taken by the arrayer to print the entire slide, in excess of an hour, meant that the slide could not immediately be transferred to a protective environment. This led to extremely miniscule quantities of material being deposited, and attempts to scan the area with the SKN proved unsuccessful. As the microarraying room was not ventilated, higher concentrations of thiols could not be tried due to the stench that would occur.

This method proved, however, extremely successful with biomolecules such as glutathione and cysteine. Water proved a more durable solvent then ethanol,

allowing the molecules time to organise. This led to easily measurable microarrays, with spots visible by the naked eye. When viewed under an optical microscope, crystalline aggregations could be seen. These, combined with the large CPD differences observed (~0.4V as compared to observed value of less than 0.1V for a monolayered material) suggest that crystalline aggregations instead of self-assembled monolayers are forming via the evaporation process.

Due to the issues involved with obtaining monolayered material, the decision was taken not to use the robotic microarraying techniques further in the investigation.

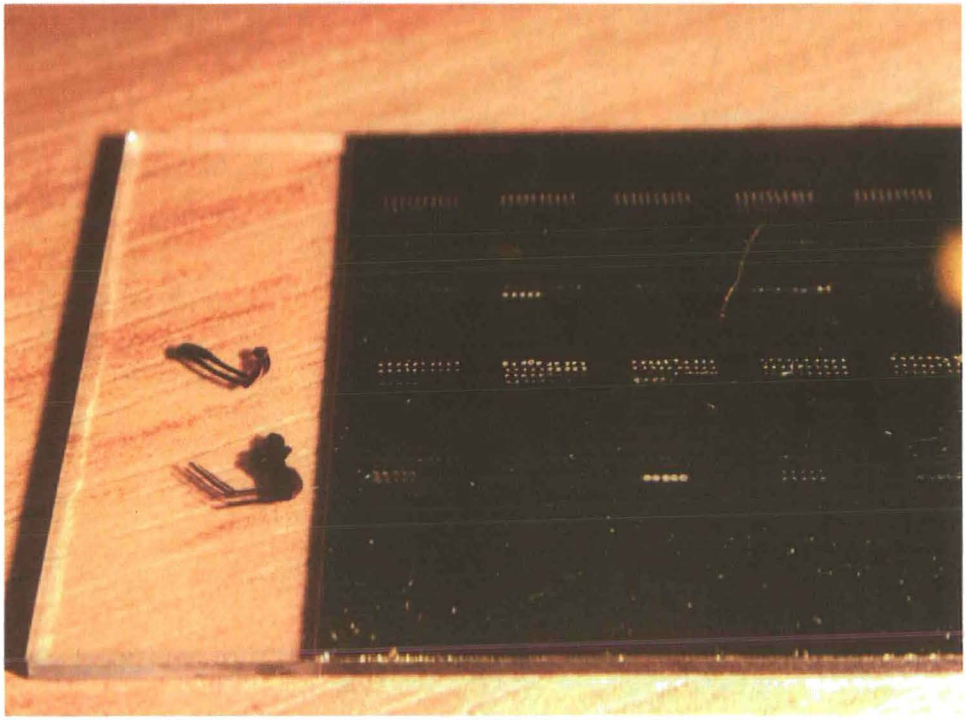

Figure 5.2.3.2.1. Photograph of cysteine robotically printed onto a gold-covered microarray slide.

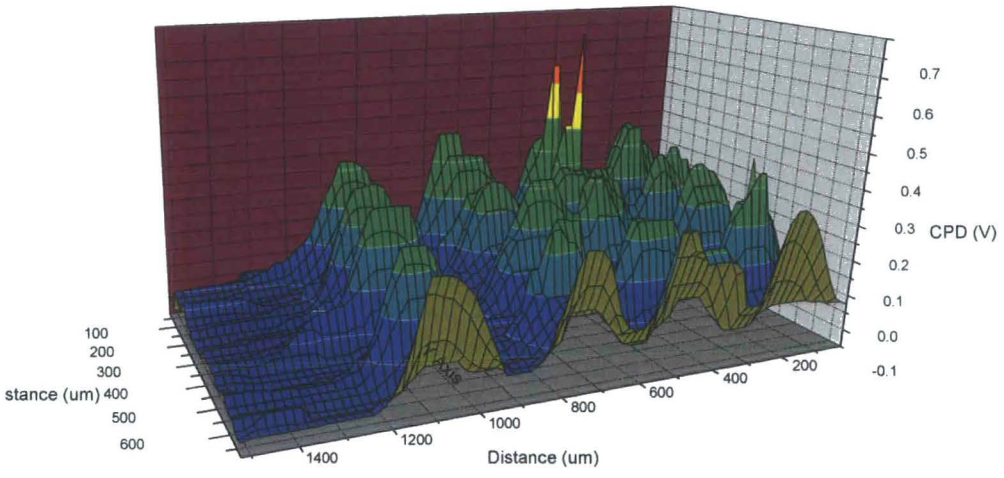

Figure 5.2.3.2.2. CPD scan of a portion of the cysteine array shown in figure 5.2.3.2.1.

5.2.3.3. Soft lithography

Arrayed grids of organothiols were microcontact printed upon gold surfaces using a PDMS stamp, as described in section 5.1.4. PDMS stamps were sourced from Platypus Technologies Ltd, and had a printing surface consisting of a grid of square 200μm raised areas. Before printing, the PDMS stamp was sonicated, washed with ethanol and then dried. The PDMS stamp was then immersed with the printing face pointing upwards into a $1x10^{-3}$M ethanol solution of the thiol compound to be arrayed. Water was used as the solvent for cysteine and glutathione, due to these molecules being unable to readily dissolve in organic solvents. (See chapter 3). The solution was covered and left for two hours, after which the stamp was removed from the solution, washed with ethanol and dried under a stream of nitrogen. The stamp was then placed, printing face down, onto the surface of a clean gold substrate and gently pressed down for 20 seconds to enable the transfer of the monolayer. The stamp was then lifted and cleaned.

As a test, a hexadecanethiol monolayer array was printed. This was then scanned by the SKN. The ΔCPD between the uncovered and covered areas of gold was found to

be approximately 0.08V, a result congruent with other monolayers such as the phthalocyanine derivatives in chapter 4. The grid spots were well-defined,

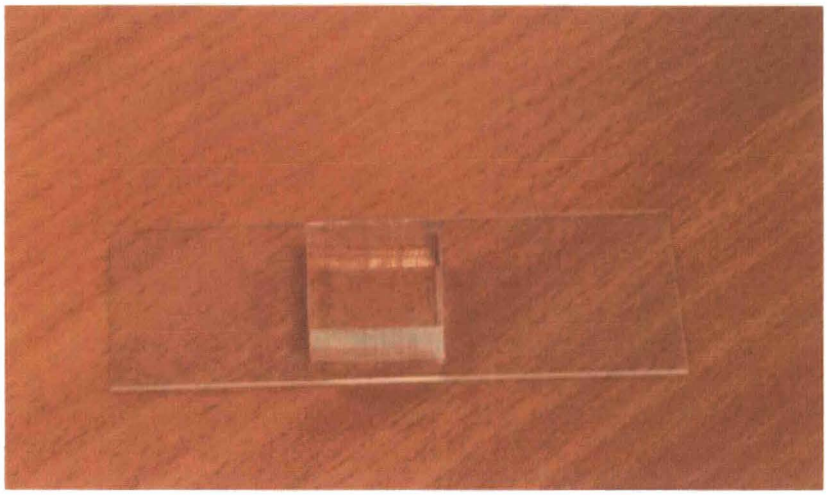

Figure 5.2.3.3.1. Photograph of 200um grid PDMS stamp.

Figure 5.2.3.3.2. Optical microscope image of PDMS stamp printing surface, showing the 200μm square raised features.

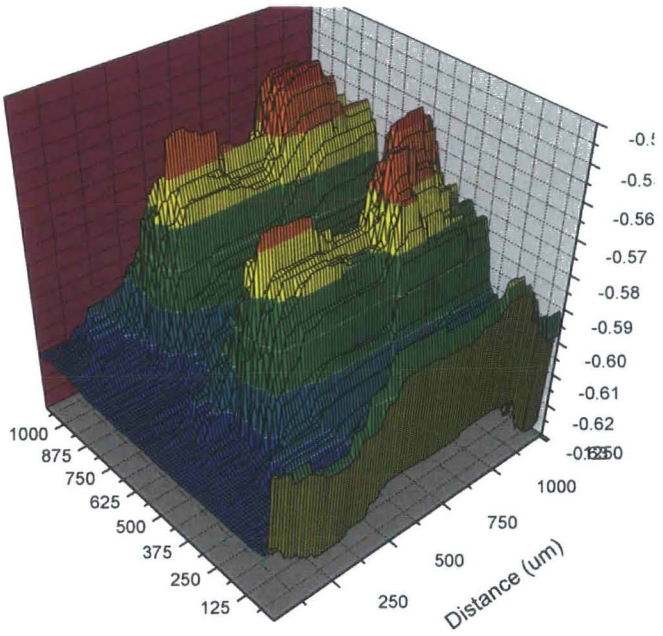

Figure 5.2.3.3.3. SKN scan of a portion of hexadecanethiol grid on gold substrate, printed by soft lithography.

Soft lithography could produce patterned monolayers on a gold substrate quickly and relatively easily. The monolayers were of generally good quality, though sometimes several prints needed to be taken to ensure an even monolayer deposition. This method was capable of producing the best results of the three studied, and was therefore chosen for the investigation.

The PDMS stamp reacted badly with the THF used as a solvent for the molecular wire. Because of this, the molecular wire was deposited using the solvent-drop method.

5.2.4. Scanning Kelvin Nanoprobe Microscopy

SKN measurements were carried out in an identical manner to section 4.2.2. Experiments were carried out in standard laboratory conditions. The SKN was protected inside an enclosed Perspex box to minimise air movements and

vibrations. Scans were usually taken of a 2x2mm square area at a resolution of 25μm, though occasionally these conditions were altered to encompass larger areas or scan smaller area with more detail.

Due to a slightly misaligned tip holder, the distance between the tip and the table would occasionally exceed the specified bounds resulting in an error and the termination of the scan. This has no effect on the quality of the points already taken, and due to the length of time of a detailed SKN scan, it was decided not to repeat scans where useful data had been collected. Some scans below may therefore appear incomplete.

5.2.5 Electrochemical Impedance Spectroscopy

Electrochemical Impedance Spectroscopy (EIS) experiments were carried out on a Solartron 1260A frequency response analyser, interfaced to a Princeton Applied Research PAR 283 potentiostat. A monolayer was prepared on a BASi MF-2014 gold working electrode as described in section 5.2.3. The working electrode was placed in a standard 3-electrode electrochemical cell with a 1cm 2 platinum counter electrode prepared by the departmental glassblowers and a BASi MF-2078 Ag/AgCl reference electrode. The electrochemical cell contained 1mM $Fe(CN)_6^{3-/4-}$ in equal concentrations in 0.1M KNO_3. The cell was placed inside a Farady cage to minimise background interference. Measurements were carried out at room temperature, using solutions purged of oxygen by argon-bubbling for 10 minutes. The frequency response analyser and potentiostat were interfaced to a standard PC running Microsoft windows using an IEEE 488.2 by the Solarton Zplot software, and analysed by the attached Zview package. Scans were taken using an a.c signal of 10Hz magnitude between the 100,000 Hz to 0.1Hz frequencies.

Supporting cyclic voltammetry measurements were carried out in the same electrochemical cell and solution, using the PAR 283 potentiostat in a voltage window of -0.5V to +0.8V and a scan rate of 100mV/s.

5.3 Results and Discussion

5.3.1 Scanning Kelvin Probe Microscopy

Contact-potential difference scans of 200μm-sized printed grids of the organothiols listed in 5.2.1.1 were taken using the SKN. The data from these scans was loaded into Originlab, a graphing and data analysis software package. 3D heightmap-surface images were constructed from the data to give a topographical overview of the CPD variations of the scanned surface. To get an average ΔCPD between the gold substrate and the covering monolayer, three lines of data was chosen that went through both a clean area and the middle of a deposition. The baseline of the clean gold was then subtracted from the resulting graphs, and the data smoothed by a 5-point Fast Fourier Transform (FFT) method to remove spikes from the data set.

The SKN tip was assumed to have flattened to a width greater then 25μm, so the highest point on the smoothed graphs was then averaged and chosen to represent the ΔCPD of the monolayer. An example using 1-hexanethiol is shown below.

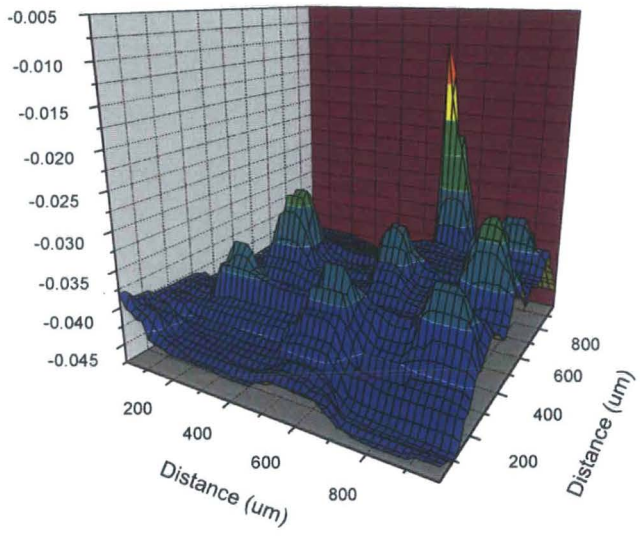

Figure 5.3.1.0.1. 3D surface image of a printed grid of 1-hexanethiol. The large spike is an abnormality caused by surface contamination.

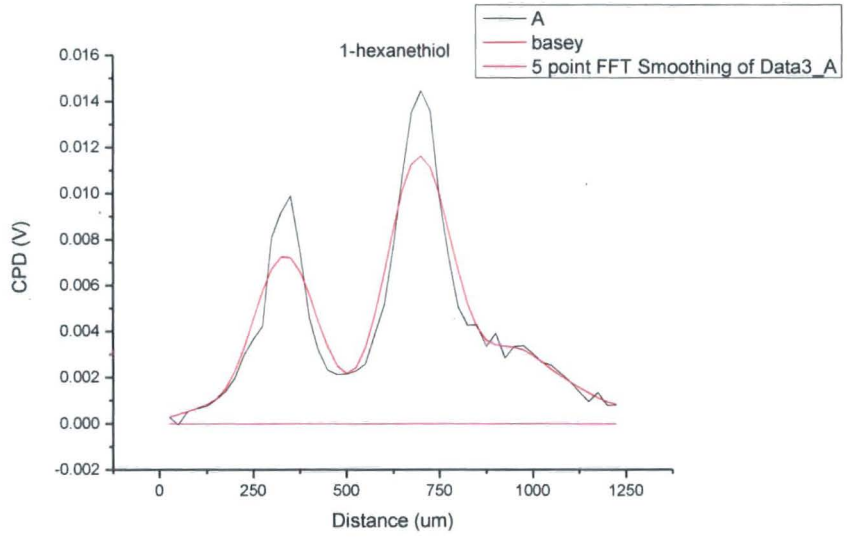

Figure 5.3.1.0.2. Line graph of a printed grid of 1-hexadecanethiol. The black line is the raw data; the red line is the smoothed data.

5.3.1.1 Results

Results are presented in a per-page format, with each page containing a molecular diagram of the organothiol, as well as the CPD values from the scan presented in a 3D topographical view. A line graph of the data line chosen to represent the average values is shown with the FFT smoothed line in red.

5.3.1.1.1. Alkanethiols

5.3.1.1.1.1. 1-propanethiol

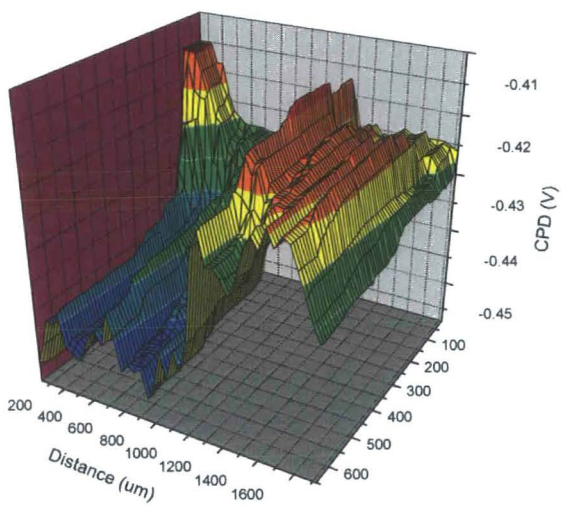

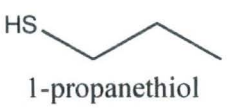

1-propanethiol

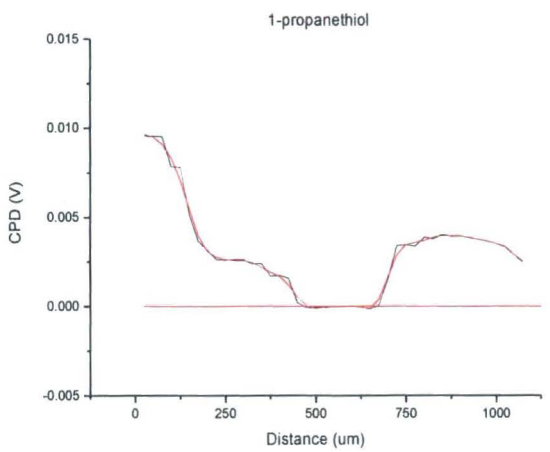

ΔCPD = 0.0097

5.3.1.1.1.2. 1-hexanethiol

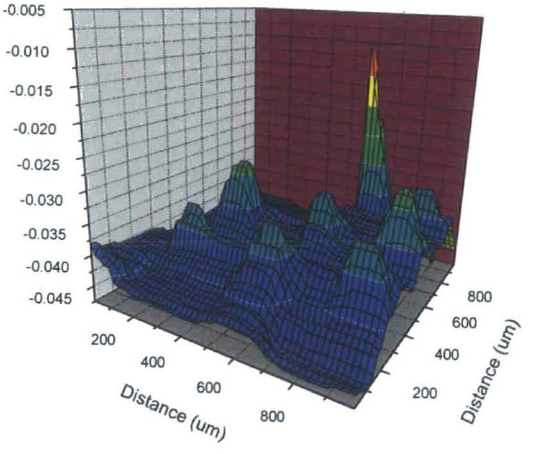

1-hexanethiol

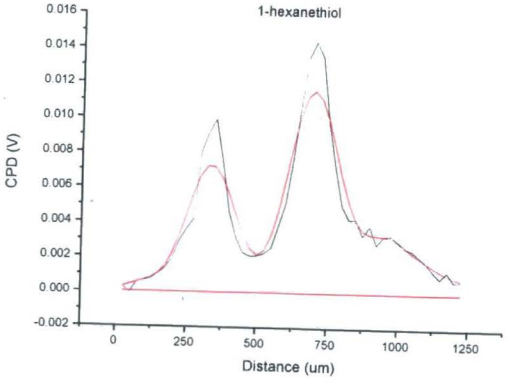

ΔCPD = 0.0118

5.3.1.1.1.3. 1-heptanethiol

1-heptanethiol

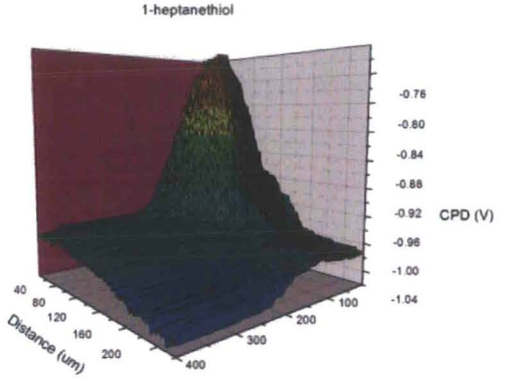

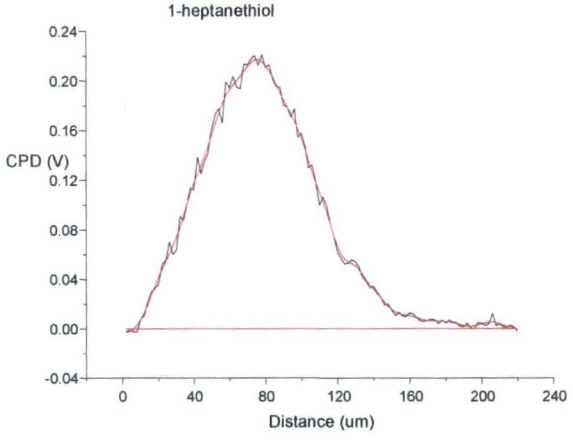

ΔCPD = 0.022

5.3.1.1.1.4. 1-dodecanethiol

1-dodecanethiol

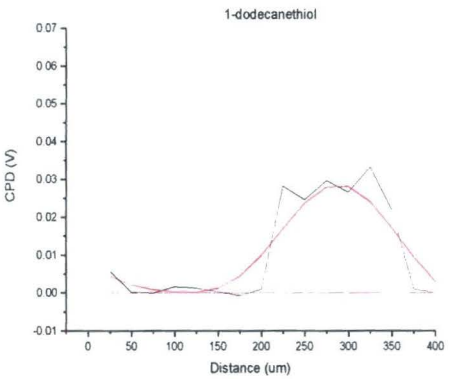

ΔCPD = 0.029

5.3.1.1.1.5 1-hexadecanethiol

1-hexadecanethiol

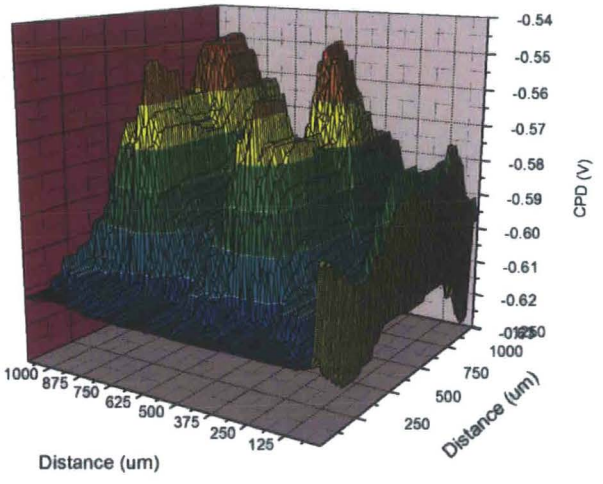

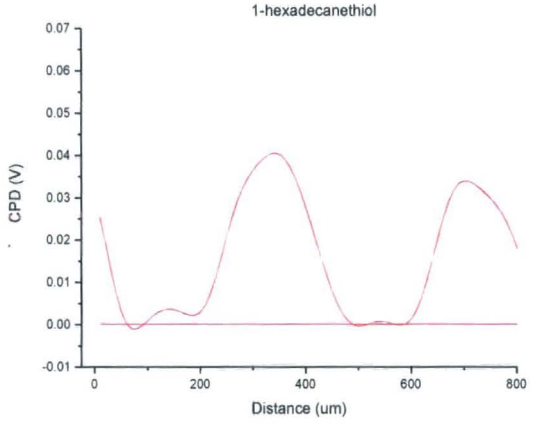

ΔCPD=0.041

5.3.1.1.1.6. 1-octadecanethiol

1-octadecanethiol

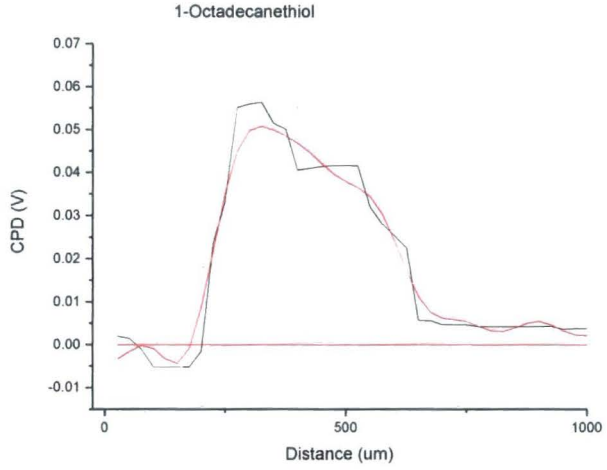

ΔCPD=0.050

5.3.1.1.1.7. 16-merceptohexadeconic acid

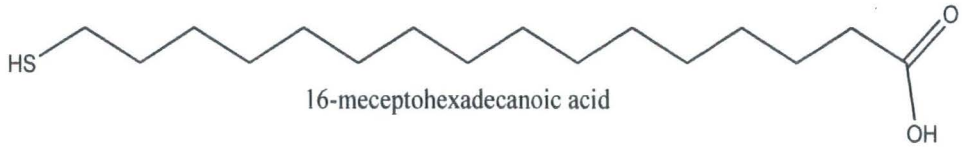

16-meceptohexadecanoic acid

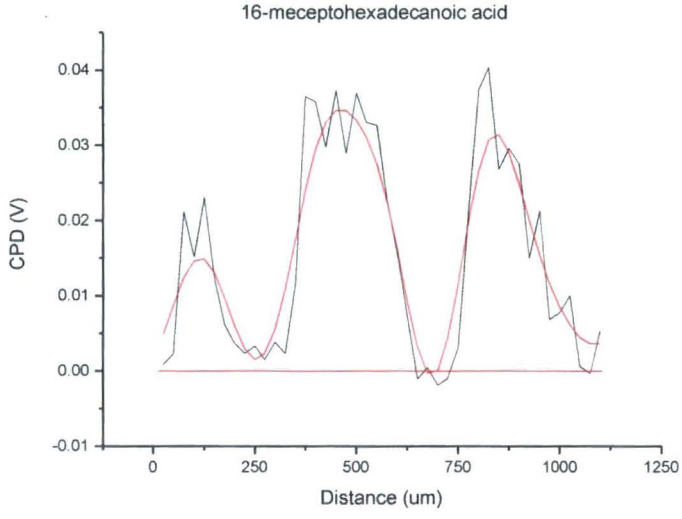

ΔCPD=0.035

5.3.1.1.1.8. 1,3-propanedithiol

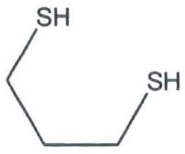

1,3-propanedithiol

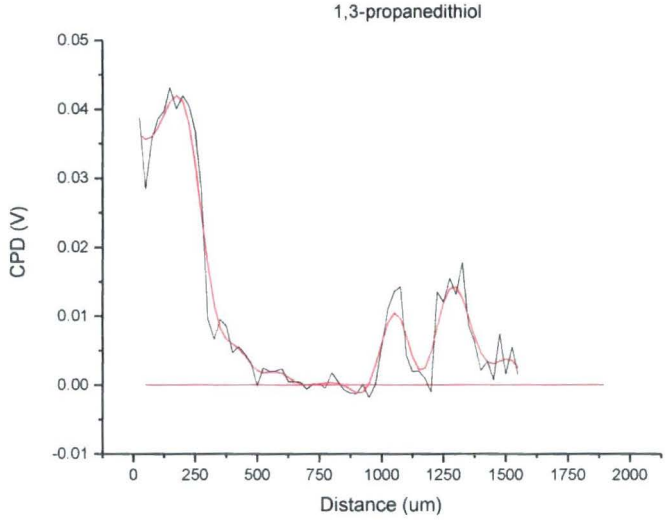

ΔCPD = 0.012 and 0.042

5.3.1.1.9. 2-ethyl-1-hexanethiol

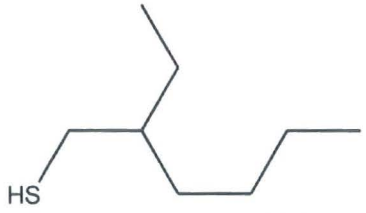

2-ethyl-1-hexanethiol

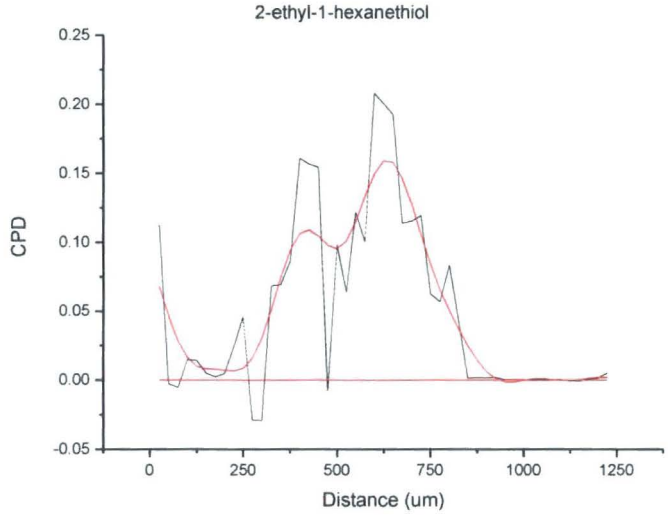

ΔCPD=0.154

5.3.1.1.2. Aromatic and cyclic thiols

5.3.1.1.2.1. 2-Phenylethanethiol

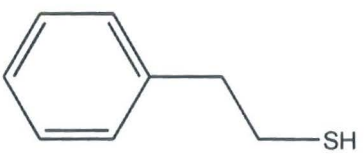

2-phenylethanethiol

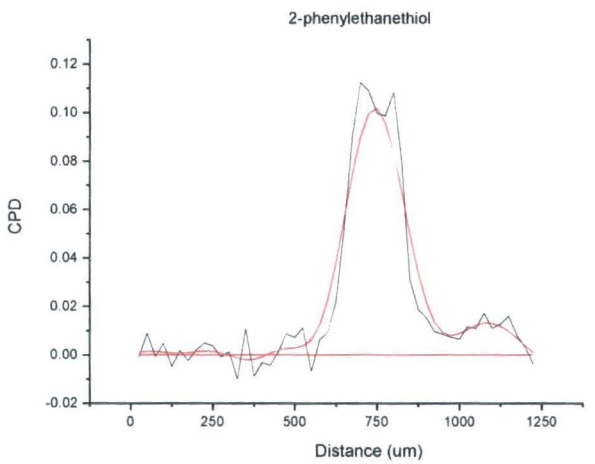

ΔCPD=0.010

5.3.1.1.2.2. 2-ethylbenzenethiol

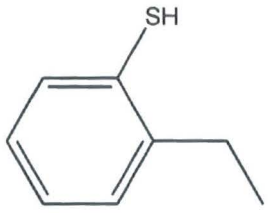

2-ethylbenzenethiol

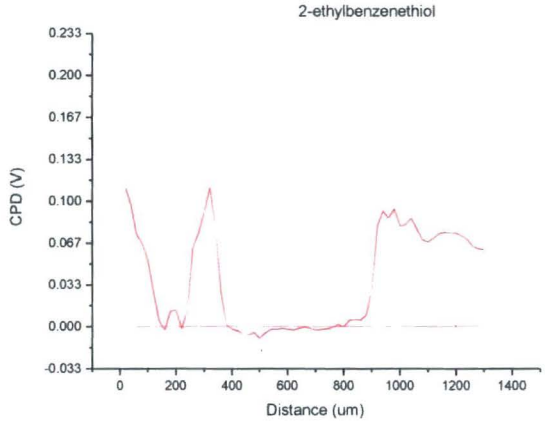

ΔCPD=0.094

5.3.1.1.2.3. 2-thiobarbituric acid

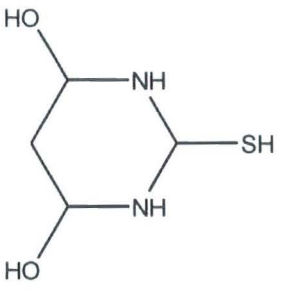

2-thiobarbituric acid

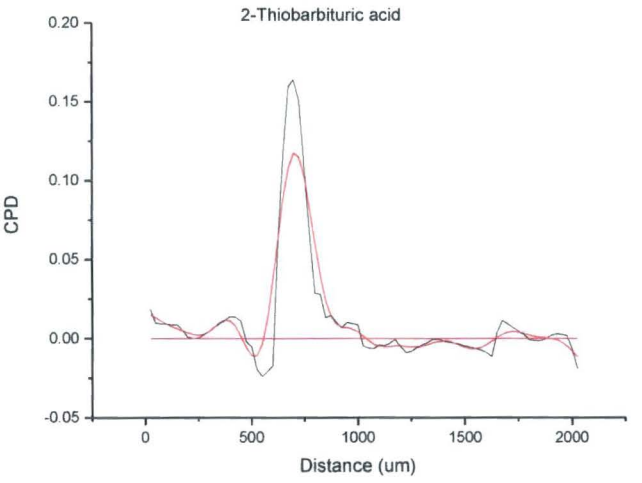

ΔCPD= 0.12

5.3.1.1.2.4. 2-thiazoline-2-thiol

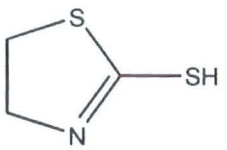

2-Thiazoline-2-thiol

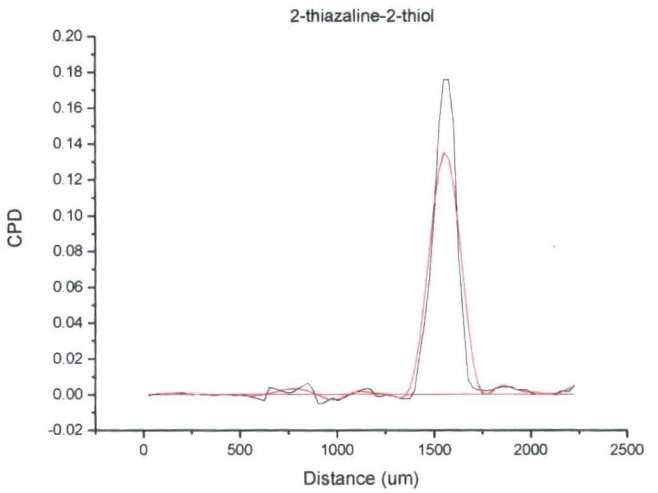

ΔCPD=0.14

5.3.1.1.3 Biological thiols

5.3.1.1.3.1. Cysteine

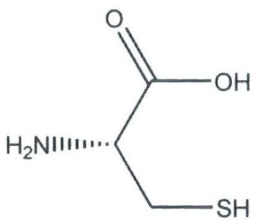

Cysteine

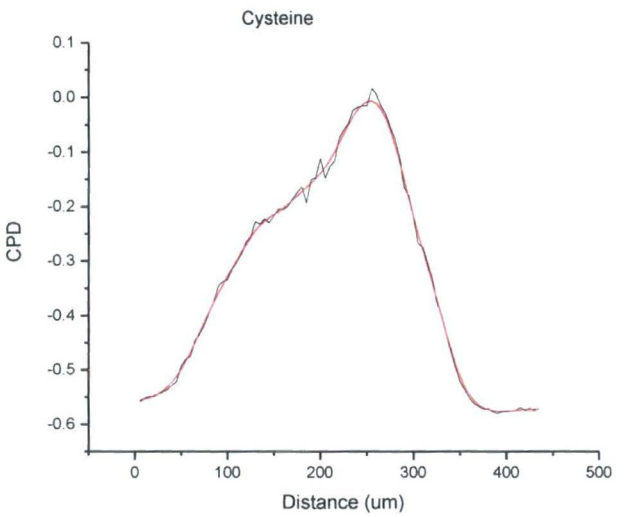

ΔCPD=0.55

5.3.1.1.3.2 Glutathione

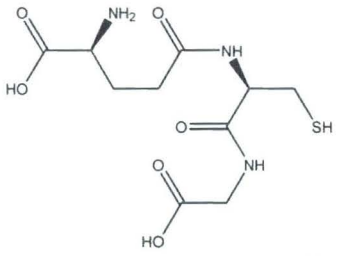

glutathione

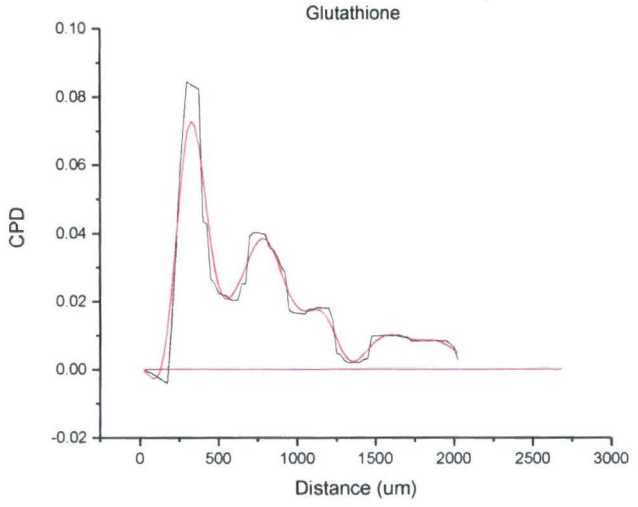

ΔCPD=0.07

5.3.1.1.4 Molecular Wire

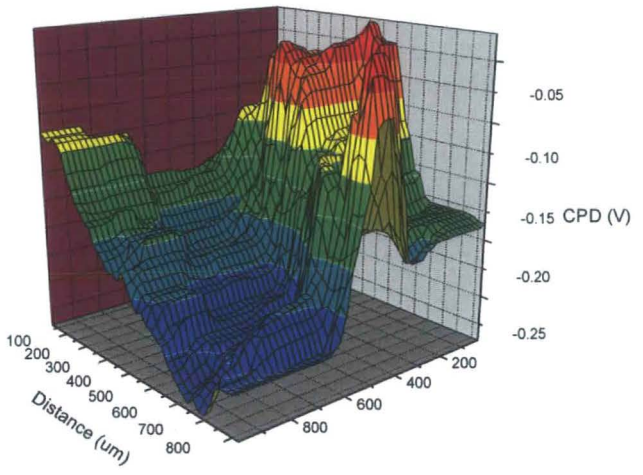

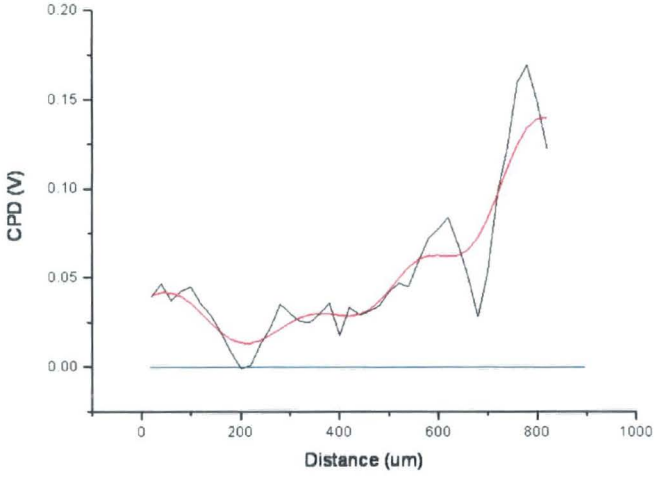

ΔCPD=0.143

Table 5.3.1.1.5. Table of SKN results

Compound	**ΔCPD**
Alkanethiols	
1-propanethiol	**0.0097**
1-hexanethiol	**0.012**
1-heptanethiol	**0.022**
1-dodecanethiol	**0.029**
1-hexadecanethiol	**0.041**
1-octadecanethiol	**0.050**
16-merceptohexadeconic acid	**0.035**
1,3-propanedithiol	**0.012 and 0.042**
2-ethyl-1-hexanethiol	**0.154**
Aromatic and cyclic thiols	
2-phenylethanethiol	**0.110**
2-ethylbenzenethiol	**0.033**
2-thiobarbituric acid	**0.121**
2-thiazoline-2-thiol	**0.140**
Biological thiols	
Cysteine	**0.552**
Glutathione	**0.072**
Molecular wire	**0.143**

5.3.1.2 Discussion

5.3.1.2.1. Alkanethiol results

The results of the alkanethiol SKN scans show some interesting trends.

The ΔCPD values increase in a roughly linear fashion from propanethiol, with its small modification of 0.0097 to octadecanethiol with its larger modification of 0.05. Due to the nature of the SKN measurements, as well as the method of obtaining the average ΔCPD value an error of some magnitude can be assumed on the results. This was selected as the standard deviation of the data set, or ±0.05V. A graph was plotted of ΔCPD against the chain length of the alkane molecule, and a trend line was added.

The error was assumed to be larger as a percentage of the smaller alkanethiols, due to the greater difficulties in accuracy at that scale. The scans of propanethiol had to be repeated several times to obtain an accurate figure, and ethanethiol proved impossible to measure coherently with the SKN, due to limitations of the lateral resolution.

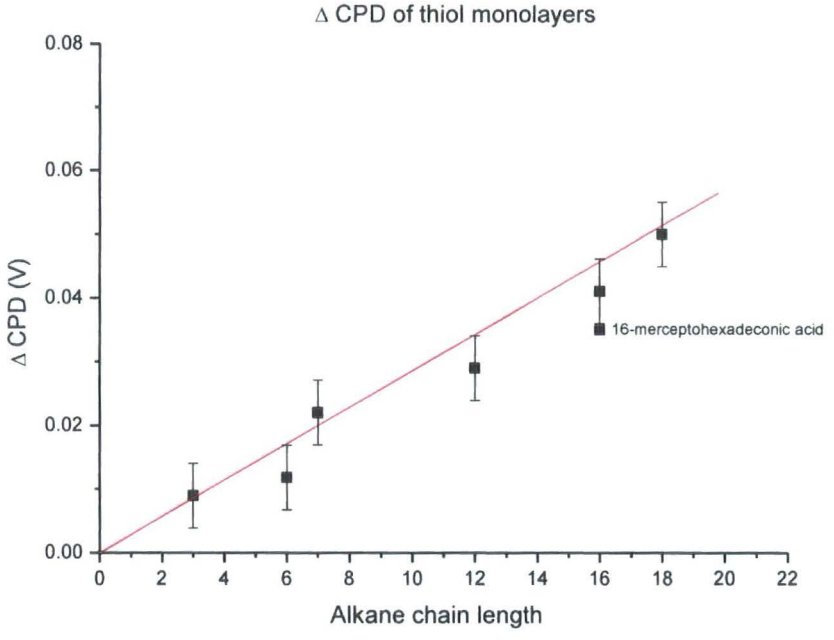

FiFigu

re 5.3.1.2.1.1. Graph showing the ΔCPD values of alkanethiol monolayers against the alkane chain length.

As can be seen, the values while corresponding to a rough linear progression, are somewhat scattered, with some only just within the margin of error. Nevertheless, it is possible using the trendline to calculate the ΔCPD caused by the addition of a $-CH_2-$ group. This works out to be approximately 0.0029V per moiety.

16-merceptohexadeconic acid, as can be seen from the graph, possesses a significantly lower ΔCPD then hexadecanethiol. This is almost certainly due to the polar carboxylic acid surface group, which modifies the dipole moment of the monolayer. This alters the voltage drop across the layer compared to hexadecanethiol, which is non-polar. In this way, the SKN can differentiate between functionalised and non-functionalised monolayers and theoretically between different functionalities, though there were no other functionalised 1-hexadecanethiol molecules easily available to test.

Two other molecules were also tested – a branched alkanethiol and an alkanedithiol, to assess structural effects on the SKN scans.

The case of 1,3-propanedithiol is an interesting one. Scans of a monolayered surface revealed small areas of dramatically differing discrete ΔCPD values, of 0.012 and 0.042V. This was originally written off as a problem with the SAM application or the scan, but the proximity of the first value to the measured value of 1-propanethiol suggested that the two values corresponded to either one or both of the thiol groups attaching to the gold. With both thiol groups attached, the propane molecules bend in a bow shape across the substrate, leading to a sharp jump upward in the ΔCPD value. Another explanation could be that multilayers are being formed in certain areas through S-S bonds. A greater variation in values would however be expected if this were the case.

Another surprise in the results is the value for 2-ethyl-1-hexanethiol. This value, 0.154V was extremely high compared to the other alkanethiols values, which ranged in the 0.01-0.05V area. The values were also inconsistent over repeated scans – showing great variation and the absence of large single peaks seen for the other alkanethiols. This suggests that the branched structure of 2-ethyl-1-hexanethiol is preventing the molecule forming good quality monolayers through steric hindrance. The ethyl branch will rotate freely around the central axis, preventing strong Van der Waals interactions between the chains. This will lead to randomly-constructed monolayers with significant pinholes and uncovered areas. The extremely high values shown also suggest the presence of a degree of crystallisation and of multi-layer structures with molecules caught between the branches.

5.3.1.2.2 Aromatic and cyclic thiol results

All the ΔCPD values for the aromatic and cyclic thiols were considerably greater than those for the straight-chain alkanethiols. This suggests that either the aromatic thiols did not form good quality monolayers like the straight-chain thiols or that the

aromatic rings are somehow inhibiting conductivity to a greater scale then the straight-chain molecules. As 2-ethyl-1-hexanethiol also exhibited a far greater ΔCPD then would necessarily be expected from its size, it would suggest that molecular organisation on the surface is a significant determinant of the ΔCPD – a disordered monolayer will have a very different dipole moment to an ordered one. The graph from 5.3.1.2.1.1 is below, updated with the values for the aromatic thiols.

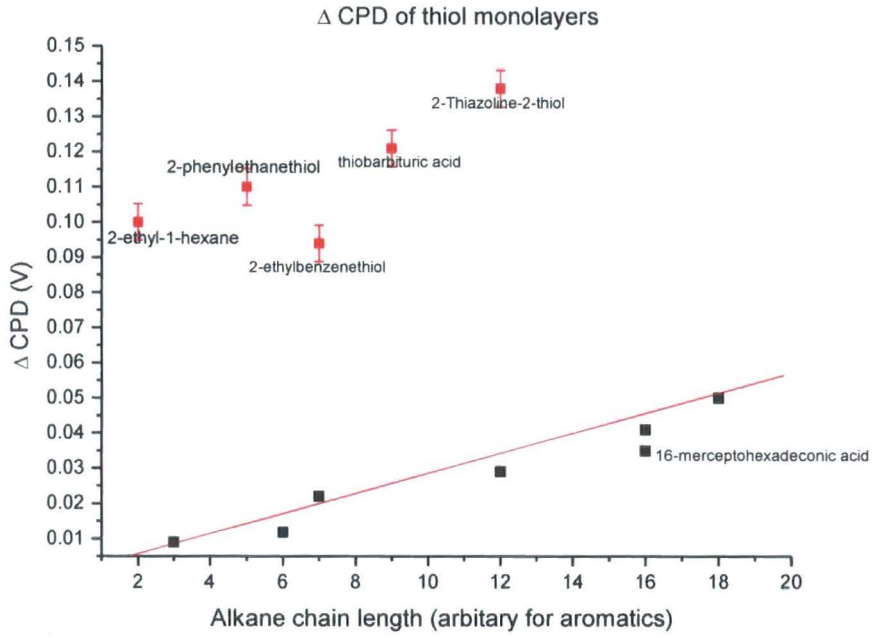

Figure 5.3.1.2.2.1. Graph showing the ΔCPD values of alkanethiols and aromatic monolayers.

Note that the x-axis position is irrelevant in this graph, as the aromatic thiols do not have simple alkane chain lengths.

2-ethylbenzenethiol and 2-phenylethanethiol are similar molecules, with both having a phenyl group connected to a –SH group. The lowest ΔCPD value is 2-ethylbenzenethiol, with a value of 0.094. 2-phenylethanethiol has a slightly higher value of 0.110, perhaps relating to the ethane moiety separating the phenyl ring from the thiol group. 2-ethylbenzenethiol exhibited some of the same irregular surface features shown with 2-ethyl-1-hexanethiol, whereas 2-phenylethanethol

showed pronounced peaks similar to the alkanethiol scans. This would seem to suggest that 2-ethylbenzenethiol, with its branched ethyl chain, encountered some of the same packing difficulties seen with 2-ethyl-1-hexanethiol. 2-phenylethanethiol exhibited a peak structure, but one very much greater in magnitude to the alkanethiols. One possible explanation is that π-π interactions could be coming into play, allowing multiple layers of phenyl rings to slip on top of one another, held strongly enough to survive the post-deposition washing. As the phenyl rings are unlikely to be lying flat on the surface, due to the short length of the ethyl tether, the interactions would not allow stable stacks of rings similar to those found with phthalocyanine compounds, but rather stable interactions with neighbouring adsorbed compounds.

Thiobarbituric acid and 2-thiazoline-2-thiol have extremely high values for monolayered compounds. As they are non-aromatic compounds, π-π interactions cannot account for the extra values.

5.3.1.2.3. Biological thiols

Two biological thiols were tested, the amino acid cysteine, in the L-configuration, and the tripeptide L-glutathione. These provided radically different results. Cysteine had by far the largest ΔCPD result shown in the study, at 0.552V. This result was an order of magnitude higher than 1-octadecanethiol. This, combined with the results from the earlier studies of cysteine using the robotic microarrayer, suggest cysteine readily forms large crystalline structures when deposited. Optical microscopy revealed small crystalline deposits on the substrate. Glutathione had a far lower ΔCPD value of 0.072, which, although higher then 1-octadecanethiol, was still of a small enough magnitude to represent a self-assembling monolayer. Glutathione, due to its large branching structure, will form loosely-packed monolayers, as the intermolecular interactions will not be as strong as a straight-chain molecule, explaining the greater ΔCPD value.

5.3.1.2.4 Molecular wire

The molecular wire recorded a maximum ΔCPD value of 0.143V, considerably higher than the values recorded for the linear thiols. This was at odds with expectations, as it was assumed that the greater conductivity of the molecular wire would lead to a smaller change in ΔCPD compared with a large alkanethiol. Instead, the value was significantly greater. This suggests that the monolayer formed was looser-packed then a linear alkanethiol SAM, owing to the long side chains of the molecular wire preventing close-packing. The poor quality of the monolayer is confirmed by impedance results (section 5.3.2.5). This leads to the interesting conclusion that ΔCPD values seem to depend more on the assembly of a monolayer then the properties of the invidvidual compounds in the monolayer.

5.3.1.3 Conclusions

The scanning Kelvin nanoprobe has shown that it is possible to distinguish between different thiolic monolayers with excellent precision. Straight-chain alkanethiols followed a standard linear pattern, with an average ΔCPD value of an $-CH_2-$ moiety being 0.0029. Functionalisation at the end of the alkane chain appears to have an effect on the ΔCPD value, lowering it when the functional group added is a polar one. Dithiols appear to have two discrete values, either caused by areas of either one or both of the thiol groups attaching, or by multilayers formed by S-S bonds. Branched alkanethiols, as well as aromatic and cyclic thiol compounds, have far greater ΔCPD values than straight-chain thiol compounds. This appears to be due to the monolayer composition – jumbled monolayers seem to be poorer conductors then ordered monolayers, and thus lead to a more non-conducting CPD value. This observation seems to apply also to the aromatic and cyclic thiol monolayers, as well as the molecular wire studied, which all exhibit far larger ΔCPD values then the straight-chain alkanethiols. From these observations, it seems that monolayer organisation is an extremely important factor in determining the magnitude of the CPD change, as much if not more than the physical depth of the monolayer.

There are some problems with these measurements, both in accuracy and in the variety of thiols used. Though an effort was made to use examples of many kinds of organothiols, in some cases, such as dithiolic compounds and end-functionalised compounds, only one example was found that correlated in chain length with an already acquired alkanethiol. This means that the characteristics noted for these molecules may not be replicated in others. This was an issue because of the necessity of finding easily available and cheap thiol compounds, and is something that should be corrected in future investigations. The accuracy of the SKN, as well as the method used to calculate the average ΔCPD for a monolayer was also somewhat of an issue. SKN tips tended to flatten, and therefore lose precision, quicker than was expected. This led to decreases in accuracy as well as the need to take the highest change in CPD seen due to the coning effect. A next-generation SKN will hopefully reduce the accuracy issues, as well as providing a more consistent baseline for the measurements so that the CPD values of monolayered gold can be measured directly.

5.3.2. Electrochemical Impedance Spectroscopy

Electrochemical impedance spectroscopy was carried out as described in section 5.2.5 on a cleaned bare reference electrode, as well as a series of gold electrodes coated with a self-assembled monolayer of the organothiols listed in section 5.2.1. The results from these investigations were analysed in the software package Zview2, written by Scribner Associates.

5.3.2.1. Bare electrode

Impedance analysis requires the construction of a simulated equivalent circuit describing the general electrochemical process under observation and the fitting of this simulated data to the collected data via iterative methods. The equivalent circuit used to compute the resistance values for the bare electrode is shown below.

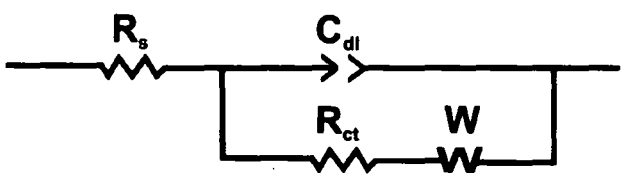

Figure 5.3.2.1.1 Equivalent circuit diagram for a bare gold working electrode.

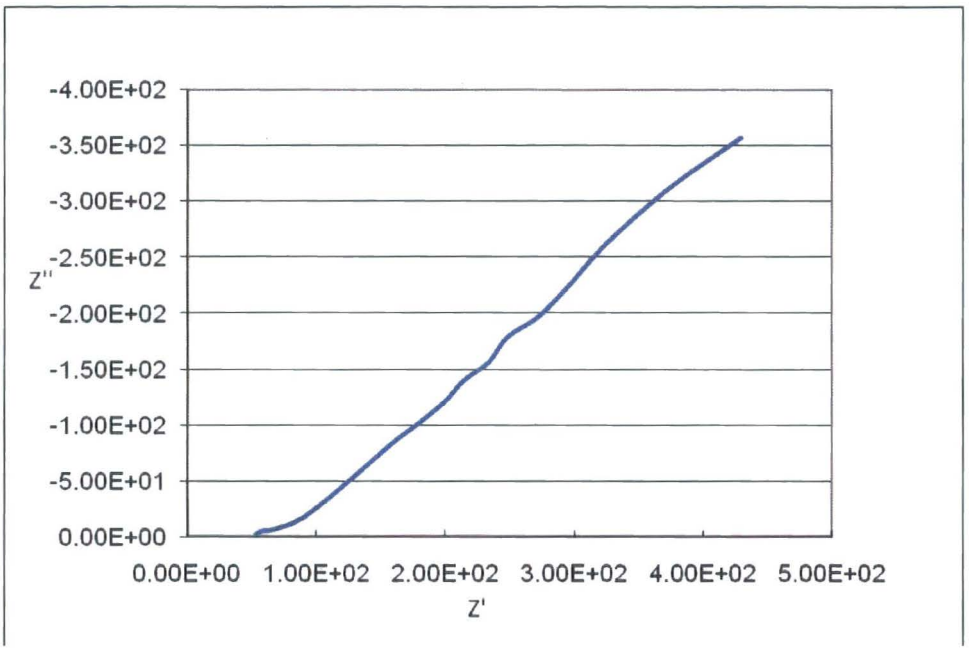

Figure 5.3.2.1.2. Nyquist plot of for 1mM $Fe(CN)_6^{3-/4-}$ in 0.1M KNO_3 solution using bare gold electrode. Frequency range: 0.1Hz to 100KHz.

Nyquist plots of impedance scans, such as the one above, are characterised by two distinct regions: a semicircular region in the bottom left (the higher frequency regions), relating to the charge-transfer processes occurring at the electrode surface and a straight, usually 45-degree, line relating to the Warburg semi-infinite diffusion processes. (See section 2.3.1). For the plot above showing the response of a bare electrode, the semicircular region is small, therefore showing a small charge-transfer resistance.

This data was fitted in Zview using the equivalent circuit shown above to obtain values for C_{dl} and R_{ct}, the capacitance and resistance terms for the Helmholtz double layer at the electrode surface. The solution resistance R_s was assumed to be 250Ω for fitting purposes – further runs with the fitted values gave an R_s value of 242.8Ω.

Table 5.3.2.1.3. Table of resistance and capacitance values for a bare gold working electrode surface, determined through electrochemical impedance spectroscopy.

	Value	Error
R_{ct} (Ω)	179.8	5.1
C_{dl} (F)	6.543×10^{-7}	4.215×10^{-9}

These values were then inserted into the equivalent circuit simulation for a SAM coated electrode.

5.3.2.2. SAM-coated electrodes

The circuit diagram is shown below:

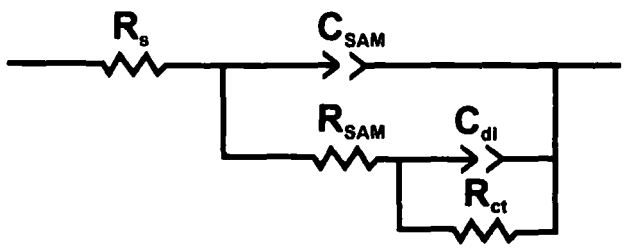

Figure 5.3.2.2.1. Equivalent circuit diagram for a gold electrode coated with a monolayer of thiol compound.

This circuit is constructed taking into account the resistance and capacitance of the bare electrode and Helmholtz double layer, the R_{ct} and C_{dl} respectively. In series with this are the resistance and the capacitance of the monolayer, R_{SAM} and C_{SAM}.

Results from electrochemical impedance spectroscopy scans of organothiol-monolayered electrodes were fitted to the equivalent circuit above. R_s, C_{dl} and R_{ct} values were used from the bare electrode runs. The results for R_{SAM} and C_{SAM} collected and tabulated.

Table 5.3.2.2.4. R_{SAM} values for SAM-coated electrodes.

	R_{SAM} (Ω)	Error
1-propanethiol	**1541**	12.5
1-hexanethiol	**10769**	101
1-dodecanethiol	**47509**	346
1-hexadecandethiol	**77935**	782
1-octadecanethiol	**85699**	526
16-merceptohexadecanonic acid	**78009**	623
2-ethyl-1-hexanethiol	**8074**	137
Thiobarbituricacid	**12546**	92.3
2-thiazoline-2-thiol	**16789**	351
Cysteine	**11006**	134
Glutathione	**22199**	245
Molecular wire	**8900**	180

Table 5.3.2.2.4. C_{SAM} values for SAM-coated electrodes.

	C_{SAM} (F)	Error
1-propanethiol	$\mathbf{5.21x10^{-7}}$	$3.11x10^{-9}$
1-hexanethiol	$\mathbf{4.68x10^{-7}}$	$4.13x10^{-9}$
1-dodecanethiol	$\mathbf{1.03x10^{-7}}$	$5.51x10^{-9}$
1-hexadecanethiol	$\mathbf{8.21x10^{-8}}$	$1.21x10^{-9}$
1-octadecanethiol	$\mathbf{3.26x10^{-8}}$	$1.25x10^{-9}$
16-merceptohexadeconic acid	$\mathbf{8.17x10^{-8}}$	$3.61x10^{-9}$
2-ethyl-1-hexanethiol	$\mathbf{4.89x10^{-7}}$	$6.41x10^{-9}$
Thiobarbituric acid	$\mathbf{4.46x10^{-7}}$	$5.24x10^{-9}$
2-thiazoline-2-thiol	$\mathbf{4.16x10^{-7}}$	$3.76x10^{-9}$
Cysteine	$\mathbf{4.89x10^{-7}}$	$1.32x10^{-9}$
Glutathione	$\mathbf{2.48x10^{-7}}$	$1.54x10^{-9}$
Molecular wire	$\mathbf{4.72x10^{-7}}$	$1.83x10^{-9}$

5.3.2.3. Alkanethiols

Nyquist plots were constructed of the results. As Nyquist plots cannot be compared directly, most have not been included here. The two plots included below show the difference in impedance characteristics for a short-chain alkanethiol (1-hexanethiol) and a long-chain alkanethiol (1-hexadecanethiol).

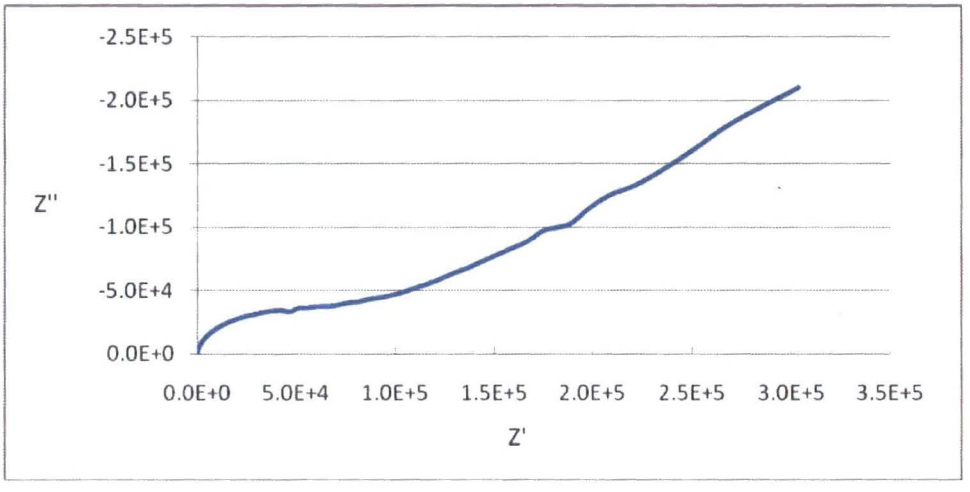

Figure 5.3.2.3.2. Nyquist plot of for 1mM $Fe(CN)_6^{3-/4-}$ in 0.1M KNO_3 solution using gold electrode coated with a monolayer of 1-hexanethiol. Frequency range: 0.1Hz to 100KHz.

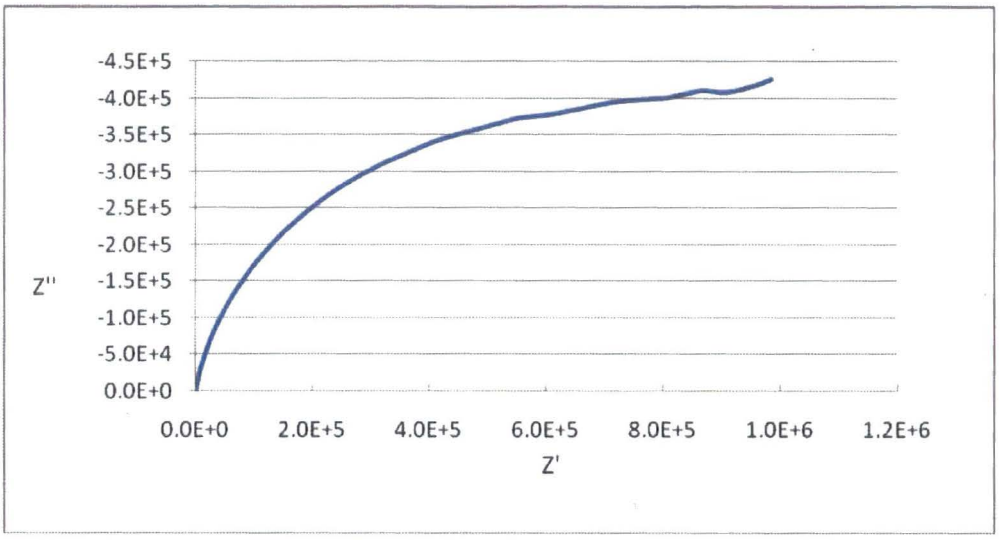

Figure 5.3.2.3.3. Nyquist plot of for 1mM $Fe(CN)_6^{3-/4-}$ in 0.1M KNO_3 solution using gold electrode coated with a monolayer of 1-hexadecanethiol. Frequency range: 0.1Hz to 100KHz.

The 1-hexanethiol plot shows a facile reaction, illustrated by the characteristic charge-transfer semicircle in the high-frequency region. Although far greater in magnitude then the bare electrode, the semicircular region still leads into the 45^0 Warburg impedance region at lower frequencies, illustrating the facile nature of the ferricynanide redox reaction taking place and consequently the poor blocking ability of the 1-hexanethiol monolayer.

The 1-hexadecanethiol plot shows a completely blocked reaction, as can be seen by the absence of the Warburg region. The charge-transfer resistance in this case is too high to allow the reaction to take place, showing that the monolayer completely blocks the electrode surface.

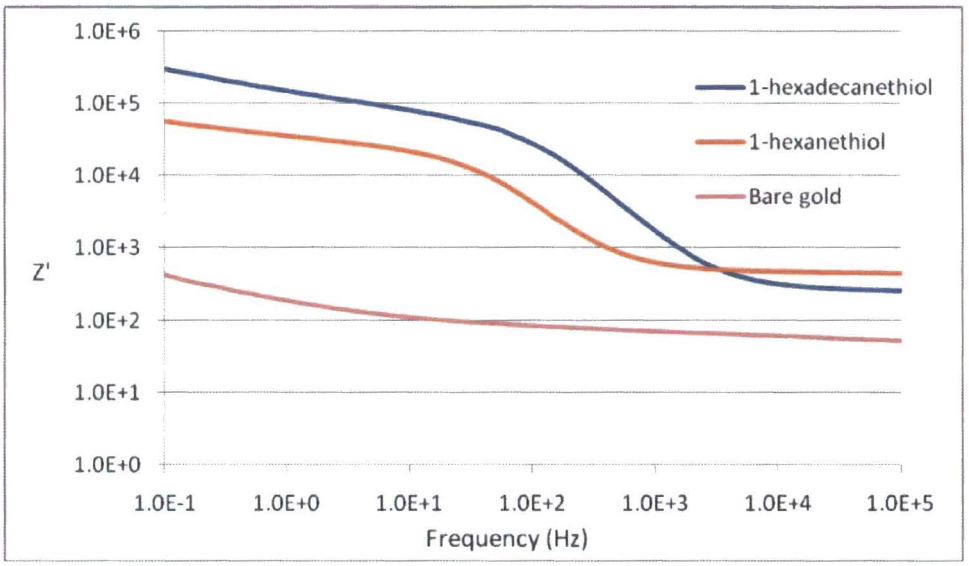

Figure 5.3.2.3.4. Bode plot showing results for a bare gold electrode, as well as electrodes with coatings of 1-hexanethiol and 1-hexadecanethiol.

The above graph is a bode plot, a graph of frequency against impedance, for – hexanethiol and 1-hexadecanethiol as well as for the clean gold electrode. Bode plots allow the direct comparison of the magnitude impedance results due to the use of logarithmic scales. As the scale is logarithmic, small differences in height equate to large differences in impedance. 1-hexadecanethiol has a Z' value of 8.65 times greater than 1-hexanethiol at 0.1Hz, for example.

Cyclic voltammetry measurements were carried out in order to investigate the degree of blocking ability of each monolayer. Measurements were carried out as described in section 5.2.5 using a clean gold working electrode, as well as electrodes coated with monolayers of 1-hexane and 1-hexadecanethiol.

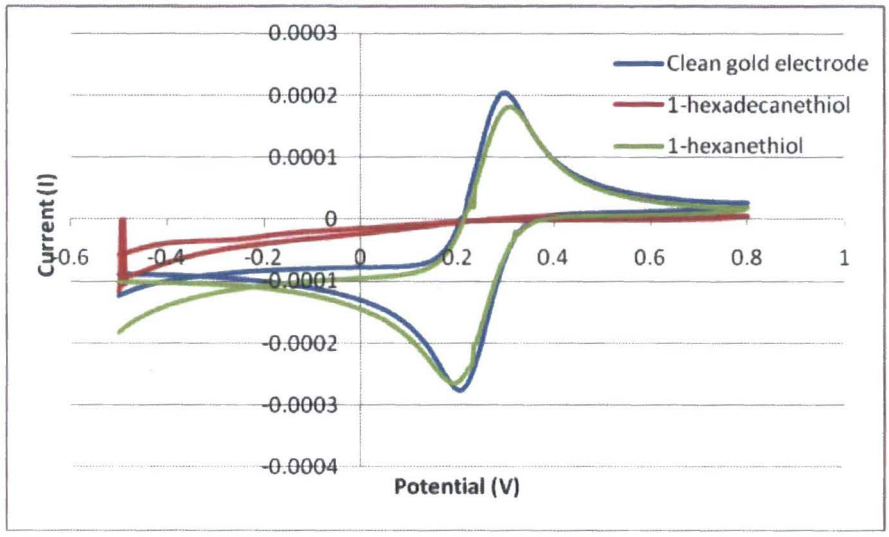

Figure 5.3.2.3.6. Cyclic voltammograms of clean and SAM-coated monolayers 1mM $Fe(CN)_6^{3-/4-}$ in 0.1M KNO_3 solution.

The CV results demonstrate the extreme blocking ability of the 1-hexadecanethiol monolayer. No reaction peaks can be seen. In contrast, 1-hexanethiol displays a response very similar to the clean electrode, showing that the redox reaction is not suppressed by the monolayer. The peak-to-peak separation of the reaction also does not change between the clean and 1hexanethiol scans, indicating that the kinetics of the reaction do not change. This suggests that the 1-hexanethiol monolayer has an extremely poor blocking ability.

The resistance and capacitance values for the linear alkanethiol molecules were plotted against the chain length of the molecule.

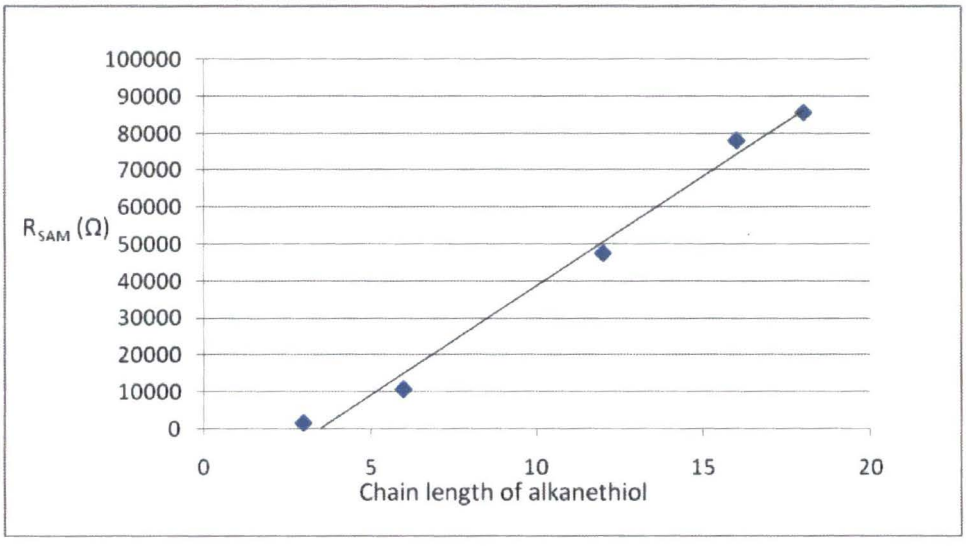

Figure 5.3.2.3.5. Graph showing the monolayer resistance (R_{SAM}) against the chain length of linear alkanethiols.

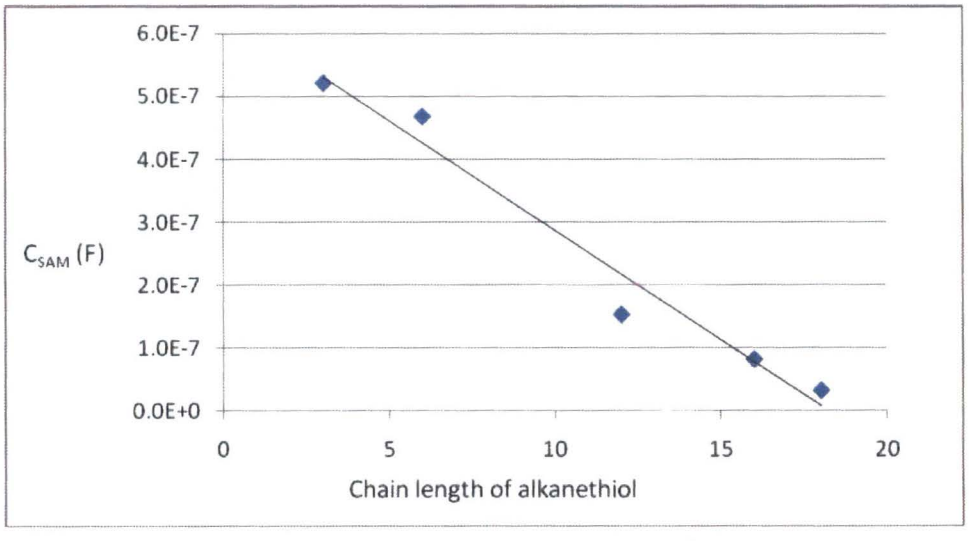

Figure 5.3.2.3.5. Graph showing the monolayer capacitance (C_{SAM}) against the chain length of linear alkanethiols.

Linear relationships can be seen for both resistance and capacitance, with resistance proportional and capacitance inversely proportional to the chain length

of the alkanethiol. The resistance increases due to the lessening conductivity of non-conjugated alkanethiols as they increase in length.

Longer alkane chains will have stronger Van der Waals forces between the chains, which will result in tighter-packed, more organised monolayers forming on the electrode surface. The capacitance therefore drops as thicker, more organised monolayers will have fewer defects and therefore will block access to the electrode surface. These results suggest that all the straight-chain alkanethiols are forming good-quality monolayers, and that therefore the resistance and capacitance values are a direct function of the length of the chain.

16-merceptohexadeconic acid has almost identical resistance and capacitance values to 1-hexadecanethiol, which is at odds with the distinctly lower ΔCPD value recorded during the SKN measurements. 2-ethyl-1-hexanethiol records a significantly lower resistance and greater capacitance to 1-hexanethiol. This suggests that the monolayer is of a significantly lower quality then hexanethiol due to the steric hindrance of the ethyl branch preventing intermolecular attractive forces.

5.3.2.4. Cyclic and biological thiols

2-ethylbenzenethiol and 2-phenylethanethiol proved impossible to measure due to extreme difficulties assembling a monolayer onto the electrode surface. The monolayer was either completely non-existent or the electrode became completely fouled due to crystallisation.

Monolayers of thiobarbituric acid and 2-thiazoline-2-thiol were able to be applied, and electrochemical impedance spectroscopy measurements were taken. These measurements are shown below together with the results of EIS measurements of cysteine and glutathione.

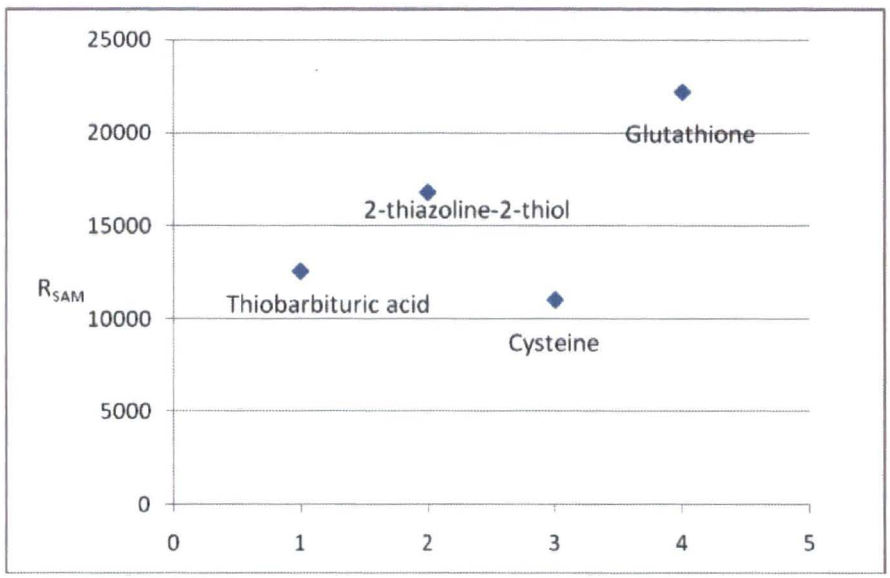

Figure 5.3.2.3.5. Graph showing the monolayer resistance (R_{SAM}) of measured aromatic and biological organothiols.

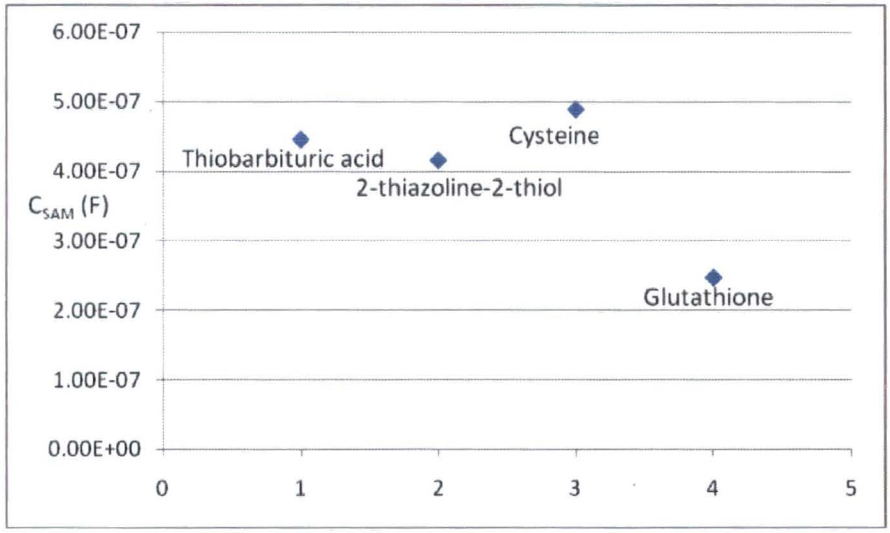

Figure 5.3.2.3.5. Graph showing the monolayer resistance (C_{SAM}) of measured aromatic and biological organothiols.

All of the aromatic and biological thiols recorded low resistance and high capacitance values relative to the straight-chain alkanethiols. This is once again due to the difficulties of forming high-quality monolayers – intermolecular forces are

hindered by the shapes and orientations of the molecules. Glutathione records a significantly greater resistance value then the other compounds owing to the sheer physical size of the molecule and therefore the thickness of the monolayer formed. This value is still very small compared to a straight-chain alkanethiol, however, roughly equivalent to the value expected for 1-heptanethiol.

5.2.3.5. Molecular wire

The molecular wire recorded very low R_{SAM} (8900Ω) and very high C_{SAM} ($4.72x10^{-7}F$) results relative to the other molecules. A Bode plot relative to 1-hexanethiol and 1-hexadecanethiol is shown below:

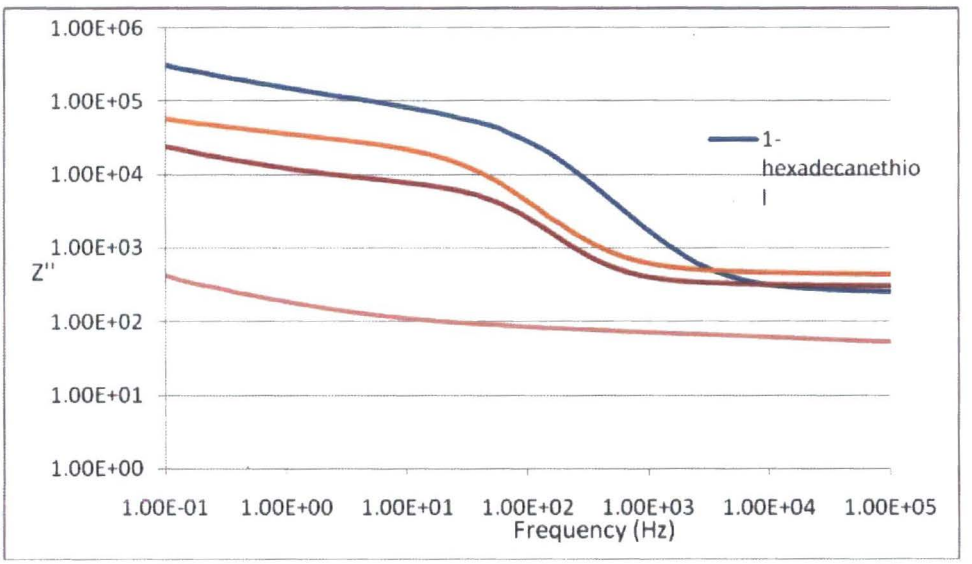

Figure 5.2.3.5.1. Bode plot comparing EIS results from the molecular wire with common alkanethiols.

The molecular wire has extremely low charge-transfer impedance values, lower then even 1-hexanethiol, a much smaller molecule. 1-hexadecanethiol has a charge-transfer impedance nearly 100 times greater than the molecular wire. Further work carried out in the research group by Francisco Aguiar using mixed monolayers of 1-dodecanethiol and the molecular wire confirmed that the mixed monolayer has a charge-transfer impedance value close to pure 1-dodecanethiol, a clear indication

that the low impedance values were being caused by pinholes caused by poor formation of the molecular wire monolayer.

5.3.2.6. Conclusions

The impedance results seem to parallel the SKN results closely. The resistance of straight-chain alkanethiols increases in a linear fashion, as would be expected. Capacitance can be seen to be inversely proportional to the length of the alkane chain. As the length of chain increases, the blocking ability of the monolayer increases, as can be seen by the cyclic voltammetry results.

Electron transfer between the electroactive solution species and the electrode surface can occur in one of three ways[14]. These are; electron tunnelling through the film, permeation of the electroactive species through the monolayer and electroactive species diffusing through bare areas (pinholes) in the layer. The blocking ability of the monolayer will depend on a combination of all three factors.

A short-chain alkanethiol such as 1-propanethiol or 1-hexanethiol will allow a far greater quantity of electron tunnelling then a longer dodecane or hexadecane thiol. It follows, therefore, that the response of the electrode will drop with increasing length of the alkanethiol and therefore blocking ability of the monolayer. Electroactive species will also find it greatly more difficult to permeate through a longer-chain alkanethiol monolayer due to the greater intermolecular attractive forces of the longer alkane chain producing a closer-packed, less permeable layer.

If the monolayer is prevented from assembling in a close-packed manner, pinholes and bare areas will appear, allowing the electroactive species to access the electrode surface. This will significantly decrease the resistance and blocking ability of the monolayer. The functionalised, branching and biological thiols had measured resistances significantly lower (usually over a hundred times) then the straight-chain alkanethiols. This can be seen in the results for the cyclic thiols thiobarbituric acid and 2-thialozine-2-thiol, both of which have extremely low resistance values for the

molecular size. Cysteine and glutathione also exhibit low resistance values, suggesting that the large branching structure of these molecules prevents formation of a good monolayer. It would appear from the results of the 2-ethyl-1-hexanethiol scan that the ethyl chain notably affects the ability of hexanethiol to form a good-quality monolayer, and thus affects the resistance and capacitance values of the monolayer accordingly.

The result from the EIS scans match up well with the SKN images, with the same linear relationship between alkanethiol chain length and measured value seen for both techniques. The SKN also predicted to a great extent the results for the biological and cyclic organothiols, with the high ΔCPD values seen for these molecules meeting up with the low resistance values seen with EIS.

Interestingly, the SKN gave very low ΔCPD values for 1-propane and 1-hexanethiol and high values for the branched and cyclic thiols. EIS gave low resistance and high capacitance results for both the shorter linear and the branched and cyclic molecules. This suggests that the SKN can distinguish between thin monolayers and poor-quality monolayers caused by loosely-packed molecules, wheras EIS measurements cannot. Therefore, the ΔCPD measurement appears to be a far more intrinsic monitor of monolayer quality and packing. EIS can only measure the ability of an electroactive probe to penetrate the monolayer. With further work on a wider variety of thiols, the ΔCPD measurement could provide very useful information on the quality and composition of an electrode monolayer, far more so then conventional electrochemical techniques.

References

[1] Honda M, Baba Y, Hirao N, Sekiguchi, *Journal of Physics: Conference Series,* 2008, **100,** 1-5

[2] Wasserman, S R, Tao, Y T, Whitesides, G M, *Langmuir,* 1989, **5,** 1074-1087.

[3] Ulman A, *Chem. Rev.* 1996, **96,** 1533-1554

[4] Frey S, Stadler V, Eck W, Zharnikov M, *Langmuir,* 2001, **17,** 2408-2415

[5] Strong L, Whitesides G M, *Langmuir,* 1988, **4,** 546-558

[6] Ulman A, Eilers J E, Tillman, N. *Langmuir,* 1989, **5,** 167-174

[7] Poirier, G E, Tarlov M J, *Langmuir,* 2001, **17,** 2408-2415

[8] Vericat, C, Vela M E, Benitiz, J A, *Phys. Condens. Matter,* 2006, **18,** 867-900

[9] Sandhyrani N, Pradeep T, *Pure. Appl. Chem, 2002,* **74,** 1593-1607

[10] Wang C, Batsanov A S, Bryce M R, *Faraday Discuss.*, 2006, 131, 221 – 234

[11] M. Thompson, L. Cheran *et al, Biosensors & Bioelectronics,* 2005, **20,** 1471.

[12] Cheran, L E, Leiss, H D, Thompson, M, *Analyst,* 1999, **124,** 961-970

[13] Li G, Butt, H-J, Graf K, *Langmuir*, 2006, **22**, 11395 -11399

[14] Finklea , H. O., Snider D. A., Fedyk J, *Langmuir,* 1990, **6,** 371-376

Chapter 6: Conclusions and Further Study

This thesis has covered a broad range of investigations and experimental methods. The promising analytical technique of Scanning Kelvin Nanoprobe microscopy has been used extensively to investigate films and monolayers of organothiols and phthalocyanine derivatives, and has proven itself to be a capable new tool in the analytical chemistry arsenal. It has been shown to be able to detect very small variations in molecular structure – for instance the addition of a methelyne group in an alkanethiol chain – as well as the ability to image monolayer organisation and composition. The SKN however suffers from the characteristic teething issues associated with new and prototype instruments. The inability of the instrument to provide a consistent baseline for measurements, caused in part by slight changes in environmental conditions as well as by human error in tip positioning and background noise reductions, cause problems when devising investigations. Samples must be prepared in a way so that the change in CPD between regions, a value that remains constant, can be measured. A further iteration of the SKN, ruggedized and commercialised for general analytical work, would hopefully solve this issue.

The work on the effects of the hydrogen bonding environment of differing DMSO:water mixtures on brought up some interesting questions on the effects these environments have on the reactivity and mechanism of biochemical reactions. These reactions are often very finely tuned in the living cell to pH and redox conditions, and slight deviations can often make reactions proceed in an unexpected manner. This is especially true for native protein folding, where the strength and pKa of the S-H bonds required to form the tertiary structure are greatly affected by the hydrogen bonding environment. The results described in Chapter 3 suggest that small-molecule protein folding catalysts such as BMC will behave in a significantly different manner in the aqueous environment *in vivo* then in the standard DMSO:water mixtures used *in vitro*. Further work in this area would

investigate whether these effects have a significant consequence on the outcome of biochemical reactions, and would test the effect of the DMSO:water hydrogen bonding environment on a wider range of biological materials, including peptides and proteins.

The work described in Chapter 4 on phthalocyanine derivatives shows some very interesting results. It appears that crystalline formation can be discouraged, allowing amorphous films to form, by the addition of large aromatic axial groups to a metallocentred phthalocyanine compound. This is obviously seen in the AFM images of the compound. This enhances the substrate-derivative interaction via aromatic π-π interactions, allowing a degree of order in the film. This appears to create a nanoporous material due to interstices forming between the phthalocyanine molecules. In electrochemical tests using probe molecules, this film appears to be both size and charge selective, though a greater variety of probe molecules is needed to say for sure. There is a good deal of promising further work that could be undertaken in this area. The phthalocyanine derivatives could act as excellent molecular sieves, allowing simple and responsive ion-selective electrodes to be constructed. Further work would investigate and tune the properties of the phthalocyanine derivative, including further synthetic work and investigations on the best way to deposit and layer the films.

The bulk of the work utilising the SKN is found in the investigations of thiol monolayers in Chapter 5. This was a large body of work, attempting the ambitious task of a systematic investigation of the effect on the work function of a monolayer with differing molecular composition. A series of organothiols were chosen for this work, but due to time and cost constraints there were several gaps in the roster, with several important areas, such as di-, aromatic and functionalised thiols, missing or incomplete. This makes it difficult to draw final conclusions of the effects of these organothiol families on the work function of their self-assembled monolayer. However, good results were obtained for the straight-chain alkanethiols and several interesting conclusions were inferred for the other organothiol families. The SKN shows considerable promise in the detection and characterisation of organothiol

monolayers, as the images and results in the chapter illustrate. A full investigation into this area, with extensive exploration of all the major families of organothiols, would fill in the obvious gaps in this initial investigation. This work if fully explored would probably prove enough material for a PhD thesis in its own right, and would be invaluable in the future development of the SKN as an analytical tool.

Conferences attended and papers published

Conferences Attended

BioNEt, Durham University, March 2005. *Poster Displayed*

Electrochem 2005, September 2005, Northumbria University, Newcastle Upon Tyne. *Poster Displayed*

BioNEt, Newcastle University Medical School, November 2005. *Poster Displayed*

REC Electroanalytical Group Postgraduate Symposium, Birckbeck College, London, November 2005. *Oral Presentation*

RSC Electroanalytical Group symposium, Bath University, March 2006.

ISE 2006, Heriot-Watt University, Edinburgh. Sepetember 2006. *Oral Presentation*

REC Electroanalytical Group Postgraduate Symposium, Birckbeck College, London, November 2006. *Oral Presentation*

Electrochem 2007, September 2007, Imperial College, London. *Oral Presentation*

Papers Submitted

1. 'The effect of a hydrogen bonding environment (dimethylsulfoxide) on the ionisation and redox properties of the thiol group in cysteine and a Protein Disulfide Isomerase Mimic (Vectrase)'.

Jaanus Kruusma, Aidan Rhodes, Radhika Bhatia, J.A.Gareth Williams, Adam.M. Benham, Ritu Kataky. *Journal of Solutions Chemistry,* 2007, **34,** 517-529.

2. 'Electrochemical sieving effects of a pthalocyanine derivative designed to form a nanostuctured film'.

Carl Barker, Alan Massey, Aidan Rhodes, Rupam jyoti Sarma, Ankit Samadariya' Martin.R..Bryce, Ritu Kataky. *Langmuir* (submitted).